



THE UNIVERSITY OF
WESTERN AUSTRALIA

Design and Implementation of a Battery Management System REV (JET-SKI)

Don Madappuli 20373911

Supervisor: Professor Thomas Braünl
Renewable Energy Vehicle Project

Final Year Project Thesis

School of Electrical, Electronic and Computer Engineering
The University of Western Australia

Submitted: 1st November 2013

NOMENCLATURE

DOD	depth-of-discharge
SOC	state-of-charge
C	charge capacity
Ah	Ampere Hours
A	Amp
V	Voltage
I	load current
E°	theoretical open circuit voltage
E	cell voltage
ΔE_{sd}	voltage drop due to self-discharge
ΔE_{rd}	voltage drop due to reactant depletion
ΔE_{mt}	voltage drop due to mass transfer resistance
ΔE_{init}	initial voltage drop during discharge
a_k	specific surface area of electrode k (k = p, n) (m^2m^{-3})
$c_{e,k}$	electrolyte concentration in region k ($mol\ m^{-3}$)
$c_{e,k,o}$	initial electrolyte concentration in region k ($mol\ m^{-3}$)
$c_{s,k}$	concentration of Li^+ ions in the intercalation particle of electrode k ($mol\ m^{-3}$)
$c_{s,k,o}$	initial concentration of Li^+ ions in the intercalation particle of electrode k ($mol\ m^{-3}$)
D	electrolyte diffusion coefficient (m^2s)
$D_{s,k}$	Li^+ ion diffusion coefficient in the intercalation particle of electrode k ($m^2\ s$)
L	total thickness of cathode-separator-anode (m)
R	universal gas constant
T	Absolute Temperature (K)
j	Current density
x	Spatial coordinate
F	Faraday's constant ($C\ mol^{-1}$)
EOL	End Of life
DC	Direct current

AC	Alternating Current
REV	Renewable Energy Vehicle
LiFePo4	Lithium Iron Phosphate
EV	Electric Vehicle
HEV	Hybrid Electric Vehicle
NiCd	Nickel Cadmium
SAE	Society of Automotive Engineers
VCL	Variable Control Logic
LED	Light Emitting Diode



1. PREAMBLE

With population growth and urbanization steadily increasing in the 21st century there has been growing concern for environmental degradation resulting from carbon emission. According to Dr Mike Raupach, chairman of CSIRO Atmospheric, studies show that the rate of carbon dioxide emission has increased 2.5% annually between 2000 to 2005 [22]. As a result, pressure from global interests groups has led all industries to adopt an ecofriendly approach to both their manufacturing processes as well as the end product provided to the consumer.

Society's traditionally heavy reliance on fossil fuels as an energy source for daily transportation has had to be reconsidered to minimize the world carbon footprint. Modern engineering and technological advancements have seen an entry of renewable energy vehicles utilizing electricity in place of the internal combustion engine. Whilst such technologies are currently in early research and developmental stages, implementation of electric motors into the automotive sector will ensure environmental sustainability. It is vital that in-depth research is undertaken by academic institutions and external industries to refine, improve this form of transport to ensure that it will be a viable option for the future.

ACKNOWLEDGEMENTS

This project titled “Design and Implementation of a Battery Management System REV (Jet-Ski)” is dedicated to the many people that have shared their knowledge and expertise in the comprehensive way so that this thesis could be made possible. The author would like to thank Professor Thomas Braünl for his guidance throughout the year and for coordinating the team to achieve project deadlines and goals. The support of all the colleagues at the REV Jet Ski have aided greatly in not only creating a vibrant team environment but has made the project an extremely formative one. A special thank you to Ms Natalie Drew for all her co-editing efforts and most importantly my family and friends for their continual patience throughout the year. I have been very blessed to have such loving family and if it were not for their continual help throughout my undergraduate years I would not have been able to come this far.

Table of Contents

1.1.1	PROJECT IMPLEMENTATION MAP.....	9
1.1.1.	PROJECT TIMELINE	10
1.1.2	ELECTRICAL CABLING SAFETY	10
1.1.3	ELECTRICAL/ELECTRONIC COMPONENTS	11
1.1.4	CIRCUIT PROTECTION	11
1.2	DRIVE SYSTEM	11
3.5.2	SYSTEM CONTROL	12
1.3	BATTERY ANALYSIS.....	12
1.3.1	SYSTEM DESIGN.....	12
1.4	DESIGN SAFETY	13
1.5	INGRESS PROTECTION	13
2.	CURRENT BATTERY TECHNOLOGIES	14
2.1	TECHNICAL REQUIREMENTS.....	16
4.1.2	COMPARISON OF ELECTROCHEMICAL CELLS.....	18
4.1.3	INTERNAL RESISTANCE	19
4.1.4	PEUKERTS LAW.....	21
4.1.5	SIMULATION OF PEUKERTS LAW	23
4.1.6	SIMULATION RESULTS OF PEUKERTS LAW	25
4.2	CYCLE LIFE.....	26
4.3	THERMAL RUNAWAY	28
4.4	OVERCHARGING TOLERANCE.....	29
4.6	SAFETY	30
5	IDEAL ELECTROCHEMICAL CELL	31
5.1	CELL MODEL COMPARISONS	33
5.1.2	CONSIDERATIONS.....	33
5.2	TORQUE POWER CAPABILITIES.....	34
5.2.1	CALCULATION OF MAXIMUM TORQUE	35
5.3	POWER DELIVERY	37
5.4	SUITABILITY CRITERIA.....	38
9.	PROPOSED CIRCUIT CONSTRUCTION.....	56
10.	BATTERY MODULE WIRING.....	59
11.	ELECTROCHEMICAL CELL MODELLING	59
11.1	MATHEMATICAL DERIVATION	60
11.2	USING ANSYS FLUENT TO MODEL ELECTROCHEMICAL BEHAVIOR (SINGLE CELL).....	63

11.3 USING ANSYS FLUENT TO MODEL ELECTROCHEMICAL BEHAVIOR (ENTIRE MODULE LAYER)	66
12. CHARGE CONCENTRATION MODELLING	68
12.1.1 SIMULATION RESULTS	71
13. BATTERY MANAGEMENT SYSTEM DESIGN	73
14. MODULE CIRCUIT DESIGN	75
14.1 BMS HOUSING	77
15. CONCLUSION	78
18. CD CONTENT (PAGE 92)	

1. INTRODUCTION

With the guidance of Professor Dr. Thomas Braunl, the University of Western Australia is currently developing innovative engineering solutions to implement plug-in electric technologies to everyday vehicles. The Renewable Energy Vehicle Project by UWA has seen the development of numerous road vehicles such as the REV Racer (2009 Lotus Elise) and REV Eco (Hyundai Getz) which aim to create electric plug-in vehicles as a viable option in place of the traditional petrol engine. In 2013 the focus will be on utilizing technologies embedded within the aforementioned vehicles into traditional petrol powered water sports vehicles. Studies conducted have shown that in Michigan alone 82,000 registered water crafts are able to disperse more than 757,000 litres of petrol annually [23]. Furthermore it is estimated that exhaust gases emitted from using a traditional Jet Ski for 2 hours is equivalent to the same amount of carbon emission produced by a 1998 vehicle driving 20,800 kilometres [24]. With attention to the alarming amount carbon and noise pollution by road vehicles such negative statistics regarding personal watercrafts have turned the spotlight into making water sports more environmentally sustainable. The following project will aim to convert a conventional Jet Ski (2008 Seadoo 4-Tec) powered by a petrol engine into an electric Jet Ski in order to achieve both zero emissions and performance efficiency comparable to a conventional petrol engine Jet Ski.

Design and implementation of an efficient battery power source shall be the main focus of this research project, with the objective of attaining comparative performance figures to traditional petrol engine Jet Skis. Furthermore, research into a suitable battery management system and charging method will be undertaken to maximize performance during its usage in water activities. Numerous forms of battery sources are available currently on the market for similar road vehicle electric conversion projects. However, due to the fact that such a vehicle will be used on water, consideration must be made to the suitability of these different power sources. It is paramount that implementing a particular battery and charging system will allow the vehicle to ultimately meet all safety and design standards governed by the relevant authorities. The end goal of conducting such a research project will be to not only produce a working electric Jet Ski, but to also prove its viability to both the consumer and its possibility to be marketed as a product.

1.1 SCOPE OF WORK

The scope of work encapsulated the analysis, design, manufacture, testing and evaluation of the UWA Rev Jet Ski project electrical component. This document stipulates all design and safety standards that shall be administered throughout the entirety of the project cycle. Important considerations regarding financing, project milestone deadlines and final deliverables are discussed within the scope of work. It is important to note that throughout the project, guidelines set out in the scope of work have been modified due to extenuating circumstances. However all safety and design requirements discussed in this section have not been deviated from.

1.1.1 PROJECT IMPLEMENTATION MAP

The UWA Renewable Energy Vehicle Project has been engaged in the design and manufacture of an electric personal watercraft (Jet Ski). Primary objectives of the project are as follows:

- Address prevalent socio-economic problems as discussed in section 1.
- Attain comparable performance figures to that of its ICE (internal combustion engine counterpart)
- To complete the effective marketization of an electric model on a commercial scale

Achievement of the following objectives are to be realised through a systems approach, wherein third party equipment such as vehicles chassis, safety/electrical components, power source and mechanical structures are procured through the respective vendors. All work carried out during the project life cycle is divided into a respective projection phase so that progress can be easily monitored. Displayed below in table 1 is the project phase map that also shows the tasks required for completion at each phase.

Figure 1: Project Implementation Map



1.1.1. PROJECT TIMELINE

For the project timeline and deliverables please refer to Appendix A. Front end loading one and two (FEL1/FEL2) shall be the main focus for this thesis and objectives in 2013. Whilst measures were taken to achieve all phases within an appropriate timeframe, unforeseen circumstances such as equipment lead time, workshop fabrication delays and design deviations have meant that only phases FEL1, FEL2 and a small part of construction phase have been achieved thus far. A separate, secondary factory acceptance test scope shall be produced to address the project close-out phase.

1.1.2 ELECTRICAL CABLING SAFETY

Electrical cabling is to be conducted in accordance to the UWA Electrical safety guidelines which are adopted by the Energy Safety Act 2006.

- ✚ All electrical wiring, installation and maintenance shall be carried out with respect to AS/NZ 3000. Work is to be conducted only on ELV (extra low voltage systems) not exceeding 50V a.c or 120V DC ripple feed.
- ✚ Exposure to voltages above the ELV limit can only be undertaken under an electrical license or permit as per the Electricity Licensing Regulation 1991.
- ✚ All high voltage cables shall have a minimum insulation thickness of 2mm as highlighted by the SAE J2929_20132 “Hybrid Vehicle Propulsion Battery Safety Standard”.
- ✚ Mandatory circuit protection should be integrated to all loops as a required by SAE J1797 “Recommended Practice for Electric and Hybrid Electric Vehicle Battery Systems Crash Integrity Testing”
- ✚ All electrical connections shall be terminated either through the use of copper plated lugs or to be directly soldered.
- ✚ Where wires are connected to components through the use of solder, heat shrinking must be carried out.
- ✚ All wiring must be checked for insulation damage prior to engaging in the testing and close-out phase. Where faults are found, the immediate power source is to be isolated for repair.
- ✚ Selection of appropriate conductor cables shall be made on the basis of the safe operating temperature for the respective load.

1.1.3 ELECTRICAL/ELECTRONIC COMPONENTS

The REV Jet Ski team is responsible for the design and production of the following components:

- ✚ Battery module power system, which shall not exceed the ELV limit as mentioned in section 1.3 (Electric Cabling standards).
- ✚ Connections between anode/cathode terminals are to be completed through the use of suitable bus bars. Bus bar temperatures are to not exceed the maximum operating temperature of 70°C unless adequate cooling systems are in place.
- ✚ A Battery Management system is to be produced within the power source circuit to ensure circuit protection and to maximise the operational life of the cells. All specifications of the battery management system are to suit the specifications of cells and respective module design.
- ✚ Charging system for the battery power source shall be done through an appropriate third party charger. The charger shall utilise a general power outlet during the charging sequence of the battery modules.

1.1.4 CIRCUIT PROTECTION

- ✚ Circuit protection system shall incorporate the Battery management system, through the use of inline relays.
- ✚ Circuit protection system needs to have the following sensing parameters: water/moisture, temperature and ignition.
- ✚ All sensors are to be connected to physical 12V relays that are able to de-energize the loop upon error/fault conditions.
- ✚ Safety system shall incorporate programmable logic (PLC) for error reporting as well as condition monitoring.

1.2 DRIVE SYSTEM

- ✚ Submersible Motors Pty Ltd is responsible for the fabrication of the motor drive system for the watercraft.
- ✚ Specifications of the motor are to be communicated to the vendor Submersible Motor Engineering SME based on nominal voltage of the battery power source and motor controller specifications (Appendix B).
- ✚ The watercrafts impeller and drive shaft shall be manufactured by SME to suit the spline requirements of the motor.

3.5.2 SYSTEM CONTROL

- ✚ An encoder is to be made as an attachment to the motor end shield so that rotor torque values can be monitored.
- ✚ The motor controller is to be integrated into the drive system to monitor important safety and performance data. Programming using the CanBus interface is to be carried out to meet the requirements of the project.

1.3 BATTERY ANALYSIS

Several studies and simulations are to be conducted prior to deciding on a suitable battery technology for the power source. The cells are to meet suitability criteria as highlighted below:

- ✚ Outer encasing of batteries must not exceed the respective maximum operating temperature under proposed loads.
- ✚ Cells are to be purchased within the project allocated budget of AUD\$5000
- ✚ Total run time is to be somewhat comparable to the pre conversion specifications of 30 minutes

The scope of work for power source analysis shall include the use of relevant software to propose the most suitable cell under project requirements. Thermal mapping methods are to play an integral role in the selection of a suitable battery technology/model.

1.3.1 SYSTEM DESIGN

Construction phase of the proposed battery system needs to ensure that suitable safety measures are in place to minimise the risk of fire hazard and personal injury. Battery system is to have these features installed;

- ✚ Circuit protection using a suitable battery management system (BMS); to comply with SAE J2929_20132
- ✚ In line relay/contactors directly near the battery modules for loop cut-off in the event of a short circuit or sparking
- ✚ Individual module monitoring by the BMS system at each node in the circuit
- ✚ Inclusion of safety sensors to detect moisture, ambient temperature, short circuit and loop monitoring
- ✚ BMS system must have error latching capabilities so that manual reset is required once error conditions are fixed

1.4 DESIGN SAFETY

Where modules are able to make direct contact with electrically conducting materials the use of polycarbonate sheeting is recommended. Adequate ventilation is to exist in areas where excessive thermal generation can occur (i.e. battery modules).

- ✚ There can only be a minimum 5mm clearance between modules and enclosure walls on either side
- ✚ A suitable cooling apparatus is to be constructed by the mechanical students for effective heat dissipation from batteries

1.5 INGRESS PROTECTION

An ingress protection rating of IP65 and above is to be maintained in all areas where electronic components are either housed or in operation. Moreover the IP65 rating will allow for minimal dust contamination within all enclosures and cavities. Saline moisture is to be avoided at all times within the hull area due to the numerous electronic components being housed in this locality.

2. CURRENT BATTERY TECHNOLOGIES

Battery cells represent the most important element of an electric vehicle (EV) as its electrochemical structure allows energy to be harnessed and turned into mechanical work on a motor. This harnessed energy can vary according to the way in which particular types of batteries are developed. Therefore, advancements in increasing battery efficiency are key to the success of all electric vehicles. The oldest form of rechargeable batteries are lead acid and, since its inception in 1859, there have been developments and changes to the types of batteries used in EVs, hybrid electric vehicles (HEVs) and pure battery electric vehicles (BEVs) [1]. In the world of renewable energy vehicles, lead acid batteries, whilst being inexpensive, provide the lowest range (approximately 50 kilometres) out of all other chemical cell types [2]. In today's renewable energy industry five different types of electrochemical cells exist, which include:

- ✚ Lead-acid batteries
- ✚ Nickel metal hydride batteries
- ✚ Lithium-Ion batteries
- ✚ Zinc-air batteries
- ✚ Molten salt batteries

Within each of these battery types exist numerous combinations of anode and cathode materials. The combination of anode and cathode material used in a battery entails its own advantages and disadvantages pertaining to cost, performance, efficiency, safety and lifespan of the battery. In order to compare these different types of battery cells, careful considerations must be made with respect to their chemistries and its impact on the aforementioned dimensions.

In selecting a viable electrochemical cell type, performance measures must be taken into account. These measures can be defined as followed:

- ✚ *Ampere hour capacity* – The following parameter (Ah) can be defined as the total charge which can be discharged when the battery is at a full charged status [3]. This rating is given as the rated amp hour capacity for specific conditions (temperature and discharge rate) from the manufacturer. We can also define the rated amp hour capacity using the following equation:

$$\text{✚ } \textit{Rated Ah Capacity} = \textit{Rated Wh capacity} / \textit{Rated Battery Voltage} \quad (1.1)$$

✚ *Nominal C rate* – This parameter is also known as the discharge current and is a value that represents the batteries rate of discharge relative to its maximum capacity when fully charged. The rate of discharge directly correlates to the amount of current that a particular battery is able to sustain for one hour whilst within a specified voltage range [3]. As an example, a battery that is rated at 1.6Ah will have nominal discharge rate (C) of 1.6A. Therefore we expect a 0.1C to be equal to 0.16A discharge rate.

✚ *Specific Energy* – This parameter defines the nominal energy within the battery per unit mass. This can also be described as gravimetric energy density [3]. The unit of measurement for this parameter is expressed as Watt hours per kilogram. Mathematically we can further define it as:

$$\text{Specific Energy} = \text{Rated Wh Capacity} / \text{Battery Mass (kg)} \quad (1.2)$$

✚ *Energy Density* – We can refer to energy density as the nominal battery energy available per unit volume. This unit of measurement is represented as Wh/m³.

✚ *Power Density* – Power density refers to the maximum amount of available power with respect to a unit volume. This value is specific to each electro chemical cell and its chemical composition. This value can be utilised in order to calculate the required battery size for a specific performance criteria. The expression for power density is W/m³.

✚ *Peak Power* – As per the United States Advanced Battery Consortium (USABC), we can define peak power as the maximum discharge of power that a battery is able to output to a load for a period of 30 seconds [4]. During this 30 seconds period, the voltage shall not fall below two thirds of its open circuit value (OCV). Mathematically this can be shown as:

$$P = \frac{2V_{OC}^2}{9R} \quad (1.3)$$

Where V_{oc} is defined as the open circuit voltage and R is the internal resistance of the battery.

- ✚ *State of Charge* – State of Charge can also be represented as (SOC %) which signifies the current capacity of a battery in relation to a percentage of the maximum capacity of a battery [4]. This value can usually be found through integration of the current to calculate the change in battery capacity over time. This can be presented as:

$$Q_t = Q_0 - \int_0^t i_a(t) dt \quad (1.4)$$

Where Q_0 represents the original capacity of the battery, with $\int_0^t i_a(t) dt$ being the change of battery capacity over the time interval 0 to t.

Depth of Discharge – The depth of discharge can be defined as the percentage of battery which has been discharged as a percentage of maximum capacity of the battery. A rate of 80% DOD discharge signifies what is known as a “deep discharge” [4].

2.1 TECHNICAL REQUIREMENTS

Selection of an appropriate electrochemical cell was based on the required operational and technical conditions of the project. Batteries are to be placed within the front-end cavity of the personal watercraft (Jet Ski). Batteries will be housed using a three-tiered aluminium battery box as shown below:

For the purpose of comparing the various electrochemical cells available for use, it is important to consider the operational conditions and requirements of our personal watercraft (Jet Ski):

- ✚ *Operating Temperature (Ambient conditions for battery modules)* – Battery cell modules are to operate efficiently at ambient temperature of 35 degrees Celsius under normal watercraft operation.
- ✚ *Nominal voltage requirements* – University policy for occupational health and safety stipulates the restriction of work on equipment/machines deemed to be high voltage (115V (DC) nominal and 50V AC) [5]. Work on high voltage equipment requires an electrician certificate or license. Therefore our Jet Ski shall utilise battery modules equivalent to 96V nominal dc to meet UWA restrictions. This is also advantageous as power loss through cabling can be represented by : $P_{loss} = i^2 \times R$
Where i the current and R equals the ohmic resistance in the cabling. Since current is inversely proportional to the voltage being used, we are able to minimise power losses by transmitting at higher voltages.

- + Safety (ingress protection/volatility) – The electrochemical cells must be able to withstand lateral g-forces caused by movement of the watercraft through the water. These forces should have minimal impact on the performance characteristics of the battery module being used. Furthermore it should provide safe handling throughout its lifetime of operation.

- + Moisture Ingressions – For the purpose of design implementation, the IEEE IEC60529 standard shall be adopted to ensure battery modules and the enclosure are able to conform to a specific degree of water and dust ingress. In this particular case, due to the vehicles marine application, stringent waterproofing standards are to be adhered to in order to minimise electrical faults caused by saline water admission. The table below provides a table of the IEEE IEC60529 [6] ingress protection codes that shall be considered during construction and implementation phase 1.

Table 1: IEC60529 INGRESS PROTECTION RATING CODES (IEEE PSES 2012)

IP CODE – 1 ST NUMERAL (DUST PROTECTION)	
NUMERAL	DUST PARTICLE SIZE
1	=50mm Diameter
2	=12.5mm Diameter
3	=2.5mm Diameter
4	=1.0mm Diameter
5	= Dust Protected
6	=Complete Dust-Tight
IP CODE – 2 ND NUMERAL PROTECTION FROM INGRESS OF WATER	
NUMERAL	DEGREE OF WATER PROTECTION
1	Dripping Water: Vertical
2	Dripping Water: 15° Tilt
3	Spraying Water
4	Splashing Water
5	Jetting Water
6	Powerful Jetting Water
7	Temporary Immersion
8	Continuous Immersion

Reference to figure one allows us to determine the most suitable ingress protection rating for both battery modules and battery enclosure during design and implementation phase 1. Due to the watercraft's marine application, all batteries should be able to withstand a certain degree of saline moisture as the direct result of normal operational use. Whilst all batteries incorporate waterproof insulation jackets to protect the internal circuitry, anode and cathode plates of batteries on most cells are not protected from oxidation due to water and saline contact [7]. For this reason a minimum ingress protection rating of IP65 will be used as the benchmark for considering appropriate electrochemical cells and cell enclosure for the design phase.

4.1.2 COMPARISON OF ELECTROCHEMICAL CELLS

In order to determine the most appropriate cell to utilise in the production of an electric watercraft our primary parameters to evaluate each cell shall be based on the aforementioned factors but also the electrochemical performance parameters: Energy Density, Internal Resistance, Specific Energy, Power Density, Depth of Discharge and Toxicity.

Figure 2 below illustrates these performance characteristics and considerations for each electrochemical cell.

Figure 2: BATTERY TECHNOLOGY PERFORMANCE COMPARISON (BATTERY UNIVERSITY 2011)

Battery Technology Comparison

Specifications	Lead-Acid	NiCd	NiMH	Li-Ion		
				Cobalt	Manganese	Phosphate
Specific energy density (Wh/kg)	30 – 50	45 – 80	60 – 120	150 – 190	100 – 135	90 – 120
Internal resistance (mΩ/V)	<8.3	17 – 33	33 – 50	21 – 42	6.6 – 20	7.6 – 15.0
Cycle life (80% discharge)	200 – 300	1,000	300 – 500	500 – 1,000	500 – 1,000	1,000 – 2,000
Fast-charge time (hrs.)	8 – 16	1 typical	2 – 4	2 – 4	1 or less	1 or less
Overcharge tolerance	High	Moderate	Low	Low	Low	Low
Self-discharge/month (room temp.)	5 – 15%	20%	30%	<5%	<5%	<5%
Cell voltage	2.0	1.2	1.2	3.6	3.8	3.3
Charge cutoff voltage (V/cell)	2.40 (2.25 float)	Full charge indicated by voltage signature	Full charge indicated by voltage signature	4.2	4.2	3.6
Discharge cutoff volts (V/cell, 1C*)	1.75	1	1	2.5 – 3.0	2.5 – 3.0	2.8
Peak load current**	5C	20C	5C	> 3C	> 30C	> 30C
Peak load current* (best result)	0.2C	1C	0.5C	<1C	< 10C	< 10C
Charge temperature	-20 – 50°C	0 – 45°C	0 – 45°C	0 – 45°C	0 – 45°C	0 – 45°C
Discharge temperature	-20 – 50°C	-20 – 65°C	-20 – 65°C	-20 – 60°C	-20 – 60°C	-20 – 60°C
Maintenance requirement	3 – 6 months (equalization)	30 – 60 days (discharge)	60 – 90 days (discharge)	None	None	None
Safety requirements	Thermally stable	Thermally stable, fuses common		Protection circuit mandatory		
Time durability				>10 years	>10 years	>10 years
In use since	1881	1950	1990	1991	1996	1999
Toxicity	High	High	Low	Low	Low	Low

Source: batteryuniversity.com. The table values are generic, specific batteries may differ.

**C* refers to battery capacity, and this unit is used when specifying charge or discharge rates. For example: 0.5C for a 100 Ah battery = 50 A.

**Peak load current = maximum possible momentary discharge current, which could permanently damage a battery.

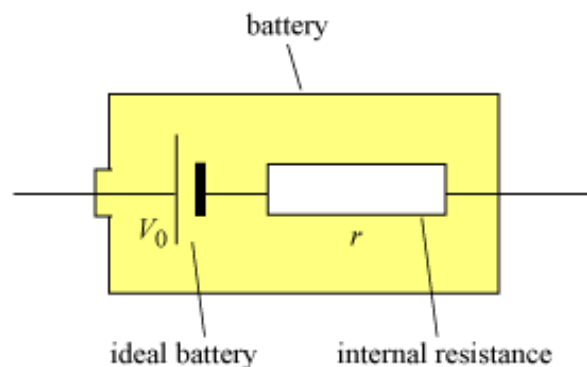
It is vital to ensure that replacement of an internal combustion engine (four stroke engine) with battery cells will provide comparable power output without compromising total weight and load distribution of the vehicle. For this reason the cells should imbue a high specific energy density so that maximum power output can be achieved whilst minimising weight requirements on the watercraft. On average lead-acid batteries, despite their low costs and popular application as automotive batteries, are incomparable to the superior energy densities of Nickel Cadmium, Nickel Metal Hydrate and Lithium Ion counterparts [8].

Referring to the above figure compared to lead-acid, Nickel and Lithium Iron cell variants have 140% and 280% higher energy densities respectively. According to Siddique A Khateeb, current technologies have been able to provide Lithium Iron cells with up to four times the energy density, proving to be ideal for electric vehicle application when considering range, acceleration and life cycle [8]. Furthermore, compared to Nickel Metal Hydride batteries, Lithium Iron cells possess 200% higher energy densities again proving to be more suitable for applications requiring the propulsion of electric vehicles for increased mileage and higher instantaneous torque values.

4.1.3 INTERNAL RESISTANCE

Internal resistance is another parameter of great importance as it dictates the batteries' total cycle life and the cell's overall performance during charge and discharge cycles. It is important to note that internal resistance is measured as a purely ohmic value assuming that the battery cell itself is a conductor. When considering a singular cell, internal resistance constitutes of ohmic, inductive and capacitive resistance values within the cell. The figure below illustrates the concept of the intrinsic resistance (internal resistance) that all electrochemical cells possess:

Figure 3: IDEAL BATTERY MODEL (ENERGIZER 2010)

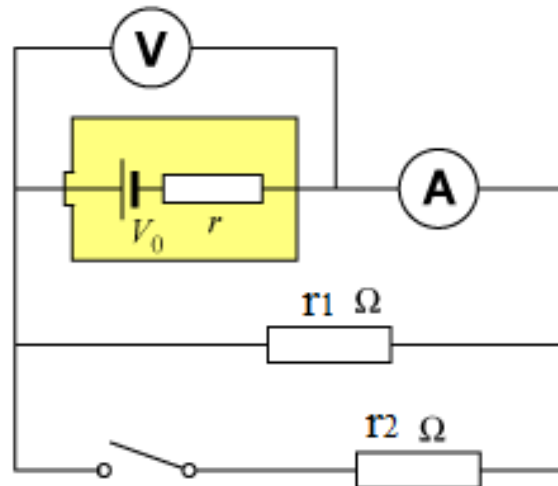


With the battery cell being assigned as an emf (electromotive force) we can thereby, as shown by figure three, model the cell according to an ideal voltage V_0 (ideal battery voltage) in series with a resistor r . This ideal voltage V_0 in most cases will be lower than the voltage normally stipulated by the battery manufacturer since the actual potential difference between anode and cathode plates will vary according to the resistive forces within the battery casing. With discharge of the battery current, I will be drawn to represent a potential difference governed by ohm's law as Ir . As a result of this, the total potential difference between anode and cathode can be calculated as equal:

$$V = V_0 - Ir \quad [2]$$

This indicates the inverse correlation between the current and total electromotive force of an electrochemical cell. Calculation of internal resistance can be undertaken through the adoption of the voltage drop method whereby an equivalent circuit model is developed as shown in figure four below.

Figure 4: EQUIVALENT CIRCUIT FOR VOLTAGE DROP METHOD



Equation [2] can be utilised to govern the voltage drop across the external sides of the cell at any point in time as:

$$V_1 = V_0 - I_1 r \quad [3]$$

Assuming that the circuit is de-energised it is expected that resistance in the external circuit due to r_1 and r_2 will decrease and hence provide another different potential governed by equation [2]:

$$V_2 = V_0 - I_2 r \quad [4]$$

Subtraction of equations [3] and [4] will provide the total potential difference as a direct result of the battery internal resistance:

$$V_1 - V_2 = (I_2 - I_1) r \quad [5]$$

Therefore rearranging equation [5] will allow us to obtain the relationship for internal resistance as:

$$r = \frac{V_1 - V_2}{I_2 - I_1} \quad [6]$$

As mentioned earlier, internal resistance is a large determinant in the total runtime that can be achieved by an electrochemical cell's specific discharge rate. It is implied that a lower internal resistance would assist increased mobility of electrolyte ion flow between anode and cathode and therefore provide overall longer run time for a given discharge rate. Higher internal resistance also correlates to larger fluctuation in the supply voltage of the cell and will tend to possess pulse-like behaviour normally identified as "load pulses". Large amplitudes due to such load pulses from increased internal resistance can cause a cell to reach its minimum nominal voltage prematurely.

4.1.4 PEUKERTS LAW

Run time behaviour under various internal resistances can be described through a theoretical approach to modelling battery efficiency. Efficiency factors pertaining to most cell technologies are governed by Peukerts Law [9] (1897 German Scientist), which aims to account for losses due to internal ohmic, inductive and capacitive resistances through a mathematical model.

$$t = H \left(\frac{C}{IH} \right)^k \quad [7]$$

- ✚ t represents the run time in hours for the particular battery assuming a specific discharge rate.
- ✚ H stipulates the rated discharge time in hours. As an example 10,000mAh battery with a 3C discharge rate would equal 0.33.
- ✚ C represents the cell's normal capacity at a 1 ampere discharge rate expressed in A-h.
- ✚ I governs the actual discharge rate of the cell comparative to 1 ampere which is thus a dimensionless constant.

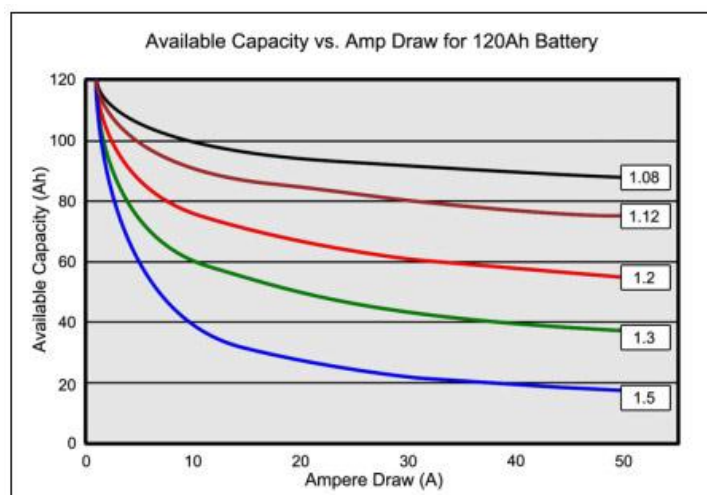
✚ k gives the Peukert's constant which is dimensionless and is characteristic of the particular battery technology used (i.e. NiCd, AGM, Flooded cell, LiFePo4) as well as the ohmic resistances within the cell. Such a value is usually provided by the manufacturer of the cell as it can only be determined through cell simulation utilising a galvanometer.

Peukert's law as explained above will take into account all relevant internal losses due to ohmic resistances. A Peukert's constant close to (1) indicates an extremely efficient battery implying minimal ohmic losses due to internal resistance, whereas one would expect an increase of this value over (1) to indicate a highly inefficient battery with higher ohmic losses. Equation [7] adjuncts an exponential relationship between the Peukert's constant and the cells stipulated run time. Theoretical studies have shown Lithium Iron cells to have 96-99.3% efficiency with a respective Peukert's constant of 1.05 to 1.08 whereas its Lead-acid counterpart possesses 75-88% efficiency with a respective Peukert's constant of 1.1 to 1.3. Whilst Peukert's law aims to mathematically model the efficiency of a battery based on the cell's inherent ohmic resistances, the model does not take into account the following factors which are known to be highly correlated to the overall performance of the cell:

- ✚ Thermal runaway and transient heat effects due to electrochemistry/operation.
- ✚ Battery Shelf life which would entail Peukert's constant to be positively correlated to aging of the battery.
- ✚ Self-discharge due to internal chemical reduction of nominal battery capacity.

Figure 5 below provides an illustration as to the available cell capacity with respect to the current drawn (Ampere) at variable Peukert constants.

Figure 5: AVAILABLE CAPACITY AGAINST AMPERE DRAWN FOR 120Ah (BATTERY UNIVERSITY 2011)



Observation of figure five provides insight into the behaviour of an electrochemical cell with respect to an increased Peukert's number. Higher constant values such as 1.3 and 1.5 indicates a steep slope with nominal capacity decreasing at a more rapid rate as comparative to those with a higher efficiency rate given by a 1.08 and 1.12 Peukert's constant. Lower values of Peukert's constant imply an extremely efficient battery cell with minimal internal losses due to ohmic resistances which thereby give flat band characteristics.

Both batteries with 1.08 and 1.12 have a very gradual negative gradient suggesting a slow discharge and thus longer run time before reaching minimum cut-off voltage. Whereas a Peukert's number of 1.3 and 1.5 have a rapid decrease in the nominal capacity of the cell displayed through the high gradient. This indicates that increasing values of Peukert's constant for a particular cell implies a higher value for its inherent internal impedance.

4.1.5 SIMULATION OF PEUKERTS LAW

In order to illustrate such a phenomena, Ansys Simplorer can be utilised to study the transient behaviour of three individual cells with varying internal resistances. The following simulation package allows the user to create an equivalent circuit model with user-defined input values. For the purpose of this simulation, a simple circuit was initially developed using Simplorer circuit modeller, which was then imported into the Ansys simulation environment. The singular cell was assumed to have the following basic input parameters:

Table 2: ANSYS SIMPLORER SIMULATION INPUT PARAMETERS

Cell Electrochemistry	Lithium Ion Phosphate
Nominal Cell Voltage	3.2V
Cell Capacity	10,000mAh
Continuous Discharge Current	3C (30A)
Minimum Operational Voltage	2.5V
Ambient Simulation Temperature	25°C

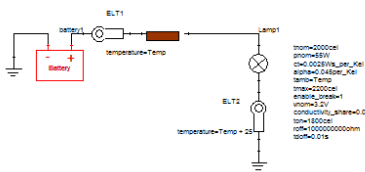
Using such input parameters, an equivalent circuit model was initially developed on Ansys Simplorer to be tested as shown below in figure six. This circuit was modified after each simulation in order to vary the value of internal resistance.

Figure 6: ANSYS SIMPLORER SIMULATION ENVIRONMENT

Automotive Library

Eyelet Terminal Model

Different connector temperatures lead to different voltage drops.



battery1.battery Properties: example elt - example elt

Parameter Values | General | Symbol | Quantities | Signals | Property Displays

Value Optimization Tuning Sensitivity Statistics

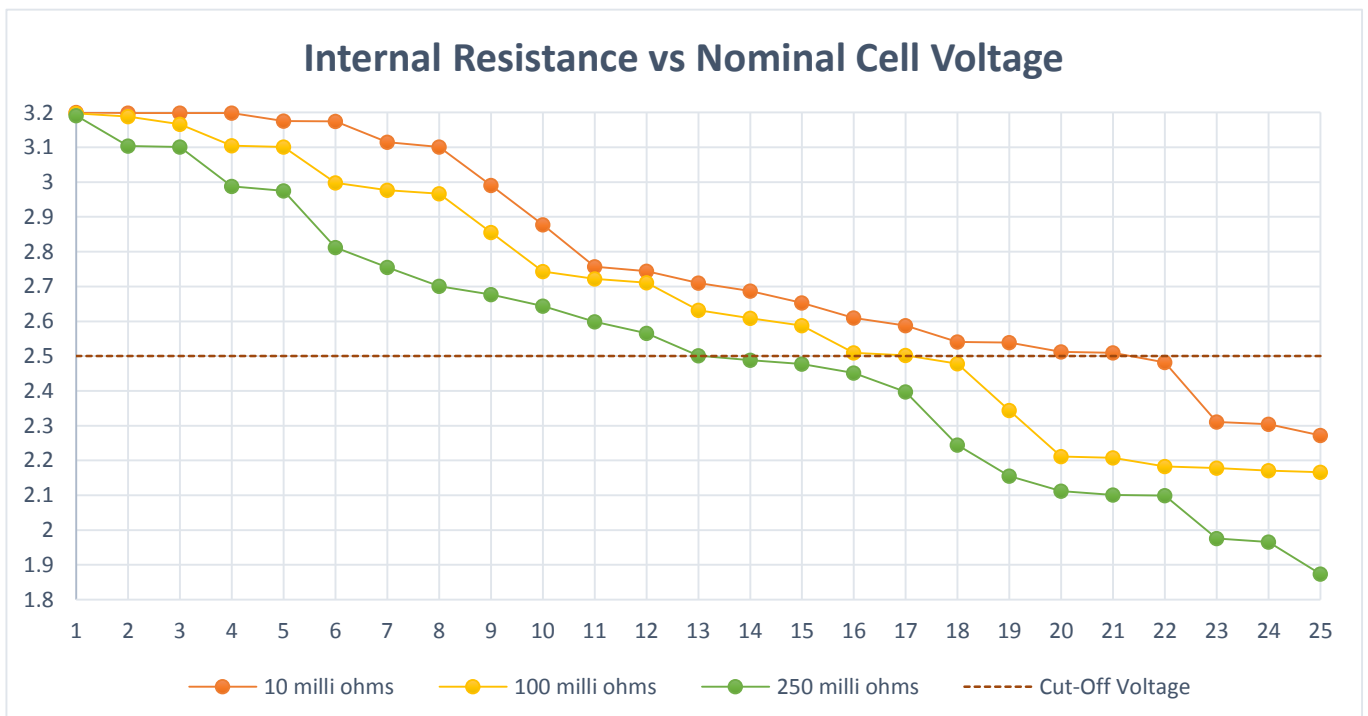
Name	Value	Unit	Description	Callback	Overide	Direction	Show Pin	Sweep	SDB
vnom	3.2	V	No-Load Voltage	...	<input checked="" type="checkbox"/>	In	<input type="checkbox"/>	<input type="checkbox"/>	<input type="checkbox"/>
rin	0.01	ohm	Internal Resistance	...	<input checked="" type="checkbox"/>	In	<input type="checkbox"/>	<input type="checkbox"/>	<input type="checkbox"/>
i	0	A	Terminal Current	...	<input type="checkbox"/>	Out	<input type="checkbox"/>	<input type="checkbox"/>	<input type="checkbox"/>
v	0	V	Terminal Voltage	...	<input type="checkbox"/>	Out	<input type="checkbox"/>	<input type="checkbox"/>	<input type="checkbox"/>

Show Hidden

OK Cancel

Following the development of an equivalent circuit model, a simulation profile was created adopting the input parameters outlined in table 1. Internal resistance was varied for each simulation to study the total time taken to reach the cells cut-off voltage. Values of internal resistances studied were; 10 mΩ, 100mΩ and 250mΩ. Results obtained from running each of the three simulations are displayed below in figure 7.

Figure 7: INTERNAL RESISTANCE VS NOMINAL CELL VOLTAGE



Time (Minutes)	Cell Internal Resistance		
	10mΩ	100mΩ	250mΩ
11	2.757	2.722	2.599
12	2.744	2.711	2.566
13	2.71	2.632	2.501
14	2.687	2.609	2.488
15	2.653	2.588	2.477
16	2.61	2.509	2.451
17	2.588	2.502	2.397
18	2.541	2.478	2.244
19	2.539	2.344	2.155
20	2.512	2.211	2.112
21	2.509	2.208	2.101
22	2.482	2.183	2.099

Figure 8: TABULATED RESULTS

4.1.6 SIMULATION RESULTS OF PEUKERTS LAW

Results obtained in the above graphs shows a negative correlation between internal resistance of a battery and its total run time. It is clear that with higher ohmic resistance, cut off voltage of the cell is reached much sooner. The cell with an internal impedance of 10mΩ has a total run time of approximately 21 minutes as shown in the above table. On the other hand there is significant performance degradation when internal resistance increases to 100 mΩ and 250 mΩ for the same cell. Run time before cut off voltage is reached, reduces to 16 minutes and 13 minutes when cell resistance is 100 and 250 mΩ respectively. This is rather concerning as the simulations do not account for excessive thermal effects that would further negatively impact the run time before cut off voltage is reached . Based on such results it is highly advisable that selection of a suitable battery cell is based on minimal internal resistance preferably in the range of 5-10 mΩ.

Using Peukert's law, a Theoretical value for the above Lithium Iron cells can be obtained assuming the following inputs: Peukert's constant k of 1.08, nominal cell capacity of 10,000mAh, discharge current of 30A and rated discharge time of 0.33 (H) hours. This provides the following equation:

$$t = 0.33 \left(\frac{10}{0.33 \times 30} \right)^{1.08}$$

$$\therefore t = 0.33363 \text{ Hours} = 20.01 \text{ Minutes}$$

Using Peukert's theoretical value a comparison between values obtained in the simulation conducted can be made. Results obtained in the simulation indicate that with the use of a cell that has an internal impedance of 10mΩ, total run time is approximated to be 21 minutes. Such simulated results are consistent with Peukert's theoretical model with only an error of only 4.94%.

4.2 CYCLE LIFE

Capacity of an electrochemical cell is directly correlated to the cycle life, whereby with each cycle the overall cell capacity (mAh) is expected to degrade. One cycle is defined as a batteries phase change from fully charged to fully discharge. Capacity retention as well as the cell's lifetime are largely dependent on both the structural stability of the electrode materials and electrochemical behaviour. Factors such as ion diffusion within the electrolyte and anode/cathode, electrolyte decomposition and interfacial properties all dictate a cell's ability to retain its nominal fully charged capacity. It is inevitable that during normal operation of any cell technology there will be a gradual loss of nominal current capacity due to discharge and charge cycles and normal operation.

There is strong evidence to suggest that increased discharge and charge rates can accelerate the overall decrease in the nominal capacity of the cell over its lifetime (IEEE) [10]. With respect to figure 4, in the comparison of various battery technologies, it is assumed that each of the tabulated cells run through numerous cycles to 80% DOD. Discharge to 80% indicates Lithium Iron to have superior cycle life, with Lithium Ion Phosphate having an average cycle of 1500 before failing to meet its performance criteria. On the other hand, Nickel based cells (Nickel Metal Hydride and Nickel Cadmium are relatively similar to lead-acid technology with an average of 400 and 1000 cycles respectively. When considering the recreational use of the particular project vehicle it will be expected that normal operational use may mean discharges of the cells at 90% DOD or even 100% which will mean a further reduction in the total amount of cycle lives available. Furthermore, according to design and implementation requirements in FEL stage 2, cells are to be installed within an enclosure which will not be easily accessible for regular cell replacement. As a result, ensuring voluminous cell cycle life

is an important consideration in choosing a particular battery technology. From the tabulated information and design criteria in this dimension Lithium Iron Phosphate cells provide maximum cycle life and therefore would be the most ideal when considering such a factor.

Experimentation by Jason Li and Johnson Winnick at the Georgia Institute of Technology has shown the relationship between nominal capacity of a lithium ion cell and the number of cycles the cell undergoes. Prismatic Sanyo UF653467 lithium ion batteries with a nominal capacity of 930 mAh were utilised and 286 discharge-charge cycles were conducted with a discharge rate at 1C from 4.1V to 3.0 V representing a 26.82% DOD [11]. Discharge and charging rates were kept at a constant 0.5 Ah. Life cycle parameters were then observed using a potentiostat (EG&G PARC model 273 A) and a lock-in amplifier (EG&G PARC model 521 C) with the simulation being monitored via impedance software Model 398.

Results obtained by the following experimentation can be observed in figure 9 which highlights the degradation of nominal cell capacity with increased cycles.

Figure 9: CYCLING PERFORMANCE OF LITHIUM IRON BATTERY AT DISCHARGE OF 1C (4.1-3V) (J LI ET AL 2001)

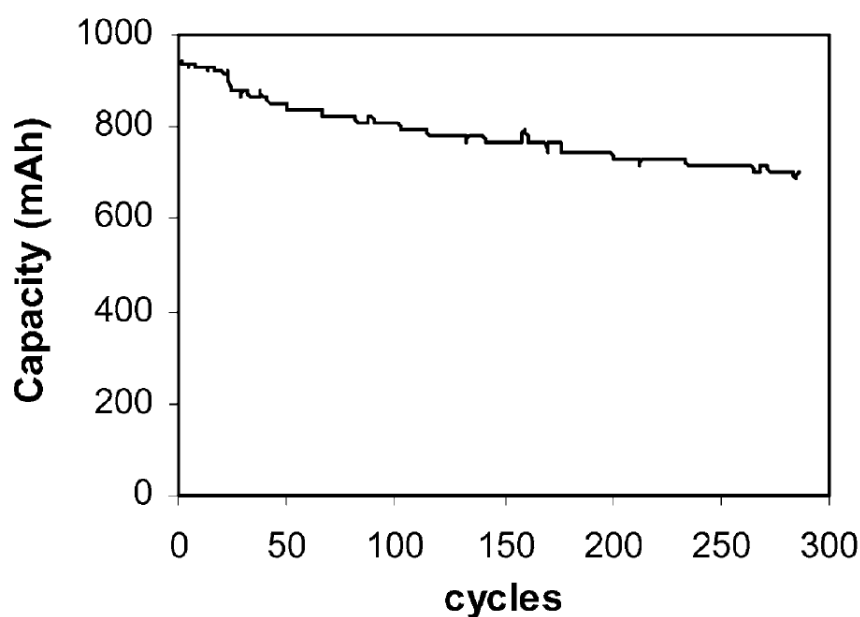


Table 3: DISCHARGE CAPACITY OF LITHIUM IRON CELL AT DIFFERENT CYCLE NUMBERS

Cycle Number	0	40	286
Discharge Capacity (mAh)	1005	972	703

Reference to both figure 8 and table 3 suggest a strong negative correlation between nominal cell capacities with increased discharge-charge cycles. Furthermore, such degradation in the cell's maximum performance over time is further jeopardised by other factors that the above experiment does not take into account, including:

- ✚ Thermal runaway and excessive thermal effects.
- ✚ Unbalanced cell loads and charging.
- ✚ Variance in DOD% at each cycle when considering normal application of cells. In this particular case, the watercraft when used may cause erratic varied amounts of capacity depletion depending on user controls and weather conditions causing increased discharge rates.

4.3 THERMAL RUNAWAY

Whilst memory effects are a prevalent problem in older battery technologies such as Nickel and Lead-Acid based, Lithium Iron batteries are minimally affected by these factors [12]. Memory effect occurs when the nominal capacity of a cell is significantly reduced as a result of shallow discharge and charge cycles. Lithium ion on the other hand is immune to such a phenomena and therefore represents an ideal cell in the application for recreational watercrafts where DOD cycles can vary according to each use of the vehicle.

Thermal runaway and excessive thermal loads have a large impact on the cycle life of all sealed battery cells. When sealed cells are exposed to excessive ambient heat loads and overcharging, oxygen recombination will take place at the cathode which results in an exothermic reaction [13]. Hess's law identifies that this recombination process has a net enthalpy of zero and therefore all heat produced within the internal membrane of the cell is of Joule origin. As a result of this occurrence (thermal runaway) there is an increase in the displacement of electrolytes within the inter-cell walls which causes substantial gains in the internal resistance of the battery [13]. Essentially what this implies is the inability for a cell to effectively dissipate the heat generated within the cell whereby the rate of heat generation surpasses its heat dissipation capacity.

For batteries such as NiMH, NiCd and Lead-acid, studies have shown charging efficiency is greatly reduced when such cells are exposed to temperatures exceeding 60 degrees Celsius. It is suggested that such battery technologies are to have controlled charging and termination implements to ensure long cycle life and efficient operation. Whilst Lithium Iron cells are also prone to reduced efficiency when exposed to temperatures above 60 degrees, there is

minimal impact on the overall cycle life of these battery cells. With consideration to design proposals and battery module location for the watercraft, it would be expected that cells within the watercraft body will be exposed to excessive temperatures during normal operation.

4.4 OVERCHARGING TOLERANCE

As per front end engineering the project requirements for battery safety shall require the use of a power charger with the following specifications;

Table 4: BATTERY CHARGING SYSTEM SCOPE REQUIREMENTS

Parameter	Value	Unit
Input Voltage	230V	Vac
Voltage Range	150V-250V	Vac
AC Voltage Frequency	55-65	Hz
Charge Voltage	72-108V	Vdc
Float Voltage V_{max}	108V	Vdc
BMS Limit Current	1.5-3A	A

With design requirements underlined in FEL1 phase 1, the inclusion of a power charger with an incorporated V_{max} overcharge limiter is crucial. Furthermore, the scope of design stipulates the need for an effective BMS (battery management system) incorporated into the design to allow for appropriate cell balancing in the event of an unbalanced battery module. Therefore a factor such as overcharging tolerance is not highly important in the suitability criteria for an appropriate cell due to the inclusion of such an instrument into the overall design of the watercraft charging system.

4.5 CELL MAINTENANCE

Maintenance of the battery cells should be minimal due to the placement of battery modules within a confined area of the watercraft. Whilst under FEL1, efforts shall be made to allow for a fully modular design for battery modules, it is expected that battery modules will be

placed within an enclosure and disassembly of cell modules shall only occur under one of the following conditions:

- ✚ Fire Hazard (shorting of battery module circuit/ general fire).
- ✚ Battery circuit fault as per BMS fault detection.
- ✚ Physical/chemical damage of watercraft and or damage to enclosure/individual cells.
- ✚ Cell replacement due to end of cycle life/malfunctioning.
- ✚ General safety breach causing severe damage to personnel and vehicle.

Both Nickel and Lead-Acid based batteries require regular maintenance (with the exception of NiMH) [14]. Both batteries require regular attention to electrolyte balancing and float charging to ensure prolonged cycle life. Furthermore, lead-acid batteries need to have cathode and anode plates re-torqued on a monthly basis and de-sulfation must be carried out regularly to prevent grid corrosion [14]. Lithium Ion cells on the other hand are minimally invasive in terms of maintenance and do not require any intervention to maintain cycle life [14].

However, utilisation of a suitable BMW system and charge protection is vital to ensure cycle life is not compromised due to overcharging and excessive heat loading. As per the design proposal for battery enclosure, access to battery modules will prove to be difficult in the event that regular maintenance is required for the proposed electrochemical cells. Therefore Lithium Iron cells would be the most favourable from such battery technologies.

4.6 SAFETY

Operation of the watercraft under normal use must comply with the safety regulations of SAE international. These rules govern the design and implementation of all HEVs and therefore adoption of a particular power source shall incorporate the use of circuit protection. SAE standard J1495 “Test Procedure for Battery Flame Retardant Venting Systems” outlines the prohibition on the use of lead acid battery cells as a continuous power source other than for providing power for starting, lighting and ignition [15]. Due to the high toxicity of the chemicals discharged from both lead-acid and Nickel Cadmium battery cells, use of these battery technologies would not conform to such a standard due to the risk they possess in the event of a fire, circuit fault or accident. Lithium Ion cells on the other hand have low toxicity in the chemical composition of the cell and thus would be an ideal candidate in order to conform to such design standards. Furthermore SAE J1797 “Recommended Practice for

Electric and Hybrid Electric Vehicle Battery Systems Crash Integrity Testing” mandates the requirement of external circuit protection beyond individual cell fuses [15].

Whilst Lead-acid and Nickel-based batteries feature fused circuit protection, Lithium Iron cells lack internal circuit protection in the event of faults or fire hazards. However, with conformance to SAE J1797, irrespective of internal circuit protection, additional safety systems must be implemented when utilising all such battery technologies [15]. Therefore whilst Lithium Iron cells do not have adequate internal circuit protection systems, the adoption of such a standards would favour the use of Lithium Iron cells for the watercraft.

5 IDEAL ELECTROCHEMICAL CELL

After consideration is given to the aforementioned performance, safety and design requirements, the use of lithium ion phosphate cells proves to be the most suitable electrochemical cell for such an application. With its superior energy density, DOD characteristics, cycle life, minimal internal resistance and low toxicity, this battery technology is the best power source to ensure maximum performance of the personal watercraft. Furthermore lithium ion phosphate cells have traditionally conformed to all design standards governed by SAE International under SAE J2929 [16]. Therefore, conforming to these standards is crucial to the project’s objective to create a marketable watercraft.

Sponsorship initiatives had primary influence on the models of lithium ion phosphate batteries that were considered. EV Works Electric Vehicle Specialist Ltd was the primary sponsor for the REV Jet Ski project and therefore battery modules were sourced from this company. Project deliverables and milestones as per the project gnat chart were also important factors in ensuring battery modules could be sourced with minimal lead time. However design consideration as per the project scope and performance criteria were also taken into account when selecting the most suitable LiFePO₄ cell.

Two models were initially reviewed for design requirements so that comparisons could be made to choose the most suitable cell from the two models. The table below provides information on each of the two cells: Winston Battery WB-LYP100AHA LiFePO₄ and Headway 38120 10Ah LiFePO₄ cell

Table 5: LiFePO4 CELL MODEL COMPARISON

Model Number :	Headway 38120 10Ah	Winston Battery WB-LYP40AHA
Pricing (Per Individual Cell)	\$18AUD	\$52AUD
		
Electrochemistry	LiFePO4	LiFePO4
Nominal Capacity	10,000mAh	40,000mAh
Nominal Voltage	3.2V	3.2V
Internal Impedance	< 6mΩ	< 19mΩ
I_{max} Charge	2C (20A)	0.3C (3A)
V_{max} Charge (Overcharge Threshold)	3.65± 0.05V	4.25± 0.05V
Max Continuous Discharge Current	3C (30A)	3C (30A)
Max Peak Pulse Discharge Current	10C (100A)	10C (100A)
Max Discharge Stop Voltage (37% DOD)	2.0V	2.0V
Dimensions	Height : 122± 1mm (132±1mm) Diameter : 38 ± 1mm	Height : 188± 1mm (190±1mm) Width : 116± 1mm Thickness : 46± 1mm
Weight	330g	1600g ± 100g
Operating Temperature	Charge : 0-45°C Discharge : -20 - 60°C	Charge : -25-75°C Discharge : -25 - 75°C

Cycle Life	@ 1C 100% DOD : 1500 cycles	@ 1C 100% DOD : 1500 cycles
	@1C 80% DOD : 2000 cycles	@1C 80% DOD : 2000 cycles

5.1 CELL MODEL COMPARISONS

Comparisons between both LiFePO4 models show very similar specifications in terms of both cycle life and operating temperature. Whilst Winston WB-LYP40AHA imbues a higher nominal capacity at 40,000mAh as compared to Headway 38120 10,000mAh, lower internal resistivity of the Headway lithium ion phosphate cell makes it a much more favourable model. As discussed earlier, higher internal resistance increases the effects of both thermal runaway and excessive exothermic heat production. Peukert’s law suggests that a direct result of this is degraded operational time of the cell through progressive life cycles. As per the scope requirements for front end engineering design, all enclosures including that of the battery modules shall be at an IP rating of 68. This would suggest minimal ventilation and airflow within the internal body of the battery enclosure. Therefore, excessive heat due to thermal runaway would not be favourable as heat dissipation would be extremely minimal without the utilisation of a suitable airflow/water cooling system within the enclosure.

5.1.2 CONSIDERATIONS

Another important consideration is the minimization of load distribution within the frontal body of the Jet Ski. Prior front end engineering design had finalised the location of battery modules and their enclosure. Load distribution of pre-conversion Jet Ski hull assembly layout needs to be maintained during the conversion process to mitigate risk of unbalanced loads. Figures 9 and 10 below provide insight into the front end engineering proposal in the location of main equipment: 3 Phase 2 Pole Induction full submersible motor, Battery modules/Enclosure, DC-AC Motor Controller, Cooling System and water pump.

Figure 10: PRE-CONVERSION TECHNICAL ASSEMBLY LAYOUT

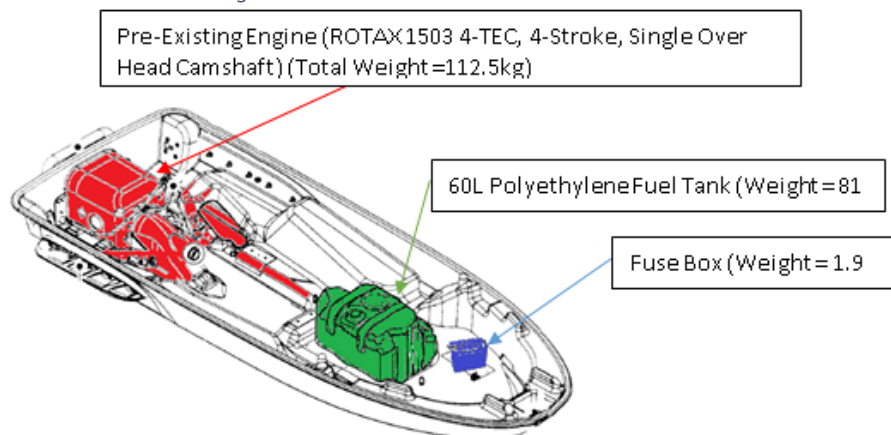
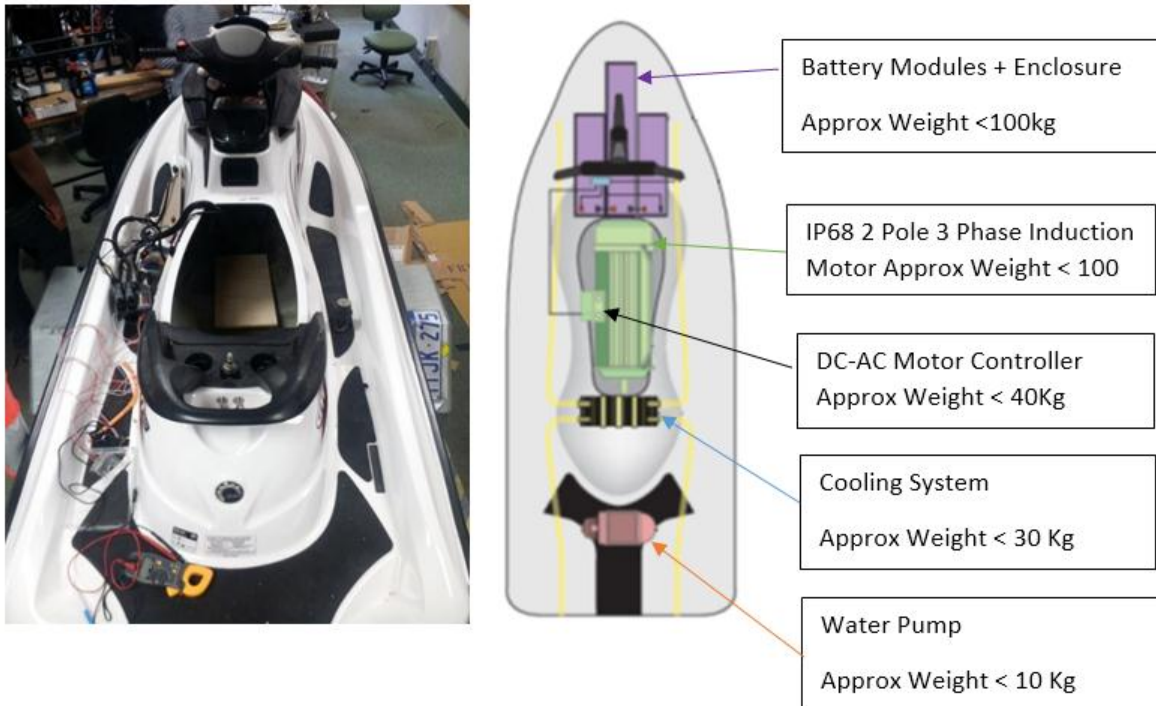


Figure 11: PRELIMINARY CONVERSION HULL EQUIPMENT ASSEMBLY LAYOUT (RILEY WHITE 2013)



With respect to figures 10 and 11, the proposed symmetrical load distribution of assembly conversion limits battery modules and its enclosure to not exceed a total weight of 100Kg. With such design requirements the use of Winston WB-LYP40AHA would not seem feasible due to its excessive weight as a single cell (1.6kg). In order to maximise attainable mileage from a battery power source, total nominal voltage applied to motor controller should be close to 115V as this is the limiting safety factor. UWA Electrical Safety and Installation guidelines section 4.2.4 governed under the AS/NZS 2243.7-1991 requires the use of ELV (extra low voltage) battery systems not exceeding 50V AC or 120V ripple feed DC (also as per AS/NZS 3000: Australia New Zealand Wiring Rules) [5]. In accordance with such safety and wiring guidelines, the use of ELV battery system shall mean that the maximum voltage that can be implemented is 120V DC.

5.2 TORQUE POWER CAPABILITIES

Preliminary engineering design for the 2 Pole 3 Phase induction motor (JS102-50KW 135Hz) is another limiting factor in the nominal voltage of the proposed power source. Maximum torque that can be achieved through the following AC induction motor can be calculated through the use of both nominal current vs torque curves provided by the manufacturer (Submersible Motors Pty Ltd) as well as theoretical synchronous speed calculation. Synchronous speed can be defined as the velocity with which the stator within the magnetic field rotates at and hence determines the speed of the rotor. Synchronous speed (SS) is

mathematically modelled as a function of the frequency of the power source as well as the number of poles (pairs) enclosed within the motor. The relationship in order to derive ideal synchronous speed of the motor is given as:

$$SS = \frac{(120 \times f)}{P} \quad [11]$$

- SS : The ideal synchronous speed of the rotor given in (RPM)
- f : The frequency of the power source (cycles per second)
- P : Number of poles within the motor (pairs)

Using equation [11] and the specification sheet for the supplied AC induction motor (JS102-50KW), the ideal synchronous speed of motor is:

$$SS = \frac{(120 \times 135)}{2} \quad \therefore SS = 8100 \text{ Rpm}$$

5.2.1 CALCULATION OF MAXIMUM TORQUE

Whilst theoretical value for the obtained synchronous speed is 8100 rotations per minute, it should be noted that the rotor in any AC induction motor is not able to turn at its theoretical synchronous speed largely due to the fact that it must induce an EMF (electromagnetic force) inside the motor. This would mean that the rotor is moving at a slower rate than the specified synchronous speed calculated earlier. If rotor speed was equivalent to the calculated synchronous speed it would mean that an EMF would not be induced within the motor and hence there would be no movement by the rotor in such a case. In any event, where the rotor speed is significantly decreased an EMF would again be induced within rotor bars which will allow it to rotate at a speed slower than the synchronous speed. The mathematical relationship between rotor speed and synchronous speed is known as slip. Slip is expressed as a percentage of the synchronous speed whereby:

$$\%S = \frac{(SS - RS)}{SS} \times 100 \quad [12]$$

- %S : Percent Slip
- SS : Synchronous Speed (RPM)
- RS : True Rotor speed (RPM)

Given equation [12] we can then rearrange the following to obtain the true rotor speed.

The calculated synchronous speed and percentage slip value provided by the manufacturer as per specification sheet in Appendix (B) is equivalent to 1.9747%. Therefore rearranging equation [12] we express true rotor speed as:

$$RS = (1 - S) \times SS \quad [13]$$

$$RS = (1 - 0.019747) \times 8100$$

$\therefore RS = 7940.05 \text{ RPM}$ – Losses due to friction windage and heat

However, losses due to friction, windage, heat and other stray losses means that this value for rotor speed will be reduced by the efficiency rating of the motor as specified by the manufacturer at 95.007% giving the real rotor speed at 7543.04 RPM.

Given these statistics, we can then calculate the maximum electromagnetic torque which is related to the rated power of the motor P_g which is 50kW specified as per the specification sheet in appendix (B);

$$T = \frac{P_g}{((1 - s) \times W_s)} \quad [14]$$

-T: Maximum rotor torque

- P_g Internal rated power (W)

- S: Motor slip

- W_s : Synchronous angular velocity ($W_s = 4\pi f/ \#$ of poles) where f = power source frequency

Using equation [14] the value for torque is equivalent to 60.133 Newton Metres which will be further reduced due to the stray and frictional losses. Therefore the real value of maximum torque will be equal to 57.13 Newton Metres. Based on these findings, motor torque curves can be utilised to work out the ideal value of input current required to achieve maximum torque and hence provide the watercraft with maximum cruising velocity. Figure 11 and 12 presented below, outline these curves obtained by motor specification sheet.

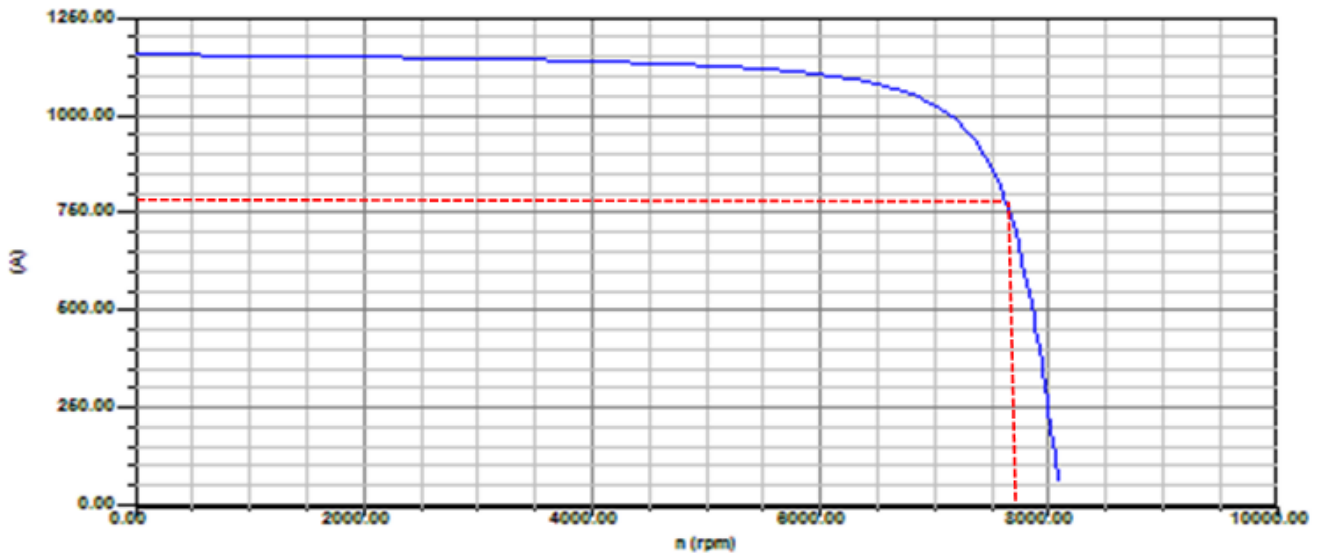


Figure 12 indicates that maximum torque of 7543.04 RPM can be achieved with an applied nominal current of approximately 770 Amps from the proposed power source. Based on such considerations, preliminary materials procurement ensured that a suitable AC Induction motor controller was purchased. Therefore all engineering design ascertaining to the power source was initiated according to the constraints and requirements of the purchased controller.

5.3 POWER DELIVERY

The Curtis 1238-766 DC to AC controller was procured for the following project. This controller is rated to have a nominal battery voltage in the range of 72-96 V DC with a two minute RMS current rating at 650 A at a power rating of 73.6kVa as per the specification sheet on Appendix (C). As per the design requirements outlined in the scope the appendant Curtis motor controller, the model complies with the water ingress standard rated at IP65. To optimise its operating environment an adequate cooling apparatus will be designed.

Maximisation of watercraft efficiency can be achieved by delivering the maximum rated voltage and nominal current to the motor controller so that torque to the motor can also be maximised. Therefore the design solution for the power source involves the use of 30 battery modules connected in series so that a total of 96V ($3.2V \times 30$) can be attained.

5.4 SUITABILITY CRITERIA

More importantly, in order to deliver 770A to the motor controller each module would require the connection of 8 individual LiFePO₄ in a parallel configuration so that maximum peak discharge current of 800A can be delivered to the controller which will then be limited to 650A via the CanBus logic control parameters. Therefore, the final battery module circuitry design stipulates the final design proposal:

- ✚ A single battery module shall pertain to 8 individual LiFePO₄ connected in parallel configuration.
- ✚ Total nominal voltage delivery is to be 96V DC.
- ✚ Maximum Peak Discharge current from entire power source is to be at 800A.
- ✚ 30 Battery modules are to be connected in series configuration to deliver a total of 800A (2 minute peak discharge) and 240 A (continuous discharge).



With such design rules, the most suitable LiFePO₄ cell was determined by project factors such as financial limitations, symmetrical weight distribution and enclosure dimension limitations.

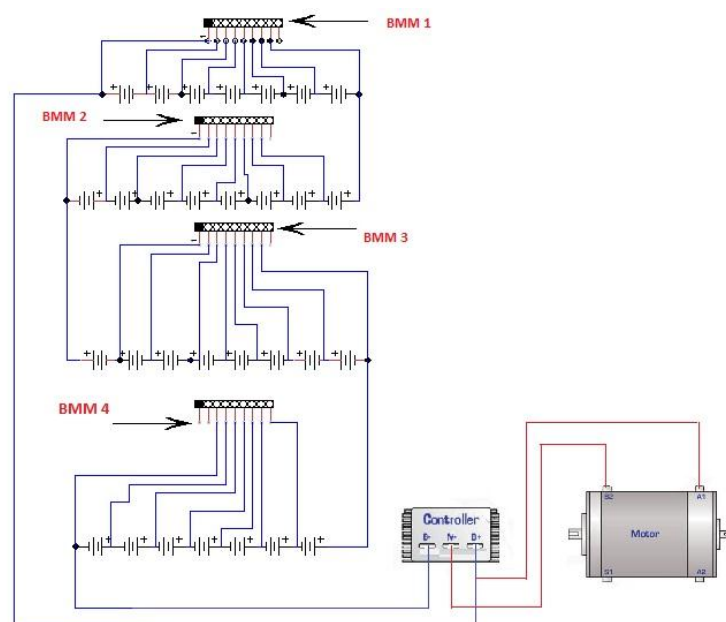
One of the largest factors as mentioned earlier is ensuring symmetrical weight distribution to maintain original balance of the watercraft prior to its conversion. Application of such a battery configuration would mean that using 240 Winston WB-LYP40AHA cells would equal a total load weight of 384Kg. On the other hand the use of 240 Headway 38120 would equal a total load weight of 79.2Kg. It is important to note that these calculations do not take into account the use of bus plates for the interconnections to compile the entire circuit. In this aspect it is clear that whilst Winston WB-LYP40AHA cells imbue a higher nominal capacity at 40,000mAh compared to its Headway counterpart at only 10,000mAh, the weight imposed on the fibreglass cavity may hinder watercraft performance significantly.

Battery box enclosure dimensions were also carefully considered because space confinements within internal cavity limit the size of the power source which can be housed. Again with respect to this design requirement, the use Winston Winston WB-LYP40AHA cells were foregone due to the smaller dimensions and ease of placement that the Headway 38120 cells provide. The use of headway cells from a project costing perspective was also a more favourable option due to the total cost including shipping being equal to \$4570 compared to \$12,730.6

6. FRONT END ENGINEERING LOADING PHASE TWO: CIRCUIT DESIGN

To conform to the design criteria set out in the earlier section, a wiring diagram was adopted to incorporate a suitable battery management system for the power source as required under SAE J2929_20132. Figure 13 below presents the preliminary circuit diagram for the proposed power source.

Figure 13: BATTERY MODULE CIRCUIT DIAGRAM



As can be seen from figure 13, each module will have a voltage of 3.2V connected in series with a total of 30 battery module power sources. Total voltage will thereby be 96V with a total continuous current of 240A. Interconnections between each of the modules will be carried out through the use of copper plated bus plates as shown below.

Figure 14: HEADWAY CELL BUS BAR



Specifications on the bus plates are as outlined in the table below.

Table 6: CELL BUS BAR SPECIFICATIONS

Material Type	Approx. 96% Copper
Thermal Conductivity	401 W/(m.K)
Length	37mm
Screw Insert Diameter	2.5mm
Width	15mm
Thickness	1mm
Weight	150g

6.1 THERMAL IMPACT ON CIRCUIT DESIGN

An important factor in both the efficiency and safety of the battery power source is the minimisation of excessive heat generation from the proposed circuit. With the use of the following cell bus bars as the interconnections for the power circuit, it is important to model the transient thermal effects caused by power loss within the circuit. A risk of fire hazard or even permanent injury/damage to the watercraft equipment, user, and battery modules can occur if the surface heat of the bus bars is excessively high. Therefore it is important to model the behaviour of the surface heat generated on the bus plates as a direct result of power loss through the interconnection plates. In order to do this, a mathematical model was developed so that thermal generation could be minimised by using multiple bus plates for the interconnections.

6.1.1 BUS BAR HEAT CONDUCTION

Having multiple bus plates will ensure that the surface heat generated by power loss and resistivity of the plates will be evenly distributed by the multiple layers of plates on a single interconnect. This will minimise the overall heat generated within the enclosure and thus reduce the risk of fire damage or even personal injury to the user and watercraft.

Power loss due to the transmission of current through the following plates can be modelled as:

$$P_{loss} = i^2 r \quad [14]$$

- P_{loss} : the power loss in watts

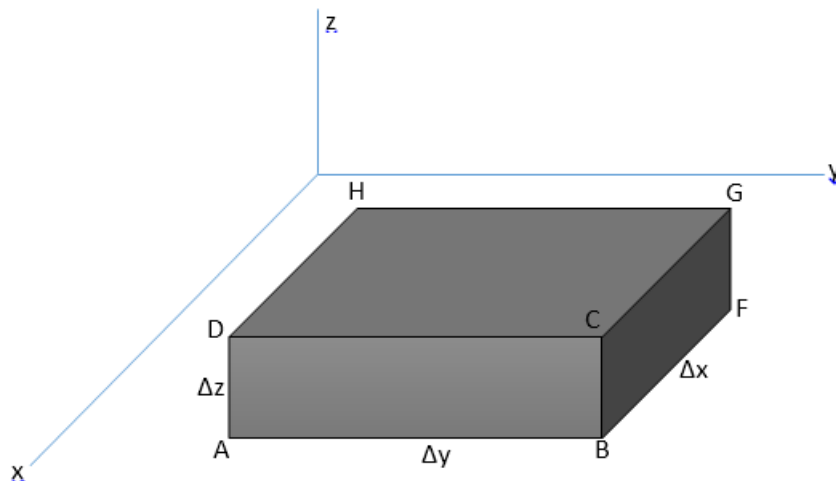
- i : the current through the node/circuit in Amps
- r : the resistance within the conductor/bus bar in ohms (Ω)

Mathematical derivation can be undertaken through the use of partial derivatives to study the flow of heat in the thermally conducting regions of the bus bar. Several facts can be inferred about the governing mathematical equations used:

- a. Heat will flow in the direction of decreasing temperature [17].
- b. Rate of heat flow through a specific area is proportional to the area and the temperature gradient expressed in degrees per infinitesimal distance ($\Delta x, y, z$) [17].
- c. Quantity of heat that is gained or lost by the bus bar as a change in temperature (i.e. change in heat content or thermal energy) is proportional to the mass of the bus bar as well as the change in temperature [17].

Fact b. outlines the use of a proportionality constant k known as the thermal conductivity of the material which in this case is 401 W/ (m.K) (at 25°C). The proportionality constant stated in fact c. is known as the specific heat of the material which will be 0.386 J/gm K (at 25°C). Considering the thermal conditions for an infinitesimal element of conducting bus bar as per figure 18 below:

Figure 15: TYPICAL VOLUME ELEMENT IN A REGION OF THREE DIMENSIONAL HEAT FLOW



Weight of the bus bar material per unit volume can be defined as ρ therefore the total mass of the unit volume is:

$$\Delta m = \frac{\rho \Delta x \Delta y \Delta z}{g} \quad [19]$$

Where g represent the acceleration of gravity constant (9.8ms^{-2}).

We can define u as the temperature at an instantaneous point in time, therefore the change in temperature Δu will be the temperature change that occurs within the bus bar in an infinitesimal time interval defined as Δt which will thereby represent the quantity of heat stored within the bus bar at this time by c :

$$\Delta H = c\Delta m\Delta u = \frac{c\rho\Delta x\Delta y\Delta z\Delta u}{g} \quad [20]$$

Based on equation 20 we can then represent the rate at which heat is being stored by the following equation:

$$\frac{\Delta H}{\Delta t} = \frac{c\rho}{g}\Delta x\Delta y\Delta z\frac{\Delta u}{\Delta t} \quad [21]$$

The source of heat which produces the change in temperature Δt throughout the bus bar element in the particular case is purely from an electrical source. This can be defined as the constant heat flux at an arbitrary infinitesimal area on the surface. Heat density at this area on the surface can be modelled as a relationship between the input power through the bus plate and cross sectional area:

$$P_D = \frac{P_{in}}{C_a} \quad [22]$$

$-P_D$ = the power density in W/m^2

$-P_{in}$ = the power delivered through the bus bar in W

$-C_a$ = cross sectional area in m^2

The thermal gradient is another factor that must be considered in calculating surface temperature at an instantaneous point in time. Thermal gradient provides insight into the direction and the rate of change in temperature around the x,y,z axis at a specific location in the three dimensional space. This value is a constant expressed as K/m . For copper this constant is $1.4 \times 10^{-5} \text{K}/\text{m}$ and thus, the equation for surface temperature for a particular point on the surface can be expressed as:

$$T(\Delta x, \Delta y, \Delta z) = T_0 + \frac{2 \times P_D \left[\frac{\Delta u}{\Delta x y z} \times \left(\frac{t}{\pi} \right) \right]^{1/2}}{k} \quad [23]$$

- $T(\Delta x, \Delta y, \Delta z)$ = the surface temperature at a specific location along the x,y,z three dimensional space in °C

- T_0 = the defined ambient temperature at which the script begins its iterative process. This is expressed in °C

- P_D = the power density as per equation [22]

- t = the instantaneous time at which surface temperature is monitored at, in seconds

- k = the thermal conductivity of the material which in this particular case is 401 W/ (m.K) (at 25°C)

6.1.2 BUS BAR THERMAL MODEL

With the above mathematical model derived, we can adopt a simple Matlab script to analyse the transient surface heat conduction of the bus bar to determine the ideal number of bus plates needed to ensure safe operating thermal conditions within the battery module and surroundings. The final Matlab script used is as follows:

Figure 16: MATLAB SCRIPT FOR MODELLING TRANSIENT THERMAL BEHAVIOUR UNDER VARIOUS NUMBER OF BUS BARS

```
function [out] = BatteryTemp( current, nPlates, initTemp, tInt )

    resCopper = 1.68*10^-8;
    specHeatCopper = 385;
    thermConduct = 401;
    vol = 0.015*0.001*0.037*nPlates;

    totalMass = 8940*vol;

    XSecArea = 0.015*0.001;
    R = resCopper/XSecArea;
    power = (current^2)*R;
    powerDensity = power/(XSecArea*nPlates);

    T = zeros(1, tInt);

    for t = 1:tInt
        res = initTemp + ((2*powerDensity*((1.4*10^-5)*(t-1)/30
)^0.5)/thermConduct);
        T(t) = res;
    end

    X = zeros(tInt, 1);

    for i = 1:tInt
        X(i, 1) = T(i);
    end

    out = X;
```

As stated by the specifications for the motor controller, the maximum 2 minute current rating is 650A and the continuous current supplied will be 240A. Simulations using the above script were used to conduct investigations as to the suitable number of bus bars required to ensure minimal exothermic heat generations. Simulations were conducted under the following assumptions:

- ✚ Ambient Temperature of 25°C.
- ✚ No airflow to battery modules (i.e. still air).
- ✚ External forms of heat generation such as cell thermal runaway and other exothermic heat sources from nearby equipment were ignored.

6.2 SIMULATED RESULTS

The results are graphed as follows:

Figure 17: THERMAL BEHAVIOR AT 240 AMPS

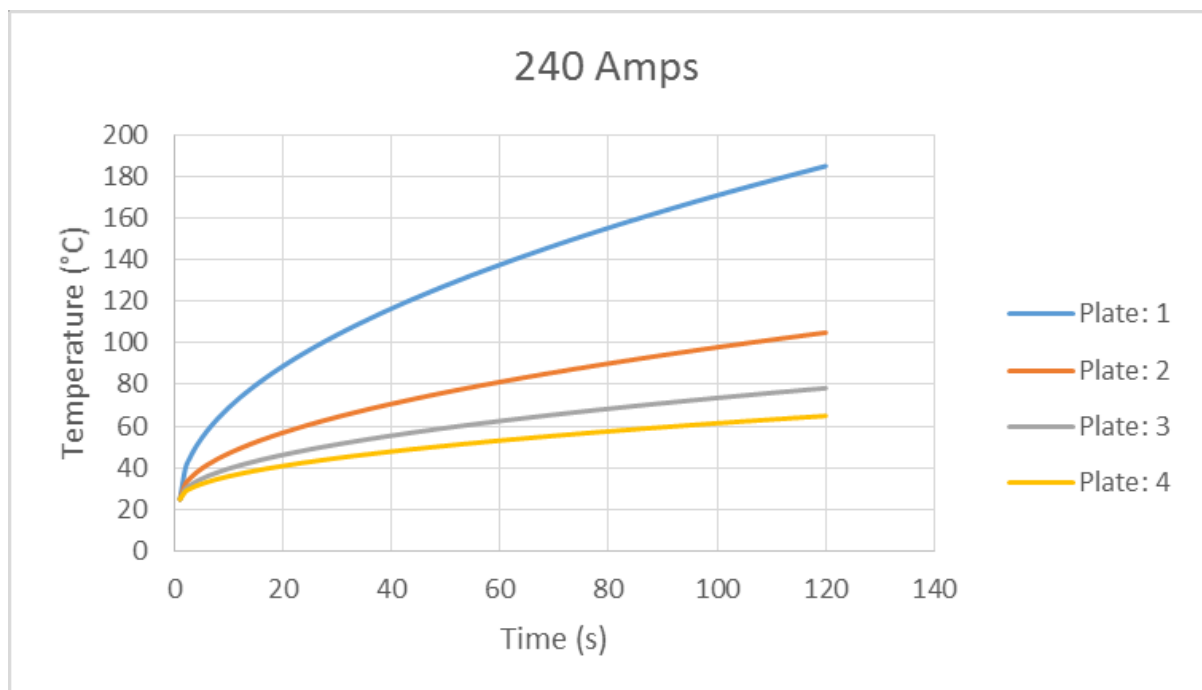


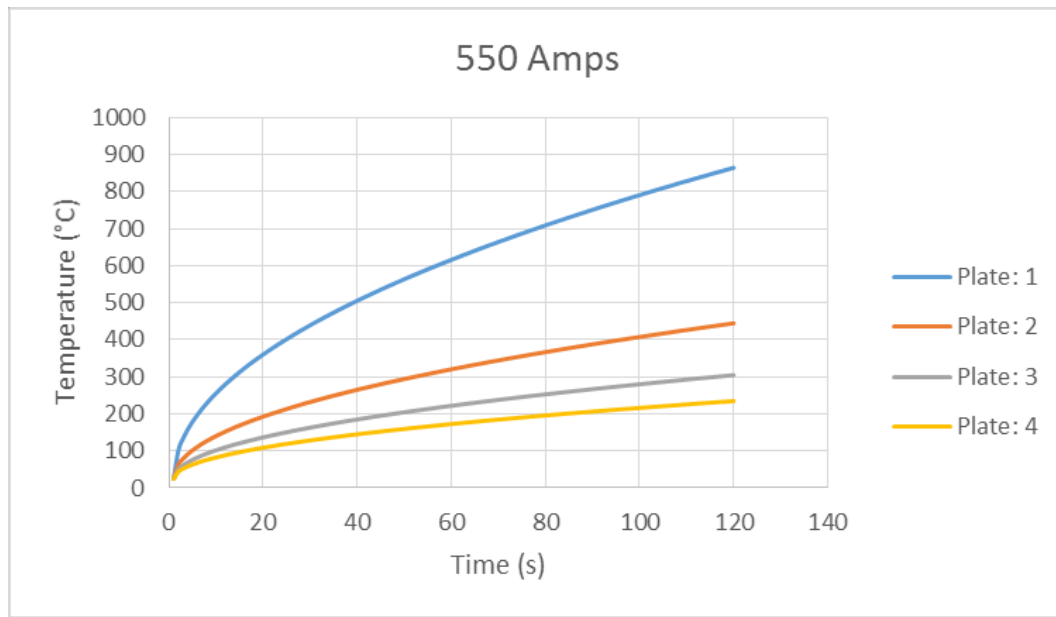
Table 7: RESULTS FOR 240 AMPS

Time (seconds)	Temperature: 1 Bus Bar (°C)	Temperature: 2 Bus Bars (°C)	Temperature : 3 Bus Bars (°C)	Temperature: 4 Bus Bars (°C)
115	181.4554	103.2277	77.1518	64.1139
116	182.1402	103.5701	77.3801	64.285
117	182.8219	103.9109	77.6073	64.4555
118	183.5007	104.2504	77.8336	64.6252
119	184.1766	104.5883	78.0589	64.7942
120	184.8497	104.9248	78.2832	64.9624

Since the continuous nominal discharge current provided by a single Headway LiFePO₄ is equal to 3C (30A), total power source discharge current will be 240A. Transmission of current at this particular value indicates that the use of only one bus bar is insufficient with surface temperature rising to 184.84°C within the 2 minute period. This would greatly jeopardise the overall safety of the circuit but moreover have a negative impact on the long term efficiency and performance of these cells. In order to mitigate fire hazards and efficient battery performance it should be proposed that either 3 or 4 bus bars are used so that temperatures at 78.28°C and 64.96°C can be easily managed via utilisation of a cooling system.

Whilst the use of 4 bus bars would provide the best thermal efficiency, clearance between modules and the enclosure wall places a limitation on the use of 4 bus bars for the interconnections. Therefore battery module construction will incorporate the use of 3 bus plates for circuit interconnections and surface temperatures will be further managed by the use of a water pump or suitable cooling method to maintain the safe operating conditions at approximately 60°C. It is also important to note that the following simulation assumes the continuous discharge of current with the user placing the Jet Ski at full throttle for the entire 2 minute duration. This would be somewhat unrealistic as under normal use it would be expected that the user would relax the throttle intermittently thus allowing further heat dissipation from the conducting surface of the bus bars.

Figure 18: THERMAL BEHAVIOR UNDER 550 AMPS



Time (seconds)	Temperature: 1 Bus Bar (°C)	Temperature: 2 Bus Bars (°C)	Temperature : 3 Bus Bars (°C)	Temperature: 4 Bus Bars (°C)
115	846.6627	435.8314	298.8876	230.4157
116	850.2586	437.6293	300.0862	231.3147
117	853.8389	439.4195	301.2796	232.2097
118	857.4039	441.2019	302.468	233.101
119	860.9536	442.9768	303.6512	233.9884
120	864.4883	444.7441	304.8294	234.8721

Table 8: RESULTS FOR 550 AMPS

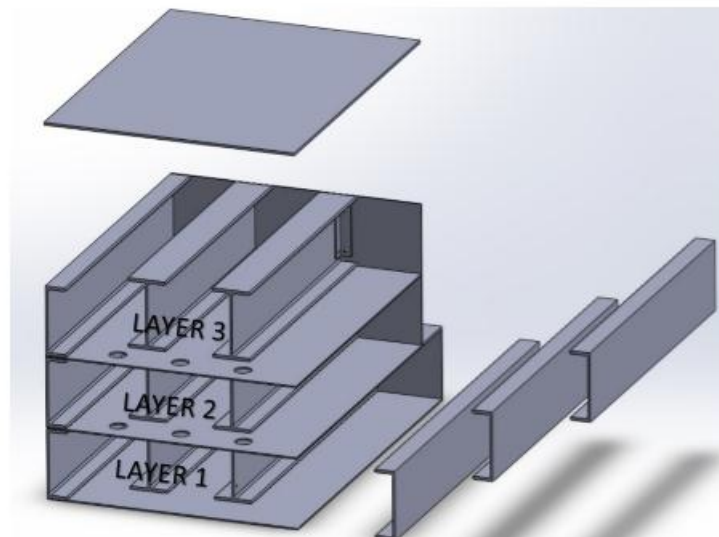
An additional simulation was carried out assuming nominal current delivery of 550A. The use of 3 bus bars suggests a surface temperature of 304.82°C if such a current was delivered for a duration of 120 seconds. Although this is somewhat concerning and would suggest an extremely high risk of fire, programming of the motor controller via CanBus interface would limit the total current from the power source to 240A so that such temperatures cannot be achieved. Also, temperatures sensors integrated into the battery management safety system would also ensure that detection of overheating (above 90°C) would automatically disconnect the circuit via the safety relays.

7. ENCLOSURE DESIGN

Design of battery modules shall be undertaken according to the preliminary floor plan of battery enclosure. Several design revisions were proposed as a suitable enclosure to house the battery modules and final proposal of the battery enclosure had to take account of the following important design considerations:

- ✚ Adequate ventilations between enclosure walls and battery cells.
- ✚ 5mm clearance between anode/cathode plates so that multiple layers of bus bars can be attached as interconnections.
- ✚ Front face of enclosure shall incorporate a 100mm clearance after battery modules to allow for an adequate bending radius for high voltage cables between parallel modules.
- ✚ Height clearance between modules and top enclosure walls are to be 10mm to allow for suitable cooling apparatus and natural heat dissipation.
- ✚ Enclosure shall be fully modular so that maintenance of cells can be carried out through minimal effort.

Figure 19: BATTERY BOX FINAL REVISION EXTRUDED VIEW (RAJINDA JAYAMANNA 2013)



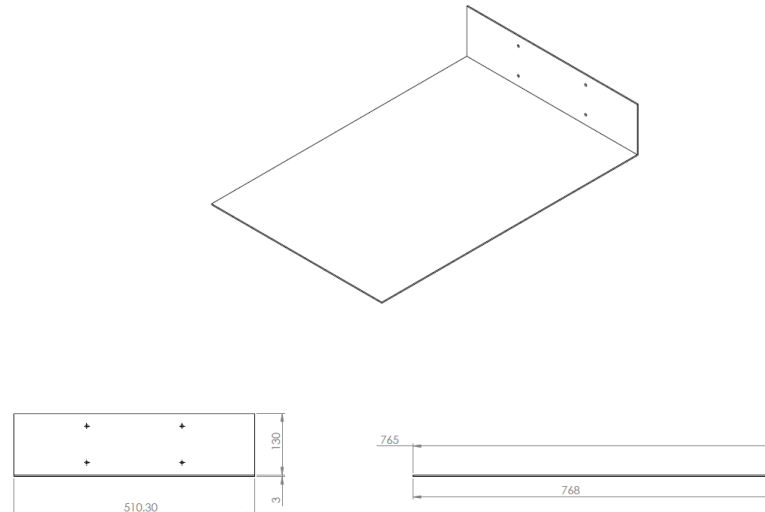
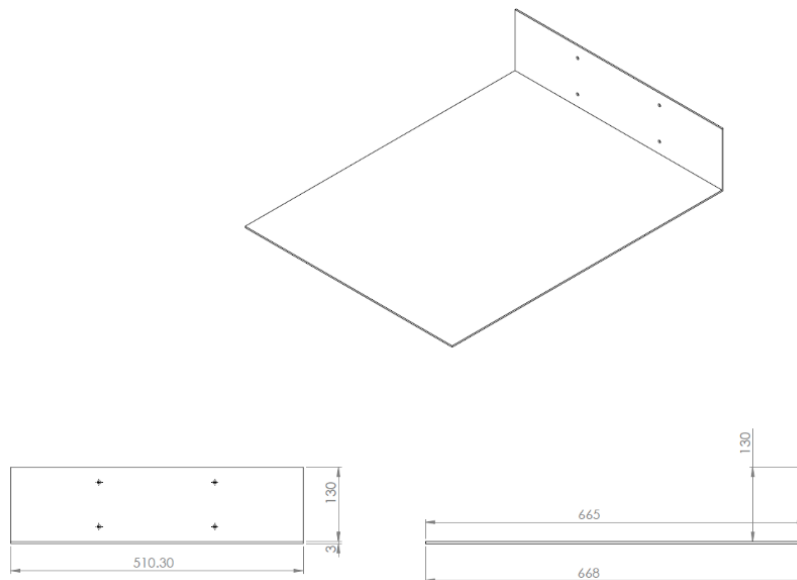


Figure 21: LAYER TWO/THREE ENCLOSURE DIMENSIONS (RAJINDA JAYAMANNA 2013)



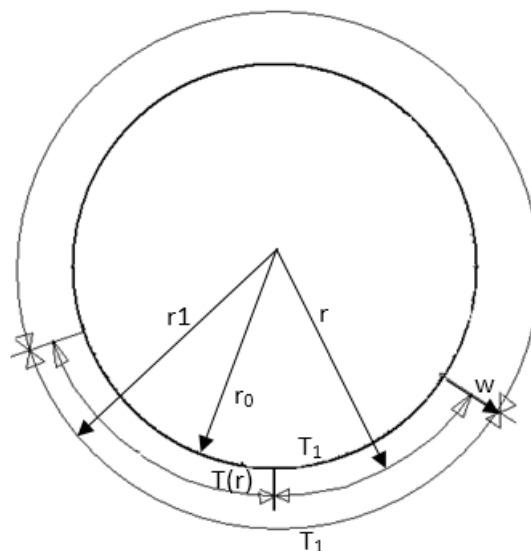
8. CONDUCTOR POWER LOSS

Based on the final “as built” revisions for the battery enclosure, battery modules were created so that a multi-tiered modular circuit could be developed. This implies the use of high voltage conductor cables to carry the nominal 96V DC between the parallel modules. As a result, selection of a suitable conductor was based on minimising radial thermal heat around the conductors due to power loss. Electrical cables are comprised of a core that is insulated with an outer protective sheath. These cable cores have an array of copper wire which constitutes 50% of the inner core. Heat conduction due to power loss through transmission occurs predominantly in the longitudinal direction of the copper conductor. Heat will also be

transferred radially through the porous copper wires by methods of thermal radiation and heat conduction throughout the length of the conductor.

Fourier's law of heat conduction dictates that the amount of heat in Btu per unit time flowing through a specific area is proportional to the area as well as the temperature gradient expressed as degrees Celsius per unit length. Using this law, a steady state model can be used to analyse the heat loss per unit time from a particular length of conductor with a radius of r_0 carrying a nominal current of 240A causing a constant insulation surface temperature of T_1 . It is under the assumption that all heat produced as a consequence of thermal radiation due to power loss will be purely radial. Therefore temperature at the layer of insulation will be dependent purely on the radial distance from the copper core conductor. Figure 23 below illustrates this assumption:

Figure 22: TYPICAL CROSS SECTION OF A CONDUCTOR (MCGRAWHILL 1999)



Under the assumption that all heat flow through the insulated layer will be passed radially, it follows that all heat shall pass into the insulation through the inner radius r_0 surface and thus eventually pass into the ambient air through the outer surface radius r_1 . Likewise the same quantity of heat Q shall be transmitted via all coaxial cylindrical areas between radius r_0 and $r_1 = r_0 + w$. Denoting T as the temperature within the insulation at radius r , we can define the temperature gradient as dT/dr per unit length in the direction perpendicular to the cylindrical area of radius r . Therefore the amount of heat Q shall be:

$$Q = \text{thermal conductivity} \times \text{area} \times \text{temperature gradient} = k (1 \times 2\pi r) \frac{dT}{dr} \quad [24]$$

Integrating equation 24 we can thereby express the equation as:

$$T = \frac{Q}{2\pi k} \ln r + c \quad [25]$$

The integration constant c can be found by the fact that $T = T_o$ when $r = r_o$ whereby:

$$c = T_o - \frac{Q}{2\pi k} \ln r_o \quad [26]$$

By substituting the equation 26 into equation 24 we obtain the following:

$$c = T_o - \frac{Q}{2\pi k} \ln r_o \quad [27]$$

8.1 STEADY STATE CONDUCTOR POWER LOSS SIMULATION

This steady state equation as computed from Fourier's law of heat transfer can be then used to model the various conductor sizes based on the above parameters. Ansys computational fluid dynamics solver was utilised in order to conduct this investigation. The program allows the user to input important variables ascertaining to the analysis such as:

- ✚ Copper conductor cross sectional area (m^2).
- ✚ Insulation thickness (w as per figure 23) and its material properties (electric conductivity, material density, heat conductivity).
- ✚ Boundary condition ; outer/inner diameter and heat coefficient h .
- ✚ User variable inputs (current, voltage, initial ambient temperature (T_1)).

Prior to creating a simulation environment, research was undertaken as to the different types of conductors available. Due to the sponsorship initiatives from Hauber and Sunher, procurement of high voltage cables was coordinated from their company. Engineering analyses were made in relation to the company's Radox155 series conductors, which comply with the wiring standards outlined by IEC228 (class 5) [18]. This ensures that maximum ohmic resistance throughout the cable length is limited to $0.80 \Omega/km$ for conductor diameters exceeding a cross sectional area of $25mm^2$. Specifications of the different conductor sizes considered under the following product range are listed below:

Figure 23: RADOX155 CONDUCTOR ASSEMBLY PROFILE

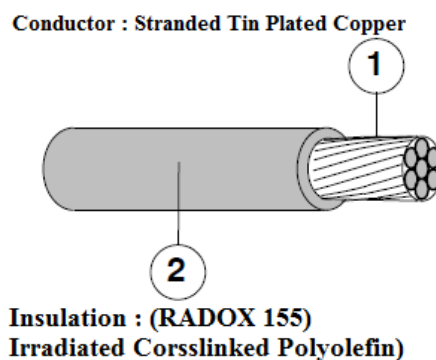


Table 9: RADOX155 DIMENSIONS AND CONDUCTOR RESISTANCE SPECIFICATIONS (HAUBER AND SUNHER 2012)

Cross section nom. mm ²	Conductor construction nom. n x mmØ	Conductor diameter max. mm	Core diameter D mm	R ₂₀ IEC 228 max. Ω / km	Weight nom. kg / 100m	Nominal voltage V	Test voltage V	Min. bending radius mm
0.25	19 x 0.13	0.6	1.45 ± 0.05	85.9	0.4	450/750	2500	3 x D
0.34	19 x 0.16	0.8	1.60 ± 0.10	52.1	0.5	450/750	2500	3 x D
0.50	19 x 0.18	0.9	1.70 ± 0.10	40.1	0.7	450/750	2500	3 x D
0.75	24 x 0.20	1.15	2.20 ± 0.10	26.7	1.1	600/1000	3500	3 x D
1.0	32 x 0.20	1.3	2.60 ± 0.10	20.0	1.5	600/1000	3500	3 x D
1.5	30 x 0.25	1.55	2.70 ± 0.10	13.7	1.9	600/1000	3500	3 x D
2.5	48 x 0.25	2.05	3.50 ± 0.10	8.21	3.0	600/1000	3500	3 x D
4.0	56 x 0.30	2.6	4.15 ± 0.15	5.09	4.5	600/1000	3500	3 x D
6.0	81 x 0.30	3.4	5.4 ± 0.15	3.39	6.5	600/1000	3500	3 x D
10	78 x 0.40	4.4	6.4 ± 0.15	1.95	11	600/1000	3500	3 x D
16	119 x 0.40	5.4	7.6 ± 0.15	1.24	16.5	600/1000	3500	3 x D
25	182 x 0.40	6.7	9.2 ± 0.2	0.795	25	600/1000	3500	3 x D
35	266 x 0.40	7.9	10.6 ± 0.2	0.565	34.5	600/1000	3500	3 x D
50	378 x 0.40	9.4	12.3 ± 0.25	0.393	50	600/1000	3500	4 x D
70	348 x 0.50	11.5	14.6 ± 0.25	0.277	68	600/1000	3500	4 x D
95	444 x 0.50	12.9	16.3 ± 0.3	0.210	89	600/1000	3500	4 x D
120	570 x 0.50	15.3	19.0 ± 0.3	0.164	110	600/1000	3500	4 x D
150	722 x 0.50	17.0	20.8 ± 0.3	0.132	142	600/1000	3500	4 x D
185	874 x 0.50	18.5	22.5 ± 0.3	0.108	171	600/1000	3500	4 x D
240	1147 x 0.50	21.3	25.7 ± 0.3	0.0817	225	600/1000	3500	4 x D

Conductor sizes enclosed within the rectangular box are the ones that were considered to be implemented into the final design. An important aspect was to ensure the conductors chosen conformed to battery box FEL design requirements which only allows for 100mm clearance. This 100mm clearance is to provide such high voltage cables with a certain degree of bending radius. Table 26 identifies that conductors with cross sectional area of 25, 50 and 70mm² allow for a minimum bending radius of 31.8, 49.2 and 58.4mm respectively. A safety factor was considered and, thus, use of a 95 mm² and above conductor cross sectional area was not considered in the engineering design proposal.

8.1.1 SIMULATION ENVIRONMENT

Simulation for the steady state thermal behaviour of these conductors was carried out by initially creating a geometric profile environment. Figure 23 shows the typical cross

sectional area of an electric conductor whereby the internal concentric circle of radius r_0 being representative of the copper conductor. The outer concentric circle (w) represents that of the insulated region. Simulation of the external environment was assumed to be at an initial ambient air temperature of 300K (26°C).

Figure 25: ANSYS SIMULATION GEOMETRY PROFILE

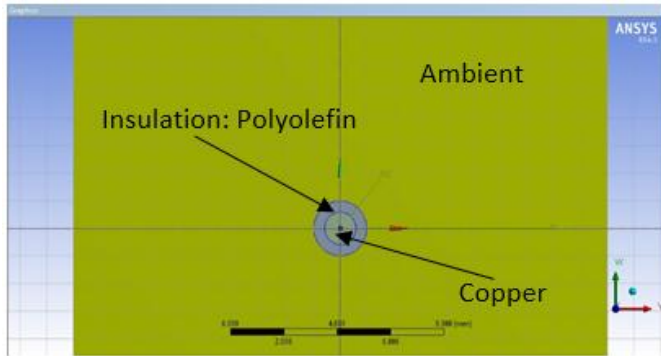
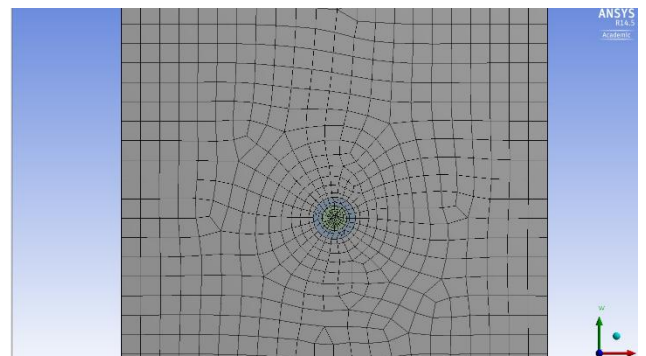


Figure 24: ANSYS GEOMETRY MESH



Once simulation geometry was developed the following model was then meshed, as per figure 28, so that material properties and input parameters could be entered for two dimensional simulation case. Each of the three simulations was conducted based on the material properties and dimensions listed in figure 26 for conductor cross sectional sizing's of 35, 50 and 70mm². Material properties for each of the boundary elements were entered as followed:

Table 10: MATERIAL PROPERTIES DATA

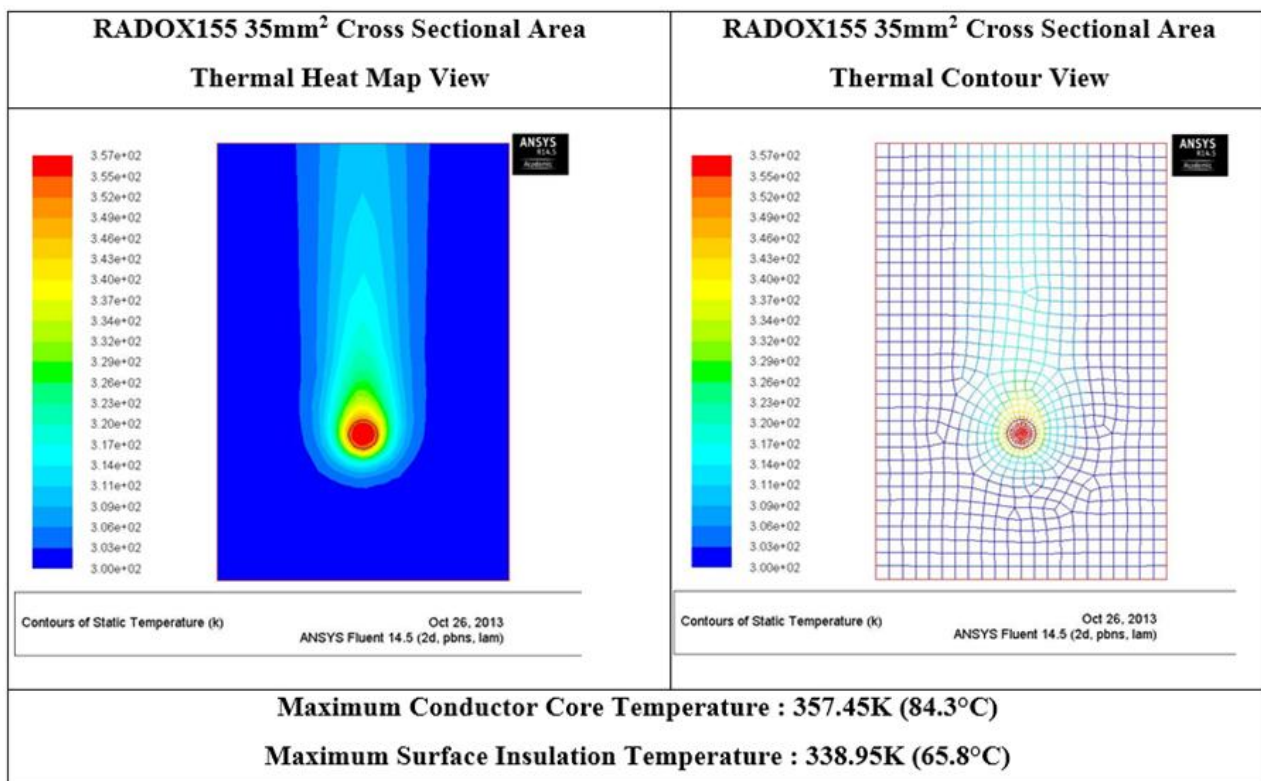
Element Wall	Material Type	Density	Specific Heat (J/Kg-K)	Thermal Conductivity (W/m-K)	Gravity	Current	Internal Emissivity	Operating Pressure (pa)	Thermal Expansion Coefficient
Air	-	1.16	1006.43	0.0242	-9.81	-	0	101325	0.0333
Polyolefin	(Alkene Polymer)	1480	1050	0.16	-9.81	-	1	101325	-
Copper	Copper Alloy	8978	381	387.6	-9.81	240A	1	101325	-

Inputs regarding geometric dimensions were altered according to conductor cross sectional area for each simulation run. To allow for accurate convergence of a steady state thermal solution, 1000 iterations were chosen for each simulation run.

Current input through the copper conductor was assumed to be 240A since this will be the continuous discharge current transmitted by the lithium iron phosphate cells. Whilst the two minute current rating is rated for 650A, this would not provide an accurate overview of conductor performance as the discharge rate from the power source would affect the long term performance of the cell. Figure 26 below shows the results obtained for each of the three conductor steady state thermal responses

8.1.2 SIMULATION RESULTS

Figure 26: HEAT MAP FOR RADOX155 35MM² CROSS SECTIONAL AREA

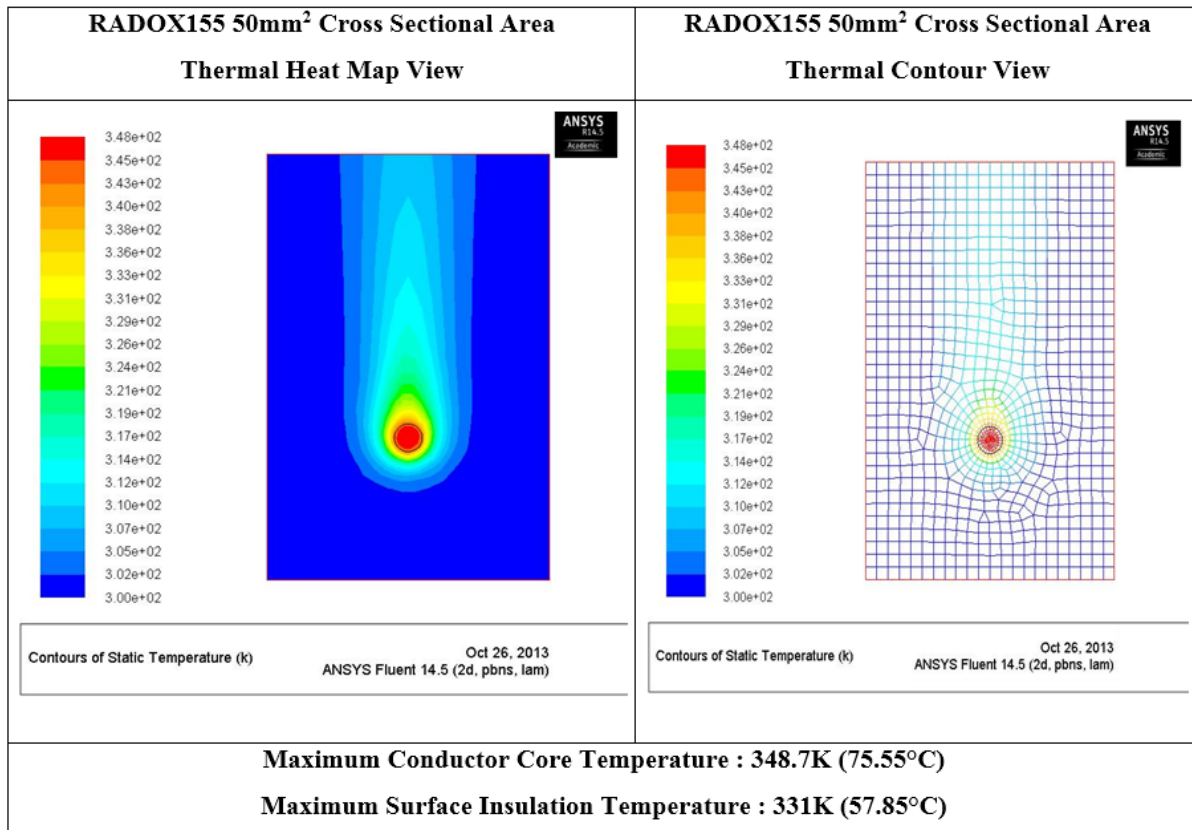


The use of 35mm² Radox155 conductor was deemed unsuitable due to its core temperature rising to a steady state value of 84.3°C. Since operating temperature for this specification of conductors are rated only for 60°C, exposing the following cable to the calculated temperature would be likely to cause insulation damage and therefore a risk of fire and damage to the watercraft. Whilst insulation outer surface r_1 will be at a temperature of approximately 65.80°C there is a potential for the following material to be damaged due to these excessive exothermic conditions. Another important consideration is the direct connection of the copper conductor to the appendant bus plate and cathode/anode terminal. With a core temperature of this calibre it would be likely that such heat would exacerbate the

effect of thermal runaway on the lithium iron phosphate battery cells. Internal temperature of enclosure without adequate cooling system would likely to cause rapid degradation of cell capacity. In turn, at such temperatures, the power source would theoretically provide minimal operational time compared to the ideal 20 minute run time calculated.

Figure 27 below provides steady state simulation results when using conductors rated at 50mm².

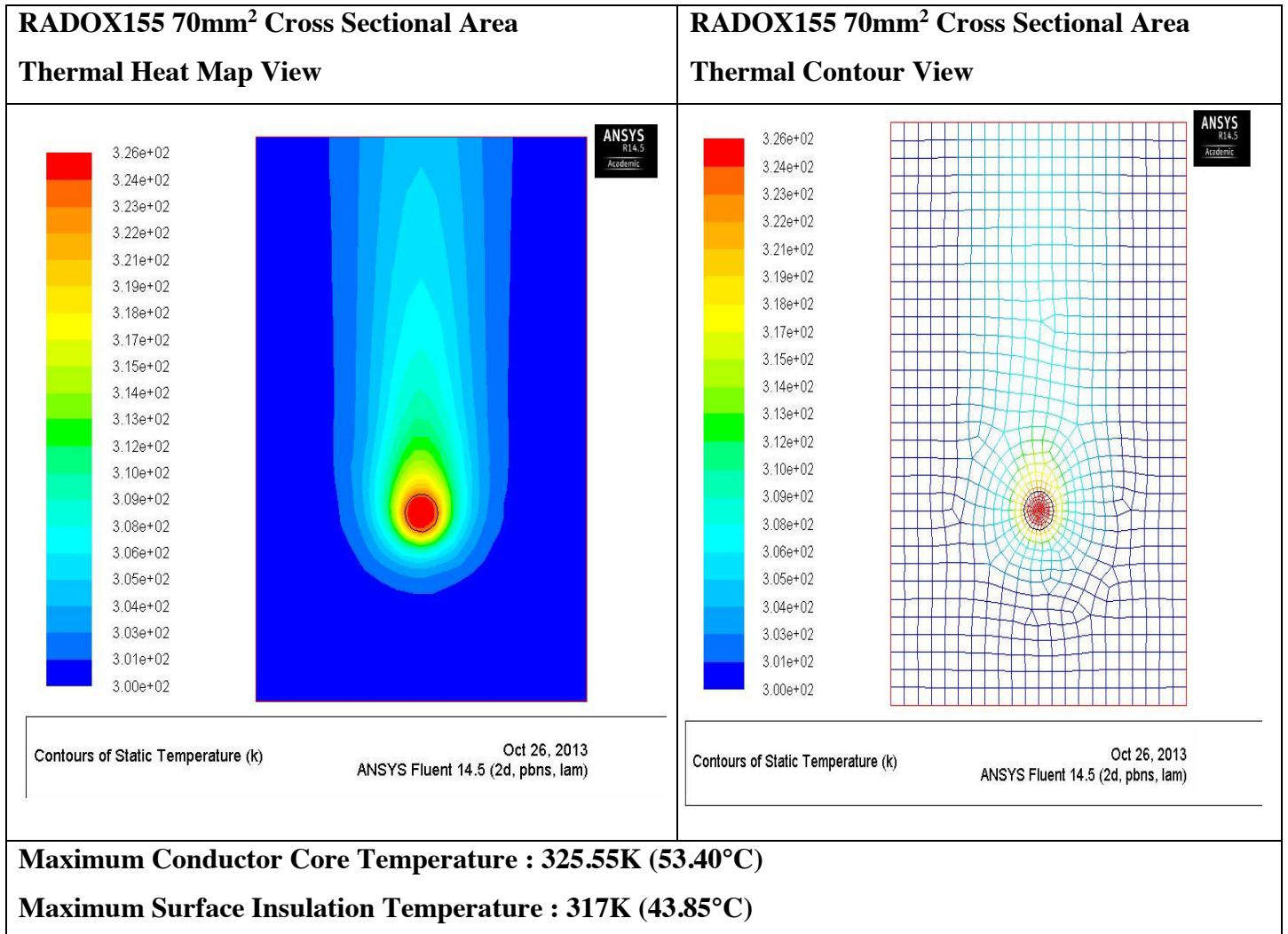
Figure 27: HEAT MAP FOR RADOX155 50MM² CROSS SECTIONAL AREA



The use of 50mm² conductor sizing indicates that a steady state temperature of 75.55°C will be reached at the core. Compared to results obtained for a 35mm² such a core temperature would be deemed unsafe and exceeds the safe operational temperature specified by the manufacturer. Additionally in this instance the use of 50mm² Radox will result in the insulation surface temperature reaching 57.85°C. When compared to the use of 35mm² it is evident that such surface temperatures are controllable and within the safe operational temperatures for both the enclosure and lithium iron cells. However, the copper conductor will be in direct contact with both the bus bar plate and anode/cathode terminal which can be detrimental to the cell due to its high core temperature at 75.55°C. For these reasons, use of 50mm² conductor was foregone.

Figure 28 below displays the results obtained for conductor sizing at 70mm².

Figure 28: HEAT MAP FOR RADOX155 70MM² CROSS SECTIONAL AREA

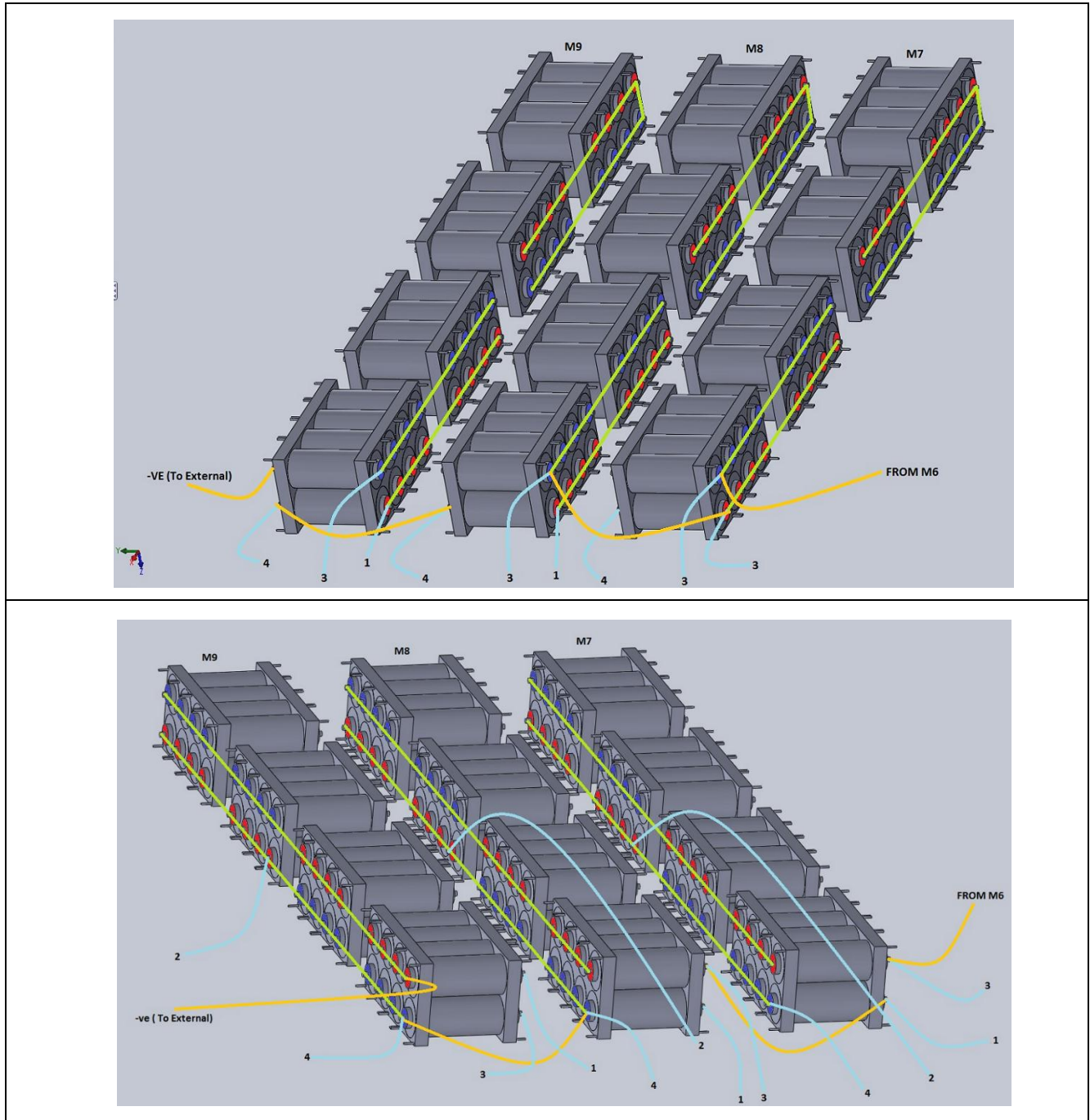


With reference to figure 28, safe operational temperatures for high voltage conductors are achieved with the use of 70mm² cross sectional area cables. Continuous transmission of 240A through such a cable size will result in a core conductor temperature of approximately 53.4°C and an external insulation surface temperature of 43.85°C. As shown by specification sheet from Hauber and Sunher for Radox155 these temperature values comply with the safe operating temperature of this particular cable at a nominal current rating of 240A continuous. Thermal maps also indicate that ambient air temperature within the enclosure will increase to 31.85°C (with initial ambient conditions at 25°C). Whilst an adequate cooling system will have to be implemented to minimise the effects of thermal runaway, this specification and dimension of conductor was deemed the most suitable cable under engineering requirements and safety considerations.

9. PROPOSED CIRCUIT CONSTRUCTION

Once specification requirements pertaining to the battery modules were finalised, a proposed circuit incorporating modularised battery sources was developed. Figures 29 to 31 display each of the battery module configurations for each of the layers as shown below.

Figure 29: MODULE CONFIGURATION LATER ONE - AS BUILT REVISION



As can be seen from the above figure, green links represent the connections between each module through the use of specified copper bus bars. Each blue and red filling represents the

cell's anode and cathode terminals. In order to connect parallel modules, high voltage 75mm² (total cable cross sectional area) cables rated for 96V DC were used as per design criteria specified in the scope section 3.3. Circuit protection at each level was undertaken by the use of BMM modules, with blue wires numbered 1-4 representing low voltage cables at each monitoring node in the circuit as per figure 13. For layer one a total of 12 BMS wires were used due to the implementation of twelve individual modules within the following level. Each non latching battery management module monitors the individual parallel modules M7, M8 and M9.

Figure 30: MODULE CONFIGURATION LAYER 2 - AS BUILT REVISION

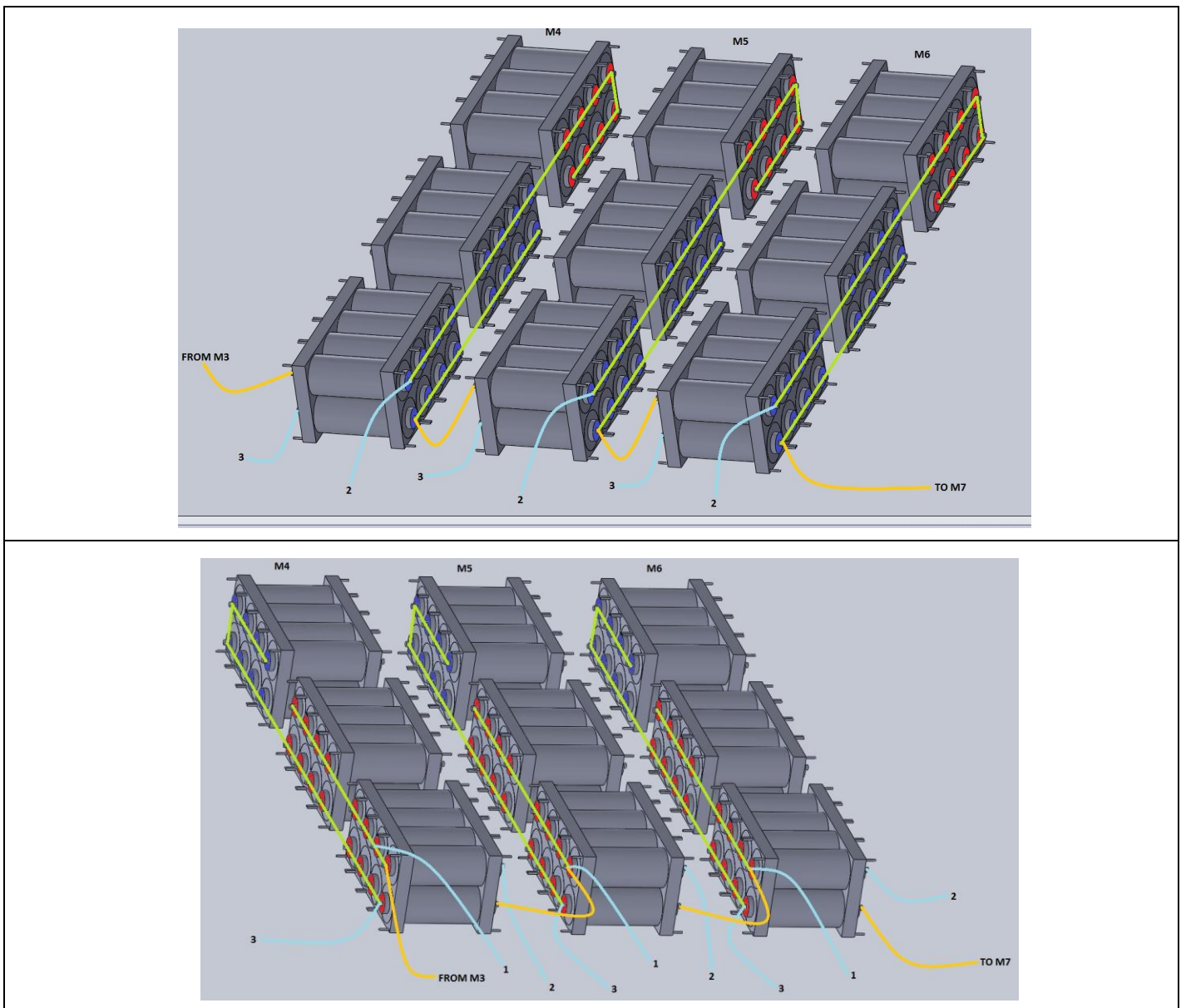
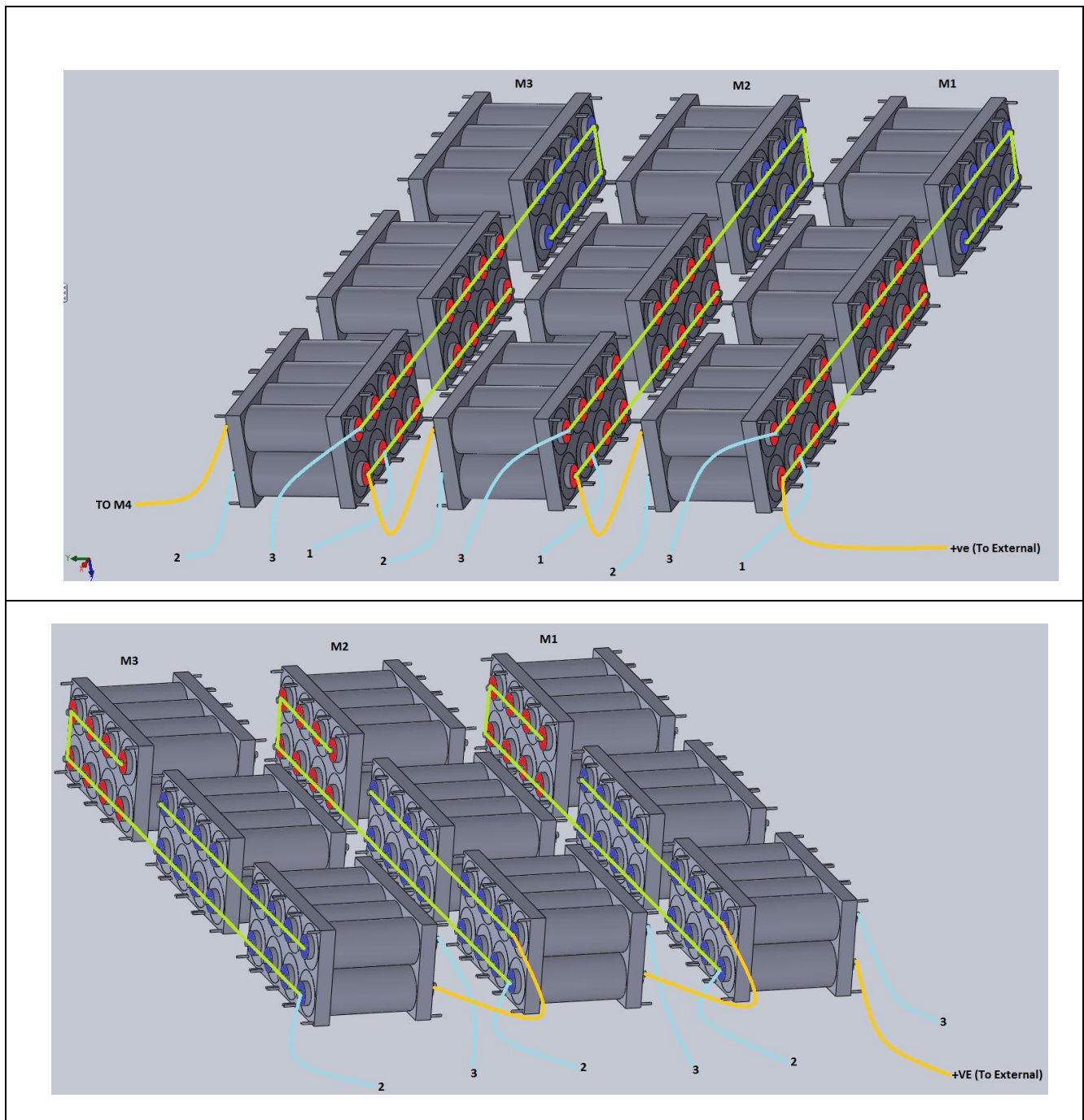


Figure 31: MODULE CONFIGURATION LAYER 3 - AS BUILT REVISION



Layer three and two will have a total of 9 individual modules in each layer. Layer 3 will carry the high voltage positive side conductor to the motor controller whereas layer one will carry the negative side of the high voltage conductor to the motor controller. Between the output high voltage conductors circuit protection will be incorporated to minimise possible fire hazard and injury in the event of cell module fault or sparking. This is to be carried out by the use of an in-line contactor which will be placed in layer 2.

10. BATTERY MODULE WIRING

These monitoring modules are to have an under voltage threshold of 2.0V dc and over voltage threshold of less than 4.0V to ensure safe operation of the individual cells. Connections to the battery monitoring modules are to be carried out through the use of low current shielded data cables. These cables are ideal for the application since each data cable consists of 4 internal conductors rated for a low current at 1.5A with an operating temperature of 60°C. Specifications of monitoring module conductors are as follows:

Conductor Profile :	
	
Size	7/0.20
Number of Conductors	4
Strand Diameter	0.20mm
Outer Shielding Diameter	4.6mm
Conductor Area	0.22mm ²
Operating Temperature	60°C

Due to the colour coded nature of the individual conductors, each battery cell monitoring node numbered 1 through to 4 as shown in figure 25 will be assigned a colour for ease of reference. Node numbers 1, 2, 3, and 4 shall be assigned Red, Green, White and Black respectively to ensure proper connections to the monitoring modules.

11. ELECTROCHEMICAL CELL MODELLING

An integral part of any electric or hybrid vehicle is the power source as it dictates the overall performance of the car. Therefore one important aspect is the modelling of the electrochemical cell's transient behaviour under normal operation. Several models have been used by industry to gain insight into the thermal behaviour of battery cells due to the electrochemistry. These models include zero-dimension resistor capacitor circuit, multi-dimension potential-current distribution and detailed electrochemistry modelling with consideration of internal separator layers. For this particular case, utilisation of Ansys Fluent Add-on-Battery modeller has provided some insight into thermal effects such as runaway and exothermic reactions within the cell substrate due to normal operation. It is vital to gain foresight into how the cell behaves under normal loads so that issues pertaining to excessive

heating can be addressed prior to construction and production phase of the project. Ansys Fluent has adopted the Tiedemann and Newman 1 dimensional model to analyse such behaviours. This original 1 dimensional model has been modified to formulate 3 dimensional computations based on the original model. The Newman and Tiedemann models aims to analyse the transient behaviour of electrochemical cells attributed to the electrolyte diffusion process within the porous electrodes [19]. Computation of the diffusion process by this model only considers the anode/cathode electrode and their current collectors. Between the anode and cathode terminal exists the separator which is modelled as an infinitely thin interface between these two terminals whereby a potential jump due to loss exists [19].

11.1 MATHEMATICAL DERIVATION

Ansys requires the user to create a three dimensional geometry with the fundamental wall parameters including anode, cathode and separator. Newman Tiedemann's mathematical derivation for the diffusion process is as follows:

$$\int_V \nabla \cdot (\sigma \nabla \varphi) dV = \int_A j dA \quad [29]$$

Equation 29 expresses the electric potential equation by an integral which equals the total current density in a given area. The alphanumeric value j represents the current density at the anode/cathode where the separator interface exists. The surface area given by A is the area of this interface and σ is the electrical conductivity at the separator wall. Newman and Tiedemann were later able to correlate the linear relationship between current density j (A/m^2) and the cell voltage governed by the following mathematical equation:

$$j = Y (\varphi_c - \varphi_a - U) \quad [30]$$

Equation 30 indicates that the cell voltage is given by the difference between anode and cathode electric potential nearest to the separator interface given by $(\varphi_c - \varphi_a)$ [19]. The total equilibrium voltage U (V) of the battery cell can be found by the intercept of a typical voltage current curve for a specific battery cell where current would be equal to zero [19]. Similarly, Y , apparent current density ($1/\Omega m^2$) can be found by the inverse slope of the same voltage current curve. Moreover such findings by Newman and Tiedemann indicated that these two variables Y and U are related to the depth of discharge (DOD) relative to the nominal capacity of the battery (Qt). Governing equations for the two relationships are:

$$U = a_0 + a_1 \cdot DOD + a_2 \cdot DOD^2 + a_3 DOD^4 + a_4 DOD^4 + a_5 DOD^5 \quad [31]$$

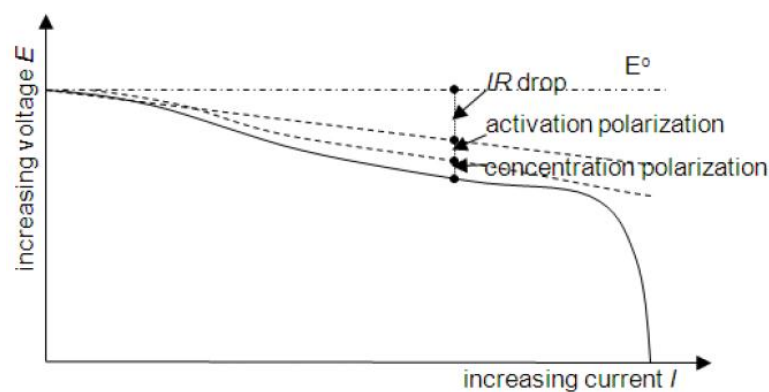
$$Y = b_0 + b_1 \cdot DOD + b_2 \cdot DOD^2 + b_3 DOD^4 + b_4 DOD^4 + b_5 DOD^5 \quad [32]$$

Coefficient represented as a_i and b_i for $i = 0:5$ are constants which can be found through the use of a polarization curve provided by the manufacturer of the battery. Values for the specific depth of discharge points can be easily obtained through the following equation:

$$DOD = \frac{A}{Q_t} \int_0^t j dt \quad [33]$$

In order to find the constants a_i and b_i for $i = 0:5$, a discharge profile of the battery cell can be used. A typical polarization curve given below highlights the different energy losses involved.

Figure 32: TYPICAL POLARIZATION CURVE (GOEBEL ET AL 2009)



The IR drop can be represented as ΔE_{mt} which is the voltage drop caused by both the internal resistance of the battery and mass transfer caused by ion diffusion [20]. Activation polarization (ΔE_{sd}) is represented by the energy drop due to the self-discharge of the cell [20]. Finally, the concentration polarization can be represented as ΔE_{rd} which is the potential drop caused by cell reactant depletion (concentration gradient of ions from the anode/cathode) [20]. All such polarization losses are governed by the following equations where:

$$\Delta E_{mt}(t) = \Delta E_{init} - a_5 t \quad [35]$$

$$\Delta E_{rd}(t) = a_3 e^{(a_4 t)} \quad [36]$$

$$\Delta E_{sd}(t) = a_1 e^{\left(-\frac{a_2}{t}\right)} \quad [37]$$

The initial voltage drop denoted ΔE_{init} is primarily due to the initial current flow through the cell. The initial internal resistance causes a potential difference (internally) between anode/cathode terminals. Constant b_i and *for* $i = 0:5$ can be found in the same way through the use of a current density vs. time polarization curve which would allow the user to utilise the same governing equations for the energy losses in equations 35 to 37.

Whilst equations 30 to 33 aim to provide insight into the electrochemical behaviour due to current density distribution and electric potential at the separator interface, Newman's model can be further extrapolated to describe thermal behaviour from thermal coupling and electric field potential. Electric conductivity can be described through its dependent nature on the internal temperature of the cell where $\sigma = \sigma(T)$. By rearranging equation 32, current density can be modelled through a temperature dependent mathematical model governed by:

$$Y = \left(\sum_{n=0}^5 b_n (DOD)^n \right) e^{C_1 \left(\frac{1}{T_{ref}} - \frac{1}{T} \right)} \quad [34]$$

Likewise, the relationship between equilibrium voltage and temperature can be found by the following equation:

$$U = \left(\sum_{n=0}^5 a_n (DOD)^n \right) - C_2 (T - T_{ref}) \quad [34]$$

Where T_{ref} represents the reference temperature of the voltage current curve for which the constants a_i and b_i are found.

Joule heating caused by diffusion of electrolytes within the cell can be represented by:

$$S_{joule} = \frac{i^2}{\sigma} = \frac{\sigma^2 \nabla^2 \phi}{\sigma} = \sigma \nabla^2 \phi \quad [35]$$

Besides joule heating due to electrolyte diffusion between separator boundary walls, another source of heat is due to reaction heating between the chemicals within the cell:

$$S_{chem} = j \cdot [U - (\phi_c - \phi_a)] \frac{A}{Vol}$$

Where Vol denotes the total volume of the battery cell.

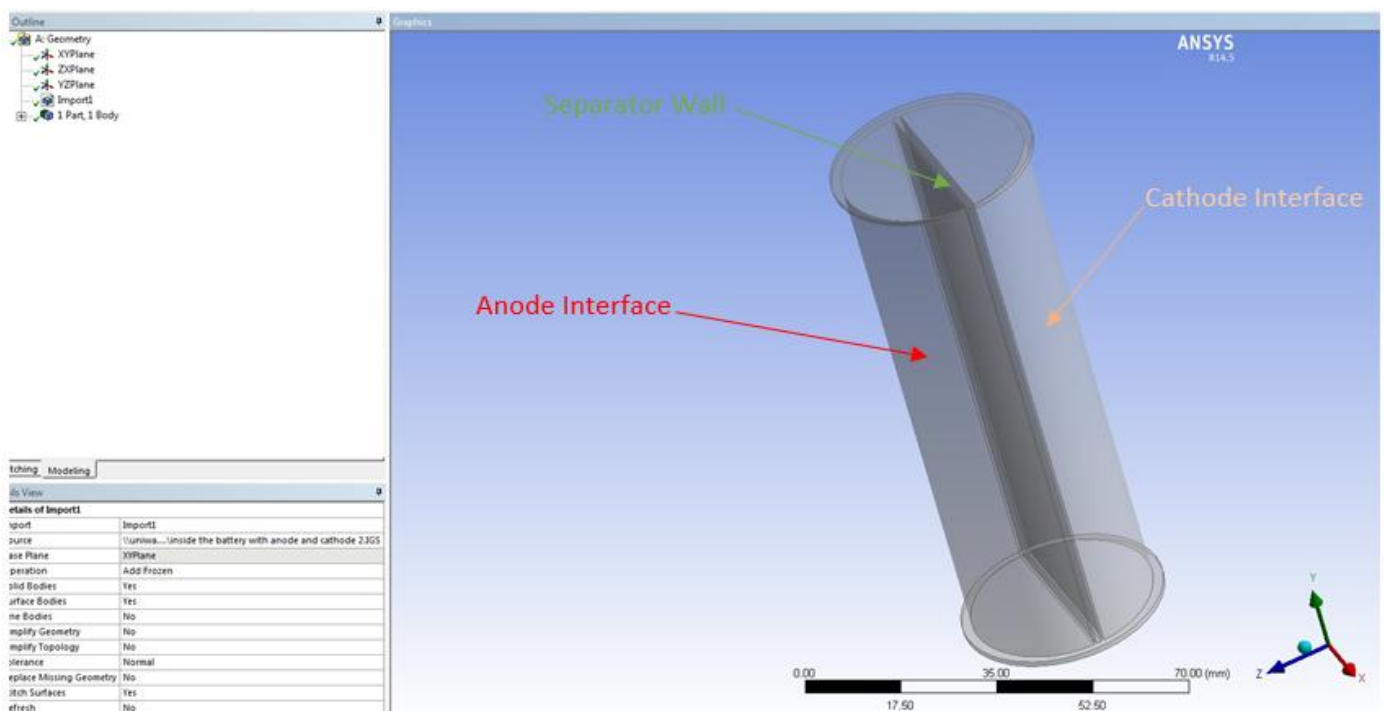
11.2 USING ANSYS FLUENT TO MODEL ELECTROCHEMICAL BEHAVIOR (SINGLE CELL)

Creation of an appropriate geometry is crucial for the accuracy of data obtained through such an analysis. Ansys fluent battery add-on module requires the user to create each geometry with the following wall/parameter regions present:

-  Anode Terminal.
-  Cathode Terminal.
-  Separator (infinitely thin surface wall).

Figure 33 below depicts the Headway 38120S LiFePO₄ that is to be analysed as per design analysis requirements.

Figure 33: HEADWAY 38120S GEOMETRY PROFILE



Once geometry interfaces were defined, parameters regarding cell performance characteristics and attributes were placed into the user interface. As per cell specification sheet in section 5 table 5 the following input variables were entered into the battery models parameter tab:

Table 11: SIMULATION/MODEL ENVIRONMENT PARAMETERS

Electrochemistry Source			Lithium Iron Phosphate
Type			
Discharge Rate		3C (30A)	
Nominal Capacity (ah)		10,000mAh	
System Current (A)		240A (Continuous discharge)	
Current Under Relaxation		160A (2C Steady State discharge per cell)	
Internal Resistance		6mΩ (per cell)	
Separator	Current	2255	
Density			
Cell Volume		138362.02mm ³	
Separator	Wall	Area	2040 mm ²
(mm ²)			

Activation parameter coefficients a_0 to a_5 and b_0 to b_5 were unable to be acquired by the manufacturer due to the lack of testing carried out on the cells. Therefore similar lithium iron phosphate cell information was located and these constants were used for the purpose of this simulation. Coefficients used as the activation parameters are sourced from another lithium iron phosphate battery cell which had a nominal voltage of 3.2V and a nominal capacity of 10,000mAh. The only minor difference was the internal resistance which in this case was 8mΩ. Therefore, the activation parameters used are as listed below:

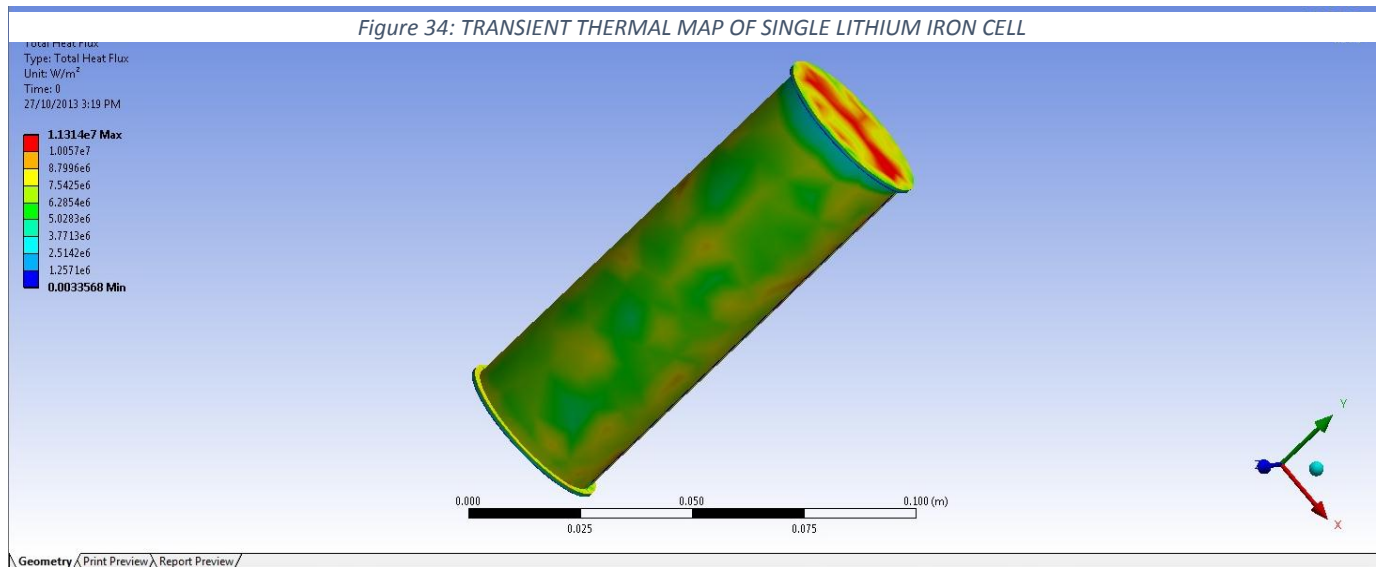
a_0	a_1	a_2	a_3	a_4	a_5
4.1	3.2	-1.25	-1.05	0	0

b_0	b_1	b_2	b_3	b_4	b_5
2100	43122	-7811	0	0	0

As recommended by Ansys, all electrochemical 3 dimensional simulations should utilise double precision in its computational process. The use of double precision computations allows the user to obtain a more highly refined and accurate model at the cost of computational time. For a single cell simulation the equipment used was an Intel Core 2 Duo (Quad Core at 2.7Ghz) with 4096 Megabytes of Ram.

11.2.1 RESULTS OBTAINED FROM ANSYS FLUENT (SINGLE CELL)

Figure 28 below provides thermal heat map results obtained from the following computation:



Results obtained from figure 34, shows the exothermic heat produced due to the electrochemical behaviour of the cell. The thermal heat map is the result of the load conditions specified in table 11. Under such conditions almost 75% of the outer encasing of the cell will reach a temperature of approximately 45.70°C with the anode and cathode terminals reaching a maximum of almost 57.13°C. This is expected since concentration of electrolyte ions are the greatest at the terminals and hence the diffusion process in these areas are greatest.

Exothermic heat production is strongly correlated with the concentration of electrolyte ions. This means that a higher area of concentration will produce larger diffusion of ions between the separator interface and the region with large concentrations. This in turn is why it is expected that the anode/cathode with its high concentration gradient, will produce the largest amount of heat in these respective regions. The simulation shows that maximum temperature reached (57.13°C) is less than the maximum operational temperature of the cell (60°C) as per the specification sheet in table 5.

11.3 USING ANSYS FLUENT TO MODEL ELECTROCHEMICAL BEHAVIOR (ENTIRE MODULE LAYER)

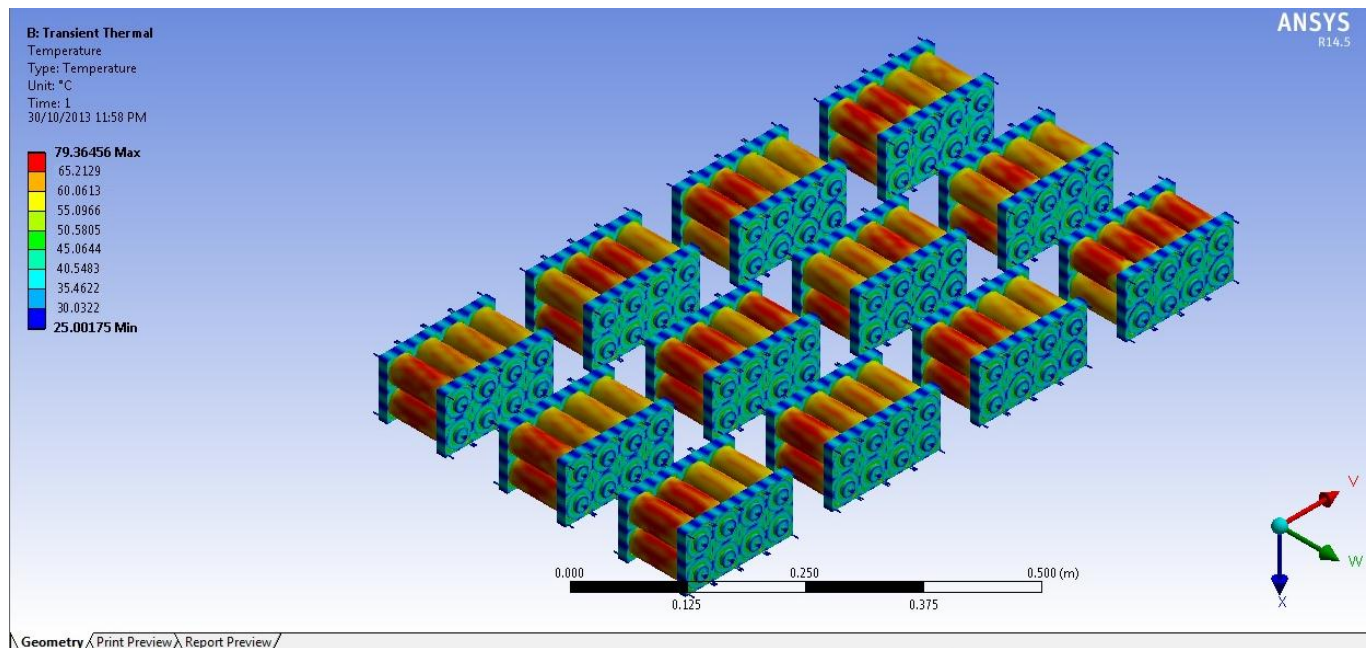
An important consideration is that the simulation has ignored the true ambient conditions that this cell will actually be exposed to. Transient thermal simulation has been conducted assuming an initial ambient temperature of 25°C, which would be unrealistic as multiple modules within a single battery layer would likely to increase the temperature even further. Therefore a more robust and realistic simulation must be conducted to achieve true data.

An additional simulation was conducted on a single layer with the entire battery module layer being a part of the simulation environment. Conducting such a task proved extremely difficult due to the limitation of hardware processing power for such a complex profile. Ansys Fluent can only be run using the university computers, as a private license would involve exorbitant amounts of money to obtain. To minimise computational processing time for a module layer, the mesh size was enlarged to reduce the number of iterations carried out on the geometry. By enlarging the mesh size the number of elements on the model become considerably less and therefore less iterations are required. However this does come at the cost of reduced accuracy in the data obtained.

11.3.1 RESULTS OBTAINED FROM ANSYS FLUENT (ENTIRE MODULE LAYER)

Simulation of a single layer was undertaken in a similar process to the single cell simulation. However mesh size was drastically reduced to allow for results to be obtained in a manageable time period. Furthermore steady state ambient temperature was considered to be the temperature at which the cell encasings reach as a result of the electrochemistry. For simplicity the plastic battery brackets were not incorporated into the simulation as this would not have any drastic impact on the final thermal conditions. Thermal map of the single layered modules are displayed below;

Figure 35: THERMAL MAP OF SINGLE LAYERED MODULES



The Heat map show that with exothermic heat production from neighbouring modules, a maximum cell surface temperature of 79.36°C is reached. Please note that battery brackets have not been considered in the following simulation and hence why they remain at a temperature of 25°C. While only a small percentage of the cells reach a maximum value, there seems to be other cells that are within the recommended operating temperature of 60°C. However it is important to note that such high temperatures will be damaging not only to the cells chemistry but can jeopardise the overall safety of the watercraft. In this simulation the integration of a cooling system has not been considered. However results suggest that an effective method for heat dissipation will be required if the power source is to be efficient and safe in its operations.

11.4 MODULE HEAT DISSIPATION

Currently there is no adequate cooling for the battery enclosure due to space confinements within each layer. Air cooling will not be suitable for this application since the internal cavity of the watercraft is fully enclosed to retain its ingress protection rating of IP65. There have been numerous proposals to incorporate a large heat sink to the bottom of the battery box which would have water pumped through the cooling coil. However as per figure 11 this water pump shall be utilised to cool the AC Induction Motor Controller.

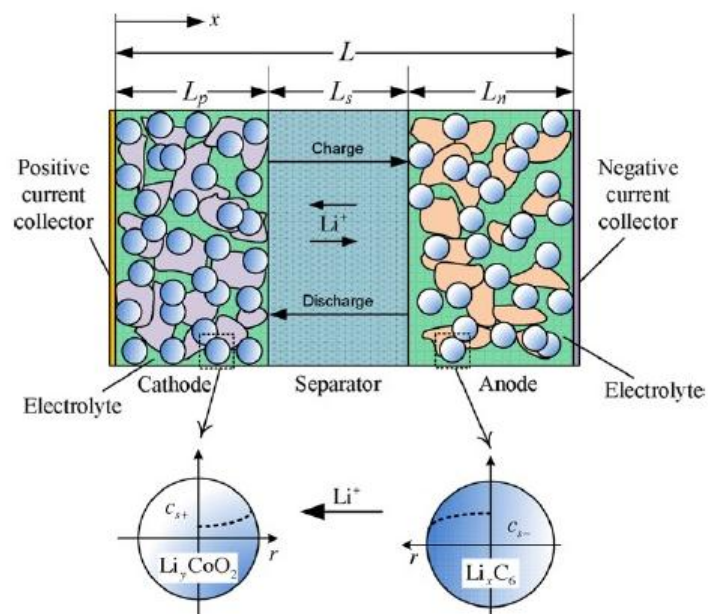
The water pump is not rated at a high enough power capacity to transfer water through to the cooling element of the motor controller and battery enclosure. In the upcoming weeks the

mechanical REV Jetski team are to conduct studies into how heat can be dissipated from the battery enclosure to allow for optimal operating thermal conditions of all cells.

12. CHARGE CONCENTRATION MODELLING

Another performance parameter that can be modelled is that of concentration gradients within the lithium ion cell. Various models have been adopted, however Ansys Simplorer adopts the Newman and Tiedemann/Doyle Et al porous electrode concentration solution [19]. The model aims to mathematically describe the charge and discharge ion transport in the solid and electrolyte solution using a one dimensional model. The one dimensional model uses the three main elements of a typical lithium ion cell as shown below;

Figure 36: TYPICAL LITHIUM IRON CELL STRUCTURE (DOYLE ET AL 1993)



The negative current collector represents the negative electrode (cathode) of the cell, the positive current collector is the anode of the battery and the separator as explained earlier is an infinitely thin interface which separates the ion charges between anode and cathode walls. The cathode region of the cell comprises of graphite (Li_xC_6) [19]. On the other hand the anode region comprises of a variety of chemistries with the majority being metal oxide. When the cell is being discharged lithium ions will diffuse to the region of graphite active particles within the negative electrode where electrochemical reactions will cause a change of state into an electrolyte solution. The ions then become positively charged and will move through this electrolytic solution through a diffusion process to the anode where they will

react with the metal oxide. Likewise for the charging of a lithium ion cell a similar process takes place however the lithium ions will move in the opposite direction from anode to cathode. Such a process is defined as intercalation and studies by Newman and Tiedemann have shown this process to be directly linked to temperature [19]. Mathematical derivation of this model can be carried out according to Fick's law of diffusion. The concentration of lithium ions in an active material to be equal to;

$$\frac{\delta C_{s,k}(x, r, t)}{\delta t} = \frac{D_{s,k}}{r^2} \times \frac{\delta}{\delta r} \left(r^2 \frac{\delta C_{s,k}(x, r, t)}{\delta r} \right) \quad [22]$$

With initial conditions:

$$-D_{s,k} \frac{\delta C_{s,k}}{\delta r} \Big|_{r=0} = 0 \quad [23]$$

$$-D_{s,k} \frac{\delta C_{s,k}}{\delta r} \Big|_{r=R_{s,k}} = J_k(x, t) \quad [24]$$

$$C_{s,k}(x, r, 0) = C_{s,k,0} \quad [25]$$

These governing equations can then be used to mathematical model the concentration gradient of diffused lithium ions by the following equation;

$$\epsilon_k \frac{\delta c_{e,k}(x, t)}{\delta t} = \frac{\delta}{\delta x} \left(D_{eff,k} \frac{\delta c_{e,k}(x, t)}{\delta x} \right) + a_k(1 - t_+) \times J_k(x, t) \quad [26]$$

For equation [26] it is assumed k=p for the anode electrode, s-k for the separator and k=n for the cathode electrode. Since electric flux produced is proportional to the concentration gradient at the positive/negative current collector the following boundary conditions can be established;

$$-D_{eff,p} \frac{\delta C_{e,p}}{\delta x} \Big|_{x=0} = -D_{eff,n} \frac{\delta C_{e,n}}{\delta x} \Big|_{x=L} \quad [27]$$

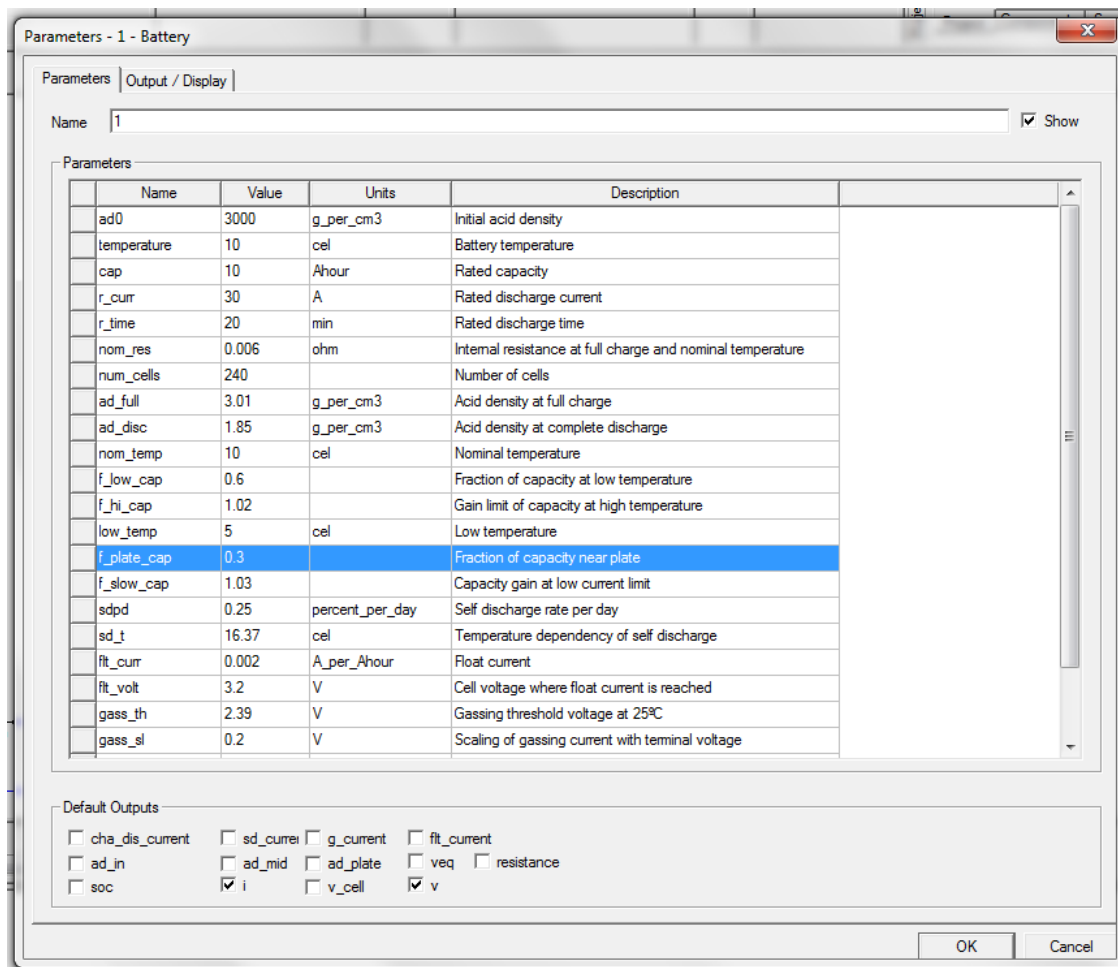
Finally by combining Kirchoff's current law and ohms law under the given boundary conditions concentration gradient as a function of temperature can be modelled as ;

$$I = -\sigma_{eff,k} \frac{\delta \varphi_{s,k}(x, t)}{\delta x} - k_{eff,k} \frac{\delta \varphi_{e,k}(x, t)}{\delta x} + \frac{2k_{eff,k}(x, t)RT}{F} (1 - t_+) \frac{\delta \ln c_{e,k}}{\delta x} \quad [28]$$

12.1 CHARGE CONCENTRATION SIMULATION

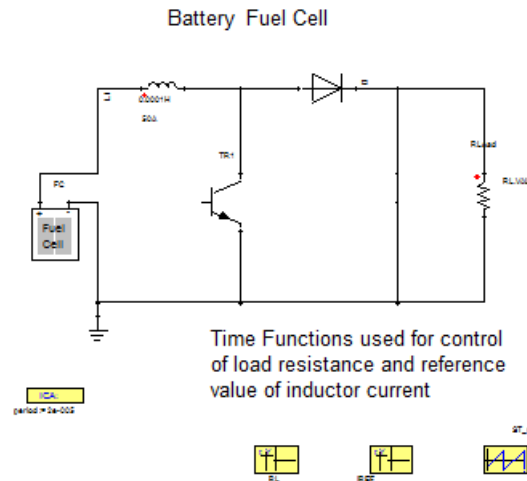
Ansys Simplorer uses these governing equations to model an accurate one dimensional model of a cells concentration gradient with respect to the applied heat load. Conducting a simulation of this nature will allow the user to obtain insight as to the optimal temperature at which the cells should be maintained. Creation of the simulation environment is very minimal with only cell parameters needed to be placed into the relevant study data. For this particular case input variables used for the simulation are shown below in the UI;

Figure 37: SIMPLORER SIMULATION VARIABLES



The circuit used to model this simulation represented cells at a normal load with all 240 cells and a total nominal voltage at 96V DC. As shown in the figure below the fuel cell was assumed to be a lumped model of the entire 30 individual modules. Furthermore resistances and inductive loads were added to simulate the entire circuit as if it was in normal operation. For simplicity the separator interface is assumed to be located at midpoint of the Headway lithium iron cell (i.e. half the total length of the battery)

Figure 38: EQUIVALENT CIRCUIT MODEL



12.1.1 SIMULATION RESULTS

Several simulations were conducted with each one being undertaken with varying temperature loads. For this project temperatures loads of; 10°C, 30°C, 50°C and 60°C were found to be the most relevant. Once the simulation on the lithium ion cell was run results obtained are shown below;

Figure 39: CHARGE CONCENTRATION VS DISTANCE FROM POSITIVE ELECTRODE

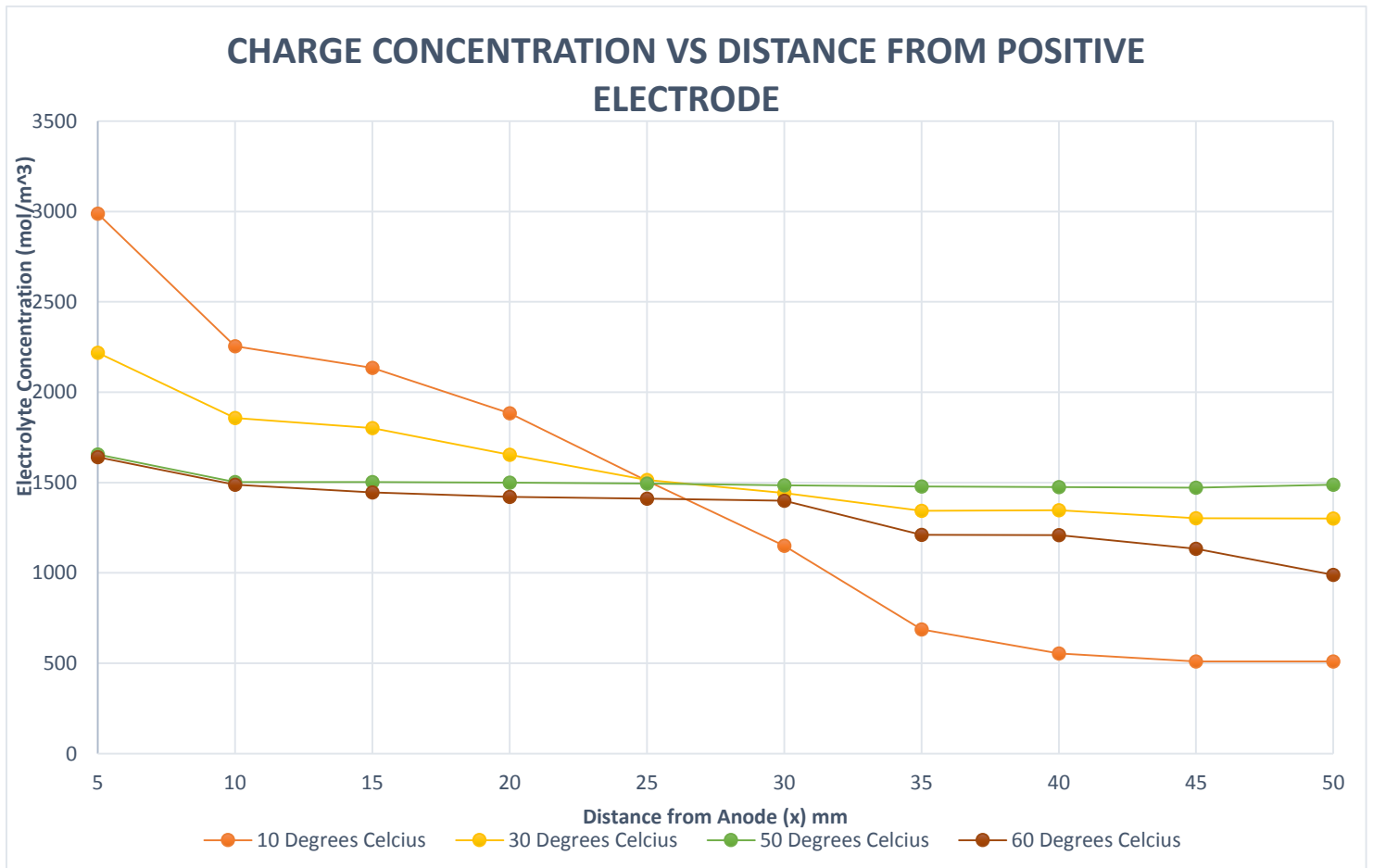


Table 12: CHARGE CONCENTRATION TABULATED DATA

Distance from Anode x (mm)	Temperature Load (10°C)	Temperature Load (30°C)	Temperature Load (50°C)	Temperature Load (60°C)
5	2988	2219	1655	1641
10	2254	1857	1503	1488
15	2134	1802	1502	1445
20	1884	1653	1500	1421
25	1509	1515	1495	1411
30	1150	1442	1485	1399
35	687	1344	1478	1211
40	554	1347	1475	1209
45	510	1302	1472	1133
50	510	1301	1488	989

Observation of the above results indicate that at lower temperatures the lithium ion cell have a much higher concentration gradient causing a rapid decrease in the diffusion process along the axial distance (x) of anode terminal. At the interface wall, which is approximately 50mm from the anode terminal it is clear that there is very minimal concentration of ions. This implies the cells inability to affectively transport lithium ions through the electrolyte solution across the interface separator effectively. Energy discharged is lower due to diminished cell concentration within the majority of the anode to interface region. On the other hand an increase in the temperature load shows a much lower gradient in the concentration profile suggesting an even spread of lithium ions throughout the anode to separator region.

A more even concentration profile throughout the cell would allow increased mobility of ions throughout the lattice and hence aid in efficient energy discharge. According to studies conducted by Doyle Et Al, lower temperatures cause an increase in the internal resistance because of lower concentration of ions available for transport through the interface and to the anode [21]. An increase in the internal resistance of the cell ultimately leads to diminished cell capacity. Increases in the load temperature also proves that chemical metabolism will increase due to ions having greater mobility as a result of greater kinetic energy [21]. Whilst results obtained show that increased temperature improves cell concentration and thus cell

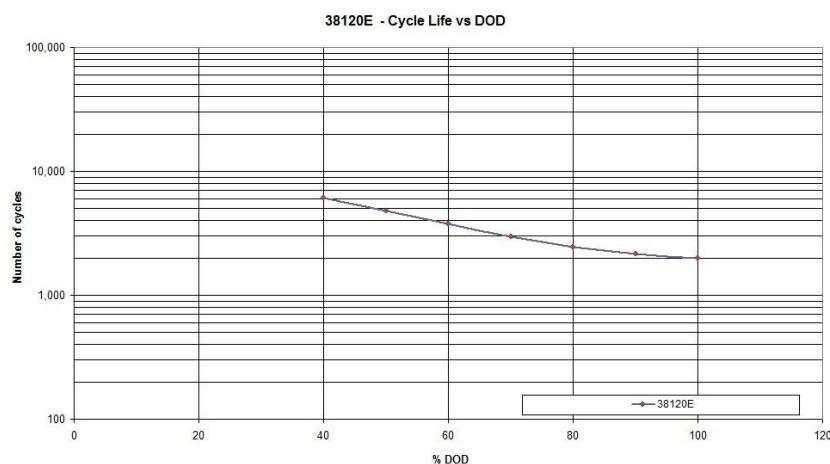
capacity, above 50°C there is a decline in performance gains. Cell concentration at the interface wall has decreased from 1488 mol/m³ to just 989 mol/m³. It therefore provides conclusive data that for optimal discharge cell capacity, the temperature of all modules must be maintained around 50°C.

13. BATTERY MANAGEMENT SYSTEM DESIGN

The use of LiFePO₄ battery technology warrants the use of adequate circuit protection, not only to ensure the cell's long term performance, but also to prevent physical injury to the watercraft and user. Prior literature has indicated the cell's high volatility to overcharging and excessive exposure to heat and thermal runaway. Furthermore, with the aim of conforming to AS300 and SAE SAE J1797, a battery management system shall be incorporated into the overall circuit of the power source. With respect to figure 15 (circuit overview) each module at every node shall be monitored in order to minimise the following factors that the cell may be affected by during its operational life:

- ✚ Unbalanced charge/discharging cycles – This occurs when modules become unevenly discharged therefore eventuating to unsymmetrical cycle lives.
- ✚ Overvoltage – If the cells are overcharged this can not only significantly degrade the overall nominal capacity and discharge profile of the cell but can also lead to possible fire hazard and toxic emission of internal chemicals.
- ✚ Under voltage – Figure 28 below shows the cycle life of the Headway LiFePO₄ in comparison to the DOD% that the cell is discharged to. There is clearly a negative correlation between these two variables and, hence, the continual discharge of the cell beyond the under voltage value of 2.0V (80% DOD) will reduce the number of cycles the cell can undergo.

Figure 40: HEADWAY LIFEPO4 CYCLE LIFE VS DOD (HEADWAY HEADQUARTERS 2013)



- ✚ Short Circuit Protection – In the event that unintentional contact is made between bus plates or any energised part of the circuit, there needs to be immediate voltage cut-off to minimise the possibility of electrocution or sparking. This is also in compliance with the AS3000 wiring standards.
- ✚ Current Limiting – Whilst the power source is able to provide a maximum peak discharge current of 800A, the management system needs to prevent such current being transmitted to the attached motor controller. However, a secondary form of current limitation is implemented through the CanBus interface of the AC-DC motor controller. The CanBus user interface allows the user to programme important parameters by VCL, such as input current/voltage and driver controls.
- ✚ Temperature Sensing – An integral part of any circuit protection system for EVs/HEVs is the mitigation of cell damage due to overheating. It is advised that most battery management systems incorporate temperature sensors within the monitoring modules themselves. However, for the purpose of this project a separate safety system with analog safety sensors (temperature/moisture) has been installed in series with latching master module.

With the above safety considerations, front end loading phase 1 proposed the use of the Zeva 8 cell monitor module version 1.3. As per specification sheet on Appendix D, each individual module is able to monitor 2-8 cells per module. This is ideal since circuit design of the power source has meant the construction of 8 cells per module in parallel with 30 of these individual modules in series connection.

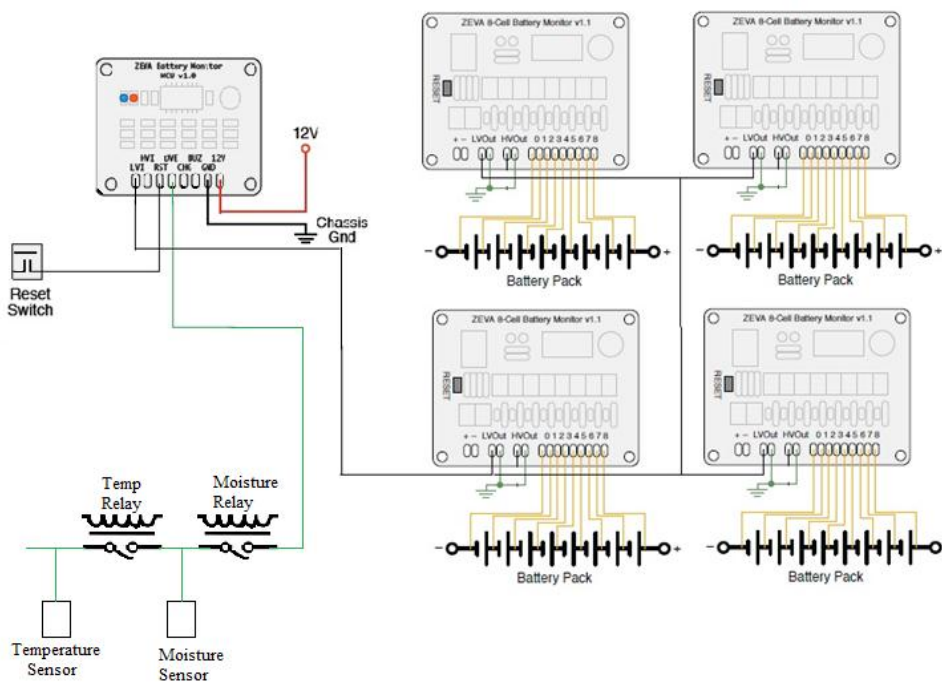
Furthermore, as per table 2, over voltage threshold for these cells is rated at $3.65 \pm 0.05V$ which allows the use of the Zeva modules due to its overvoltage cut off at 3.70V. Another important aspect is prolonging the cycle life of the battery cells to an estimated 2000 cycles. Care should be taken to avoid deep discharging whereby the cells are discharged beyond its 90% DOD. The Zeva monitoring modules have an embedded under voltage threshold cut-off at 2.0V which is ideal as this represents 80% DOD. The modules are designed to display certain error and run conditions through LED status lights. The single LED light has three different status modes as indicated by the specification sheet on Appendix E. A solid green on light represents normal safe operation of cells, and flashing status (2 flashes per second)

indicates cells are above 3.7 (over voltage warning). In the case that the LED status light blinks intermittently (every second) this indicated under voltage warning (i.e. cells are below 2.0V). An off status for the LED will indicate a wiring/short circuit error. A total of four non-latching monitoring modules are used in the following power circuit.

14. MODULE CIRCUIT DESIGN

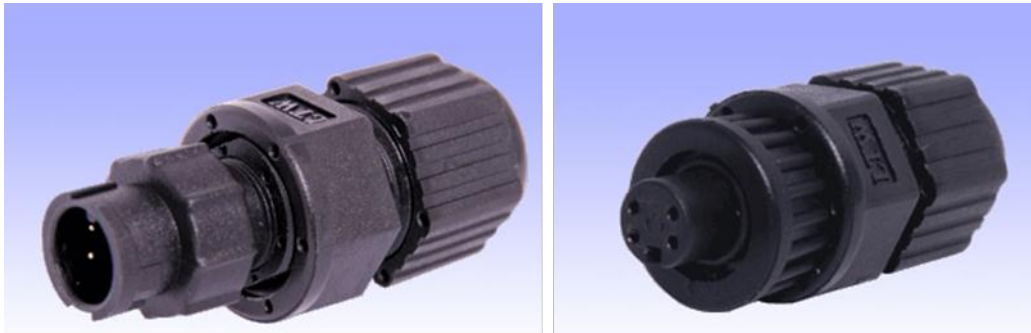
Each of the four BMS modules are non-latching since these modules are to be connected as a daisy chain (series connections) to the master module. The master module is to be latching which allows the circuit to be energised through a primary safety relay only when the master module detects both a healthy loop and optimal cell conditions. In the instance an error is detected, either in the circuit loop or battery cell conditions, then a red led status light will be displayed. The monitor module must be then placed in “reset” mode through the “RST” pushbutton to re-energize the circuit provided the error conditions has been resolved. Whilst provisions have been made on the monitoring module for a warning buzzer, this feature will not be used for the following project. Both the monitoring modules and master module are designed to take a power input of 12V through the use of an auxiliary battery. A low voltage signal will be used as for interconnections between the modules to provide extra accuracy in monitoring capabilities. Inter module connection is shown below:

Figure 41: INTER MODULE WIRING DIAGRAM



Each of the modules at every node shall be connected to a single battery module input numbered 0 through to 8. As per the module wiring diagram figures 25 to 27, low current wires shall be used in order to make these connections to each of the monitor module. To maintain a minimum ingress protection rating of IP65 as stipulated in the design scope section 3.8, waterproof connectors will be used to minimise the risk of moisture exposure. These waterproof connectors can be seen below:

Figure 42: 4 INPUT WATERPROOF CONNECTORS (ALTRONICS 2013)

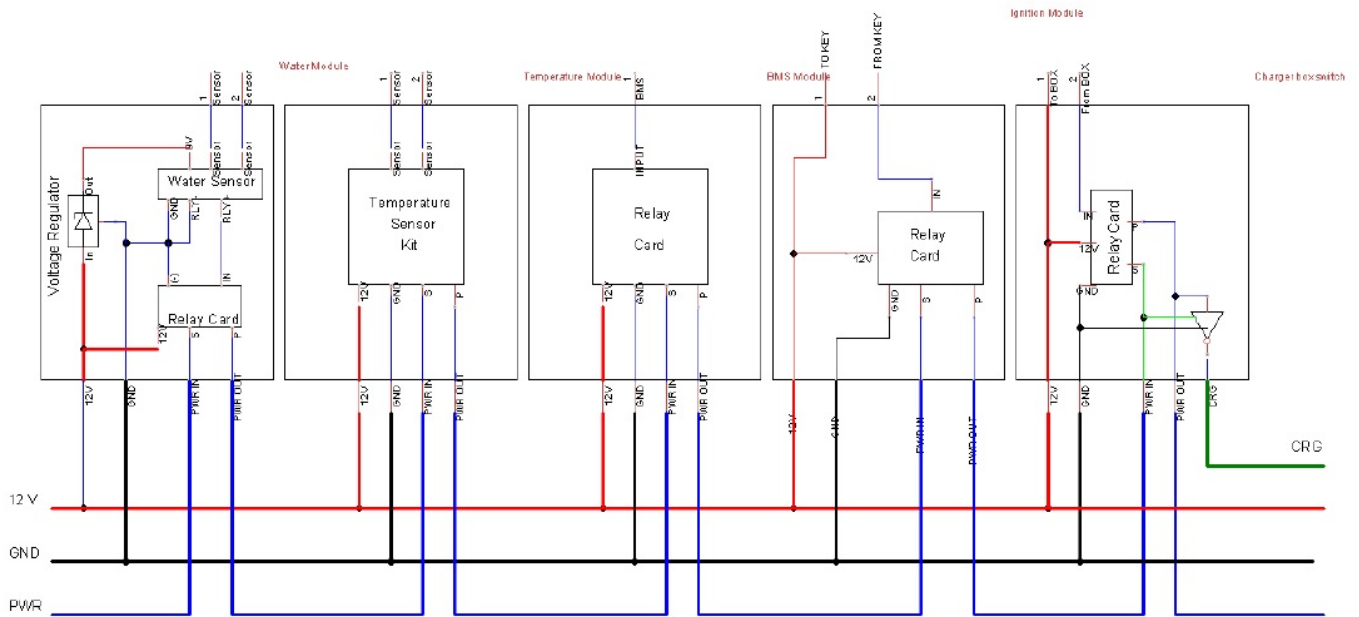


Male and female interlocking connectors will allow each of the BMS wires numbered 1 to 4 (figures 25 to 27) to be connected into these glands. The outputs will then be soldered onto the respective inputs of the monitoring modules. Altogether there will be 30 BMS wires (30 series connected modules) that will be attached to the respective monitoring modules. As can be seen from the inter module wiring, a low voltage output signal shall be carried through to the neighbouring modules and also to the master module.

Power to each module is read through input 8 and therefore, in the production phase, careful attention will be focused on attaching a single BMW wire to input 8 for every module. The 12V signal for the master module will be provided by means of an auxiliary 7.2Ah 12V sealed lead-acid battery. Placement of the reset switch shall be within the enclosure so that, in an event of a condition error, the reset pushbutton cannot accidentally be pushed when in close proximity to the user.

Primary safety within the following BMS system is from the charge enabled relays which form a part of the safety system on the watercraft. Currently, a design proposal for a temperature sensor and moisture sensor have been confirmed. These will form a part of the safety system in which the power source circuit can only be energised once safety relays read a healthy loop. Safety system design has been allocated to another colleague within the REV Jet Ski project. All interconnections between safety sensors are shown in the figure below:

Figure 43: SAFETY SYSTEM WIRING DIAGRAM (RILEY WHITE 2013)



Each individual relay for temperature, moisture and ignition will be powered through a 12V DC signal. When power and a high signal ‘1’ is sent to each module, this will allow the individual relays to be energised and thus close the loop. If a healthy loop is detected through all such safety modules, then 12V power shall be sent to the monitor module to allow for the power source circuit to be also energised.

14.1 BMS HOUSING

The Zeva monitoring modules including th

e master, are to be housed within a flange mountable box that will maintain an ingress protection rating of IP68. Gland penetrations will be made on the sides of the box so that BMS wiring can be passed through waterproof glands to minimise exposure to moisture. Furthermore the box is to be mounted on top of the battery enclosure as this will provide easy access for both monitoring and maintenance purposes.

15. CONCLUSION

Conducted thermal and charge concentration simulations indicate that optimal thermal conditions for the lithium iron phosphate cells will be 50°C. However results obtained indicate that electrochemical phenomena such as thermal runaway and internal impedance causes the total exothermic heat released to reach in excess of safe operating temperatures. Currently no provisions have been made for the inclusion of a cooling system for the battery enclosure which may come at the detriment of performance. One of the primary objectives in the project is to be able to market the electric watercraft on a commercial basis. However the success of such a goal can only be possible if performance figures are somewhat comparable to the Jet ski ICE counterpart. Numerous delays in workshop fabrication and part lead time has meant that progress on the project is extremely slow and hence why performance evaluation will not be completed in the following year.

15.1 LIMITATIONS

Another important consideration is that while simulated data may indicate such inherent problems its validity can only be found once performance evaluation begins. Both the mathematical and simulation models derived will always have some degree of inaccuracy due to the unavailability of specific data pertaining to the cells. However the software used gives great insight into how one may expect the lithium ion batteries to operate with the given voltage and current loads. As per the discussions made within the study, every attempt has been made to relate the mathematical models with true acquired data from previous experiments. It was found that concepts like Peukerts law holds quite accurately to real data acquired with an error margin of 4%.

15.2 FUTURE WORK

In the short term project timeline a solution to cooling the battery modules will need to be found. Another important aspect is obtaining adequate sponsorship for this project as monetary limitations has placed a lot of inflexibility in the parts that the team can purchase. Lithium ion batteries are still a relatively new technology and therefore in the coming years the project may look into improving the run time of the watercraft by investing in newer technologies such as porous three dimensional lithium salt batteries. These are expected to provide 1000 times the standard energy density of current lithium cells whilst being

extremely compact and lightweight. The only drawback is the high manufacturing price involved.

16. REFERENCES

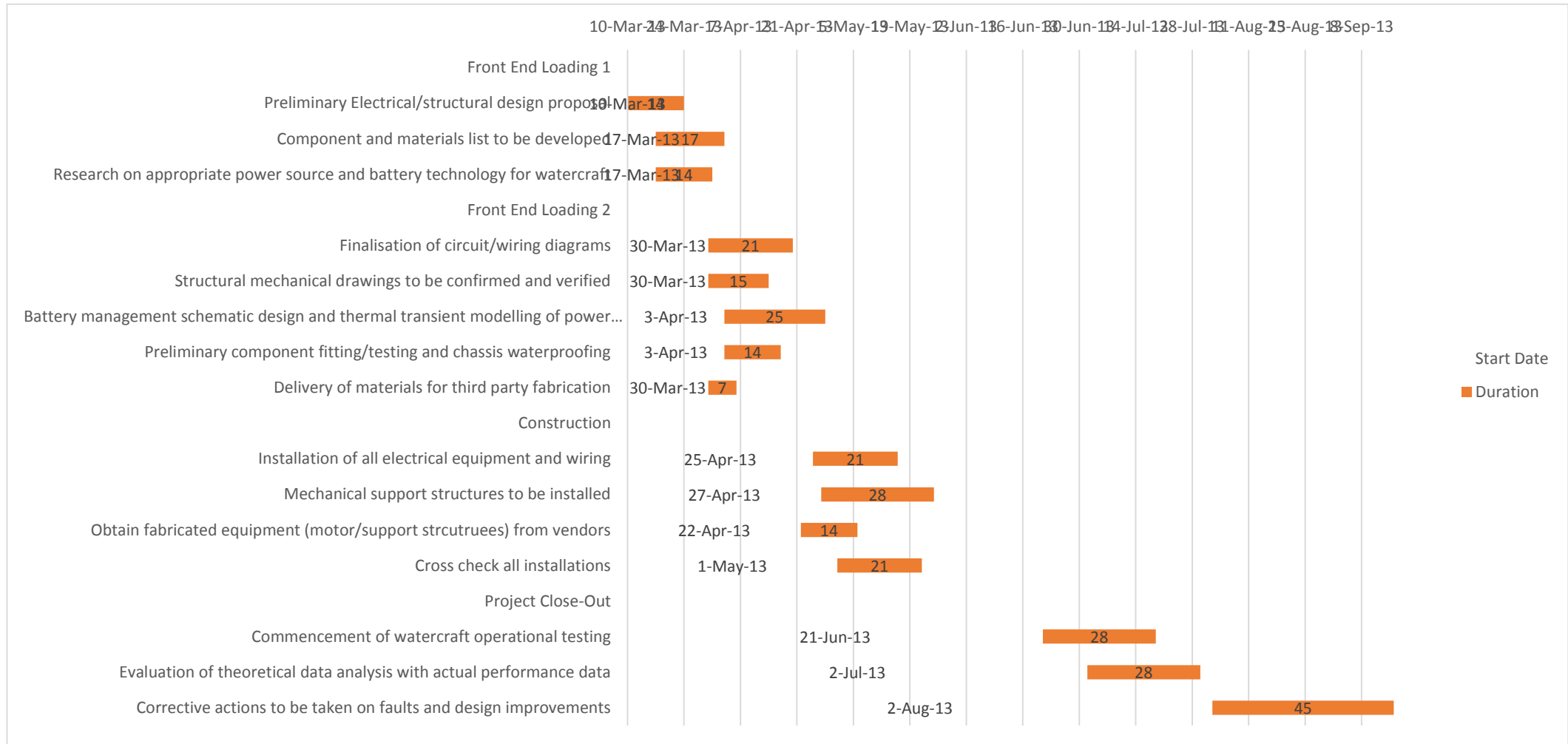
- [1] S. Mcluer, "Battery Technology for Data Centers and Network Rooms: Lead-Acid Battery Options," *Data Center Science Center*, vol. 12, pp. 1-9, 2009.
- [2] J. Urban, "Voltage Testing of Lead Acid Batteries," Urban Power, LLC, New York, 2002.
- [3] C. W. L. Y. W. a. K. S. Kwo Young, "Electric Vehicle Battery Technologies," in *Power Electronics and Power Systems*, New York, Springer Science, 2013, pp. 5-15.
- [4] SAE INTERNATIONAL, "VEHICLE ELCTRIFICATION STANDARDS," SAE INTERNATIONAL, 1 February 2013. [Online]. Available: <http://www.sae.org/standardsdev/vehiclelectrification.htm>. [Accessed 19 October 2013].
- [5] IEC, "Norme Internationale," The International Electrotechnical Commision, 19 November 2004. [Online]. Available: <http://www.scribd.com/doc/123279841/IEC-228-Conductors-of-Insulated-Cabes>. [Accessed 14 April 2013].
- [6] T. F. a. J. N. M. Doyle, "Modeling of galvanostatic charge and discharge of the lithium/polymer/insertion cell," *Electrochemical Society*, vol. 140, no. 75, p. 144, 1993.
- [7] IEEE-PSES , "Ingress Protection Testing and IP Codes," in *IEC60529*, 2009.
- [8] E. M. J. W. P. K. J. Li, "Studies on the cycle life of commercial lithium ion batteries during rapid charge–discharge cycling," *Journal of Power Sources*, vol. 294, no. 301, pp. 5-8, 2001.
- [9] Power Management, "Battery Powered Linux Mini-HOWTO," 18 August 2008. [Online]. Available: <http://www.tldp.org/HOWTO/Battery-Powered/battery.html>. [Accessed 1 October 2013].
- [10] H. A. Catherino, "Physical Chemistry," in *Secondary Batteries: Lead Acid Battery Thermal Runaway*, California, DTIC ONLINE, 2007, pp. 21-24.
- [11] DIFF-EN, "Difflen," 5 January 2013. [Online]. Available: http://www.difflen.com/difference/Li-ion_vs_NiCad. [Accessed 17 June 2013].
- [12] SAE, "Electric and Hybrid Vehicle Propulsion Battery System Safety Standard - Lithium-based Rechargeable Cells.," SAE International, 1 February 2013. [Online]. Available: http://standards.sae.org/j2929_201102/. [Accessed 19 October 2013].
- [13] C. R. Wylie, *Advanced Engineering Mathematics*, New York - London: McGraw-Hill, 1999.
- [14] I. Buchmann, "Battery University," Cadex, 12 March 2013. [Online]. Available:

http://batteryuniversity.com/learn/article/water_loss_acid_stratification_and_surface_charge.
[Accessed 7 July 2013].

- [15] W. T Doyle. John Newman, "Porous-electrode theory with battery applications," *AICHE Journal*, vol. 21, no. 1, pp. 25-41, 2004.
- [16] B. S. a. K. Goebel, " Modeling Li-ion Battery Capacity Depletion in a Particle Filtering Framework," *NASA Ames Research Center*, vol. 1, no. 1, pp. 1-8, 2009.
- [17] D. S. T. a. D. P. F. Dr Michael Raupach, "CSIRO," Marine and Atmospheric Research, 27 November 2006. [Online]. Available: <http://www.csiro.au/Organisation-Structure/Divisions/Marine--Atmospheric-Research/Increase-in-carbon-dioxide-emissions-accelerating.aspx>. [Accessed 23 March 2013].
- [18] The University Of Vermont, "Personal Watercraft: Safety and Environmental Impact," Vermont Legislative Research , Vermont, 2001.
- [19] T. Stienstra, "Park Service to Ban Personal Watercraft," *Examiner Outdoors*, pp. 1-4, 8 July 1998.
- [20] The University Of Western Australia, "UWA Health and Safety," UWA, 1 January 2013. [Online]. Available: <http://www.safety.uwa.edu.au/topics/electrical-safety/appliance-guidelines>. [Accessed 7 September 2013].
- [21] MIT, "MIT Electric Vehicle Team," Massachusetts Institute of Technology, Massachusetts, 2008.
- [22] C. M. Laurence Croguennec, "Towards high energy density sodium ion batteries through electrolyte optimization," *Energy & Environmental Science*, vol. 10, no. 8, pp. 14-17, 2013.
- [23] M. J. a. B. Haverkort, "Battery Modeling," *UTWENTE*, vol. 1, no. 1, pp. 17-23, 2007.
- [24] IEEE, "Energy efficient battery management," *IEEE Journal on Selected Areas in*, vol. 19, no. 7, p. 177, 2001.

17. APPENDICES

APPENDIX A



Appendix B

JS102-50kW 96V 135Hz 200mm

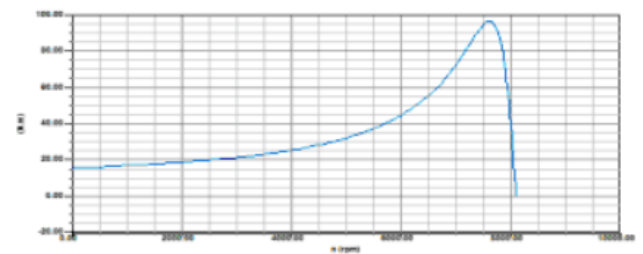
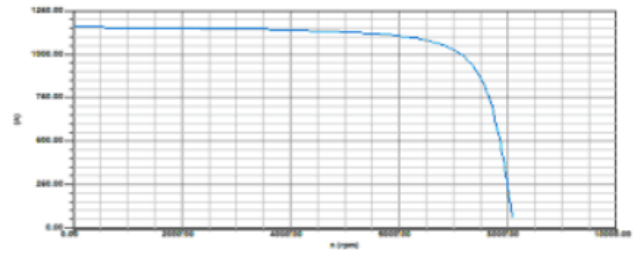
16/09/2012

BEST

Given Output Power (kW):	50	50	50	50
Rated Voltage (V):	96	96	96	96
Winding Connection:	Delta	Wye	Wye	Wye
Number of Poles:	2	2	2	2
Given Speed (rpm):	8000	8000	8000	8000
Frequency (Hz):	135	135	135	135
Stray Loss (W):	250	250	250	250
Frictional Loss (W):	150	150	150	150
Windage Loss (W):	150	150	150	150
Type of Load:	Constant Power	int Power	int Power	int Power
Operating Temperature (C):	75	75	75	75

STATOR DATA

Number of Stator Slots:	24	24	24	24
Outer Diameter of Stator (mm):	224	224	224	224
Inner Diameter of Stator (mm):	110	110	110	110
Type of Stator Slot:	3	3	3	3
Dimension of Stator Slot				
hs0_stator (mm):	1	1	1	1
hs1_stator (mm):	1.12	1.12	1.12	1.12
hs2_stator (mm):	25.98	25.98	25.98	25.98
bs0_stator (mm):	4.5	4.5	4.5	4.5
bs1_stator (mm):	8.37091	8.37091	8.37091	8.37091
bs2_stator (mm):	15.2116	15.2116	15.2116	15.2116
rs_stator (mm):	2	2	2	2
Top Tooth Width (mm):	6.6	6.6	6.6	6.6
Bottom Tooth Width (mm):	6.6	6.6	6.6	6.6
Length of Stator Core (mm):	200	180	170	165
Stacking Factor of Stator Core:	0.95	0.95	0.95	0.95
Type of Steel:	DW315_50	W315_50	W315_50	W315_50
Number of lamination sectors	1	1	1	1
Press board thickness (mm):	0	0	0	0
Magnetic press board	No	No	No	No
Number of Conductors per Slot:	7	4	4	4
Number of Parallel Branches:	2	2	2	2
Number of Wires per Conductor:	5	9	9	9
Type of Coils:	11	10	10	10
Coil Pitch:	11	11	11	11



Appendix B

Armature Copper Density (kg/m ³):	8900	8900	8900	8900
Rotor Bar Material Density (kg/m ³):	8900	8900	8900	8900
Rotor Ring Material Density (kg/m ³):	8900	8900	8900	8900
Armature Core Steel Density (kg/m ³):	7600	7600	7600	7600
Rotor Core Steel Density (kg/m ³):	7600	7600	7600	7600
Armature Copper Weight (kg):	13.6946	13.4328	13.085	12.911
Rotor Bar Material Weight (kg):	2.56644	2.30979	2.18147	2.11731
Rotor Ring Material Weight (kg):	1.4508	1.4508	1.4508	1.4508
Armature Core Steel Weight (kg):	31.1656	28.049	26.4907	25.7116
Rotor Core Steel Weight (kg):	5.58917	5.03025	4.75079	4.61106
Total Net Weight (kg):	54.4666	50.2727	47.9588	46.8018
Armature Core Steel Consumption (kg):	60.6851	54.6166	51.5823	50.0652
Rotor Core Steel Consumption (kg):	13.7228	12.3505	11.6644	11.3213
RATED-LOAD OPERATION				
Stator Resistance (ohm):	0.00543842	0.001646	0.001604	0.001582
Stator Leakage Reactance (ohm):	0.0697862	0.030588	0.029314	0.028663
Rotor Resistance (ohm):	0.00973848	0.002945	0.002828	0.002769
Rotor Leakage Reactance (ohm):	0.114821	0.03361	0.03196	0.031095
Resistance Corresponding to Iron-Core Loss (ohm):	66.605	19.5658	18.472	17.9222
Magnetizing Reactance (ohm):	3.20249	0.933966	0.874659	0.841934
Stator Phase Current (A):	211.085	374.624	370.868	369.366
Current Corresponding to Iron-Core Loss (A):	1.32784	2.53589	2.70646	2.79891
Magnetizing Current (A):	27.6162	53.1247	57.1579	59.5801
Rotor Phase Current (A):	200.952	355.876	351.28	349.223
Copper Loss of Stator Winding (W):	726.957	693.201	661.777	647.703
Copper Loss of Rotor Winding (W):	1179.77	1119.02	1046.85	1013.15
Iron-Core Loss (W):	352.305	377.467	405.919	421.202
Frictional and Windage Loss (W):	293.627	294.318	295.142	295.529
Stray Loss (W):	250	250	250	250
Total Loss (W):	2802.66	2734	2659.69	2627.59
Input Power (kW):	52.7998	52.7307	52.6574	52.6265
Output Power (kW):	49.9971	49.9967	49.9977	49.9989
Mechanical Shaft Torque (N.m):	60.3256	60.2539	60.1705	60.1324

Appendix B

Efficiency (%):	94.6919	94.8152	94.9491	95.0071
Power Factor:	0.864412	0.842504	0.849849	0.8528
Rated Slip:	0.0229212	0.021767	0.020391	0.019747
Rated Shaft Speed (rpm):	7914.34	7923.69	7934.84	7940.05
NO-LOAD OPERATION				
No-Load Stator Resistance (ohm):	0.00543842	0.001646	0.001604	0.001582
No-Load Stator Leakage Reactance (ohm):	0.0699069	0.030638	0.02936	0.028706
No-Load Rotor Resistance (ohm):	0.00973671	0.002945	0.002827	0.002769
No-Load Rotor Leakage Reactance (ohm):	1.54912	0.422163	0.371975	0.351156
No-Load Stator Phase Current (A):	29.4628	57.6597	61.5321	63.8776
No-Load Iron-Core Loss (W):	397.431	441.446	466.888	480.721
No-Load Input Power (W):	980.969	1003.95	1069.09	1080.06
No-Load Power Factor:	0.0861456	0.078639	0.080057	0.07815
No-Load Slip:	0.000117516	0.000101	0.00011	0.000106
No-Load Shaft Speed (rpm):	8099.05	8099.18	8099.11	8099.14
BREAK-DOWN OPERATION				
Break-Down Slip:	0.07	0.06	0.06	0.06
Break-Down Torque (N.m):	97.6001	88.0791	93.3874	96.258
Break-Down Torque Ratio:	1.61789	1.4618	1.55205	1.60077
Break-Down Phase Current (A):	459.015	735.892	773.1	793.152
LOCKED-ROTOR OPERATION				
Locked-Rotor Torque (N.m):	20.1279	13.9218	15.0851	15.887
Locked-Rotor Phase Current (A):	688.392	1048.63	1115.01	1156.73
Locked-Rotor Torque Ratio:	0.333655	0.231053	0.250706	0.264201
Locked-Rotor Current Ratio:	3.26121	2.79915	3.00649	3.13165
Locked-Rotor Stator Resistance (ohm):	0.00543842	0.001646	0.001604	0.001582
Locked-Rotor Stator Leakage Reactance (ohm):	0.0681067	0.030271	0.028918	0.028178
Locked-Rotor Rotor Resistance (ohm):	0.0126702	0.003807	0.003642	0.003559
Locked-Rotor Rotor Leakage Reactance (ohm):	0.0717822	0.022858	0.021015	0.019931
DETAILED DATA AT RATED OPERATION				
Stator Slot Leakage Reactance (ohm):	0.0304867	0.017918	0.016923	0.016426

Appendix C

MODEL 1236/1238

CURTIS



DESCRIPTION

Curtis Models 1236 and 1238 provide advanced control of AC induction motors performing on-vehicle traction drive or hydraulic pump duties. They offer vehicle developers a highly cost-effective combination of power, performance and functionality.

APPLICATION

Designed primarily for use on medium to large material handling vehicles such as counterbalance or warehouse trucks. The Model 1236 is equally suitable for Light-On-Road passenger vehicles and utility vehicles. The larger Model 1238 is also intended for use on all heavy-duty applications such as Tow Tractors and Airport Ground Support Equipment (GSE).

Patents Pending

www.curtisinstruments.com

Only Curtis AC can offer:

- **Curtis VCL -Vehicle Control Language** is an easy to use programming language that allows vehicle developers to write powerful logic functions and create a 'virtual system controller'. Curtis offers customers VCL development tools and training. Curtis also provides a VCL service where Curtis engineers will work with the OEM to create any custom VCL code required.
- **Indirect Field Orientation (IFO) vector control** algorithm generates the maximum possible torque and efficiency across the entire speed range. Advanced Curtis IFO vector control provides superb drive 'feel', improved speed regulation and increased gradeability.
- **Curtis Auto-Tune** function enables quick and easy characterization of the AC motor without having to remove it from the vehicle. Curtis AC controllers are fully compatible with any brand of AC motor.
- **Dual-Drive functionality** is standard, allowing correct control of vehicles such as 3-wheel counterbalance trucks or other applications featuring twin traction motors. This function ensures smooth and safe operation, minimal tire wear and correct load sharing between the traction motors at all times.
- **Configurable CANbus** connection allows communication with other CANbus enabled devices. These models are CANopen compatible and can be further customized and configured using VCL.
- **Integrated System Controller** - More than just motor controllers, they are also powerful system controllers. They feature a comprehensive allocation of multi-function I/O pins for use as analog inputs, digital inputs, contactor coil drivers and proportional valve drivers. In addition to this local I/O, these controllers can use VCL to map and configure the remote I/O available on other CANbus devices, send messages to CAN displays and thus control and monitor the entire system.

FEATURES

Advanced functionality, compact power

- High frequency, silent operation across the 0–300Hz stator frequency range.
- Models available for 350–800A output at 24–96V system voltages. These are true 2 minute RMS ratings, not short duration 'boost' ratings.
- Powerful operating system allows parallel processing of vehicle control tasks, motor control tasks and user configurable programmable logic.
- Advanced Pulse Width Modulation techniques produce low motor harmonics, low torque ripple and minimized heating losses, resulting in high efficiency.

Appendix C

MODEL 1236/1238

FEATURES *continued*

Unmatched Flexibility

- Programmable for either traction or pump applications.
- Field upgradeable software.
- Integrated Battery state-of-charge algorithm and hour meter.
- Multi-Mode™ provides user-selectable vehicle operating profiles.
- Fully-featured generic software and VCL for typical Warehouse Truck applications is included.
- Comprehensive programming options and VCL allow other applications to be easily supported.
- Curtis handheld or PC Windows programming tools provide easy programming and powerful system diagnostic tools.
- Integrated status LED provides instant diagnostic indication.

Robust Safety and Reliability

- Insulated Metal Substrate power base provides superior heat transfer for increased reliability.

- Fail-Safe power component design.
- Redundant hardware watchdog timers.
- Reverse polarity protection on battery connections.
- Short circuit protection on all output drivers.
- Thermal cutback, warning, and automatic shutdown provide protection to motor and controller.
- Rugged sealed housing and connectors meet IP65 environmental sealing standards for use in harsh environments.

Meets or complies with relevant US and International Regulations

EMC: Designed to the requirements of EN12895

Safety: Designed to the requirements of EN1175

IP65 Rated per IEC 529

UL recognized

Regulatory compliance of the complete vehicle system with the controller installed is the responsibility of the vehicle OEM.

MODEL CHART

Model	Battery Voltage V	2 Min RMS Current Rating (A)	2 Min RMS Power Rating (kVA)
1236-44XX	24-36	400	16.6
1236-45XX	24-36	500	20.9
1238-46XX	24-36	650	25.4
1238-48XX	24-36	800	31.2
1236-53XX	36-48	350	19.7
1236-54XX	36-48	450	24.8
1238-54XX	36-48	450	25.5
1238-56XX	36-48	650	36.3
1236-63XX	48-80	300	28.1
1236-64XX	48-80	350	32.4
1238-65XX	48-80	550	51.3
1238-66XX	48-80	650	60.6
1238-75XX	72-96	550	62.3
1238-76XX	72-96	650	73.6

SYSTEM ACCESSORIES



The Curtis Model 840 LCD Multifunction display contains 8 large, easy to read characters to provide display of battery discharge (BDI), hour meter and error messages. Built-in backlight is also available.



The Curtis model 1352 CANbus I/O expansion module features 9 I/O pins, including 6 proportional valve drivers. This module can be used to further expand the I/O capability of Curtis AC motor controllers using VCL.



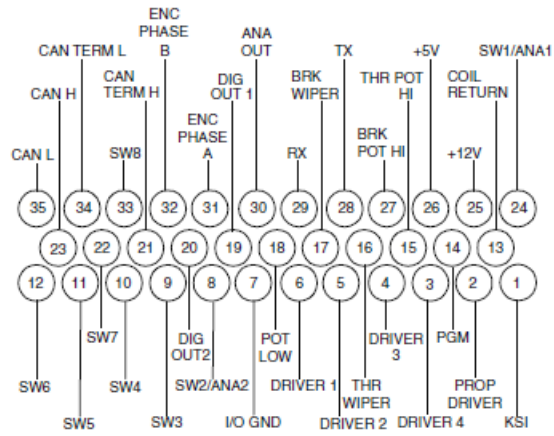
The Curtis Model 1313 Handheld Programmer is ideal for setting parameters and performing diagnostic functions.

Contact Curtis to obtain the VCL Vehicle Control Language compiler and development tools.

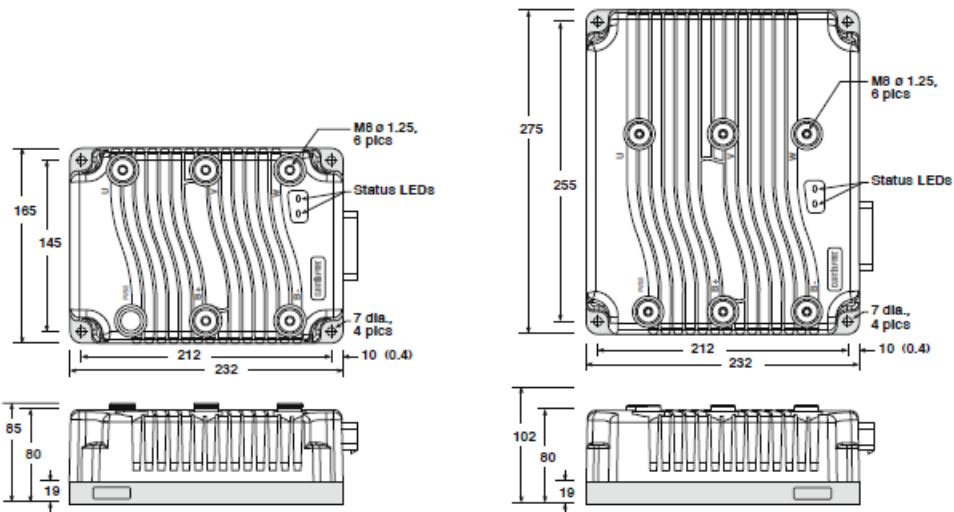
Appendix C

MODEL 1236/1238

CONNECTOR WIRING



DIMENSIONS mm



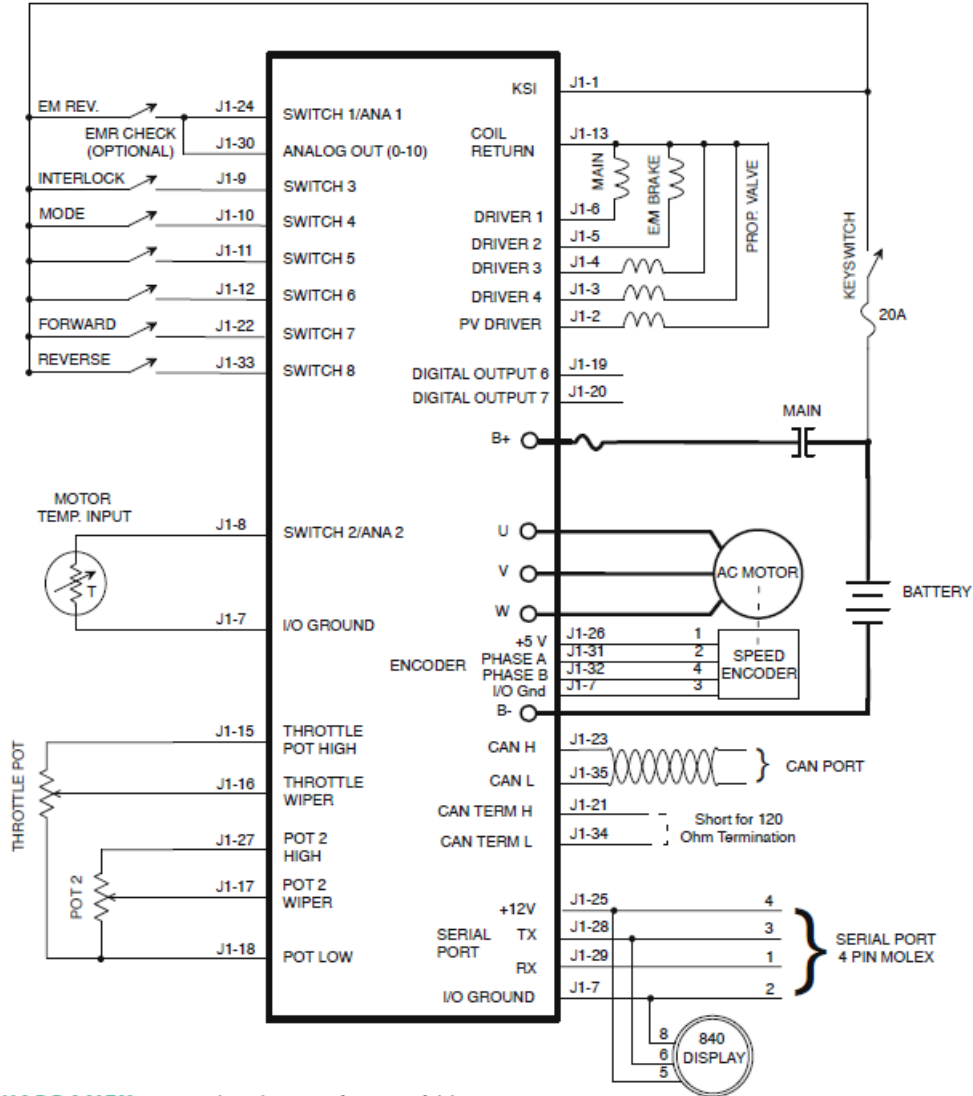
1236

1238

Appendix C

MODEL 1236/1238

TYPICAL WIRING



WARRANTY Two year limited warranty from time of delivery.

Appendix D

ZERO EMISSION
VEHICLES AUSTRALIA



<http://www.zeva.com.au>



8-cell Battery Monitor Module v1.3

*Simple, reliable and economical protection
for your LiFePO4 battery pack.*

Please read these instructions carefully for proper installation and use of this product.

SPECIFICATIONS

- Monitor 2–8 cells per module
- Automatic cell count detection
- Over-voltage threshold: 3.7V
- Under-voltage threshold: 2.0V
- Sampling rate: 10Hz
- Dimensions: 68x52x15mm
- Solid State Relay (SSR) output, 500mA max.
- Status LEDs for visual feedback
- Power consumption:
6.5mA when SSR on, 3.5mA when SSR off

PROTECTING YOUR LITHIUM BATTERIES

Lithium batteries have been a revolution in energy storage and a major enabling factor in the resurgence of electric vehicles. However lithium batteries can be damaged if their voltage goes out of safe operating range – either too high (overcharging) or too low (over-discharging).

Battery packs are commonly built from a large number of individual cells in series to achieve higher voltages. Due to manufacturing tolerances, cells always have some variation in capacity, so there will always be some cells in a pack which get full or go flat before others.

In battery packs made up of many cells in series, the overall voltage gives little indication of the voltage of individual cells in the chain. As such it is important to have a system which monitors the voltages of each cell and take action if any individual cell goes out of range.

ZEVA's 8-Cell Battery Monitoring Modules (BMMs) offer a simple and economical way to monitor the voltage of your Lithium Iron Phosphate (LiFePO4) cells, and signal external systems to protect the battery pack if a cell goes out of range. A single module can monitor 2–8 cells, or multiple modules can be cascaded for larger packs.

The BMM is microcontroller based and uses a Solid State Relay (SSR) output to signal over-voltage or under-voltage conditions. There is also a blue LED which provides visual feedback on module status.

Battery management or monitoring systems are the last line of defence for your battery pack. In normal circumstances it should not interfere with the vehicle operation, only intervening when something goes wrong and protection is required.

WHY NO BALANCING?

As well as cell voltage monitoring, most Battery Management Systems (BMS) include a mechanism for balancing cells, typically by shunting some power off high cells. Balanced cells are all at the same state of charge, which maximises the usable capacity of the pack.

Cells should be manually balanced when first installed by individually charging them to 3.65V (known as *top balancing*). Thereafter the only reason they get out of balance are variations in self-discharge, or variations in quiescent current draw by BMS modules themselves. Self-discharge in lithium cells is very low – typically around

1% per month. Variations in self discharge between cells due to manufacturing tolerances are typically an order of magnitude lower again. So if they start balanced, they may need no further balancing for the life of the pack. (But occasional "health checks" of your battery pack are still a good idea.)

Over the years we have seen dozens of instances where shunt balancing caused more trouble than its worth. Shunt systems may fail from manufacturing faults, damage during installation or component ageing. If they fail to come on, the cell ends up higher than the others. If they get stuck on (a common failure mode in transistors), the cell will be continually discharged.

For these reasons, we decided to develop a battery protection system without active balancing.

MODULE VARIANTS

Modules are available either with momentary outputs or latching outputs:

- **Momentary outputs:** In packs with more than 8 cells, multiple BMMs will be needed to monitor all the cells, and a supervisor module is used to monitor outputs from BMMs and take actions. Output relays are closed only while all cells monitored by the BMM are in range.
- **Latching outputs:** For packs with 4-8 cells, one BMM can monitor the whole pack. Output relays are closed when all cells are within range, but will open and remain open if a cell goes out of range. This can be used to shut down your charger (using the overvoltage output) or drive system (using the undervoltage output) to protect the cells. Resetting the module is achieved by momentary power cycling (via onboard pin jumper, or added remote switch). Latching modules are indicated by a **green sticker on the microcontroller**.

Modules may also be ordered with or without **sockets and locking plugs**. Without plugs/sockets, wires are soldered directly to the PCB. This is suitable for installations when the BMM will never be disconnected from the battery. Plugs & sockets are recommended in installations where boards may periodically be disconnected from batteries. It can also make installation safer as wiring can be completed before the BMM is plugged in.

18. CD CONTENT

This provides a brief outline of all files within the CD:

1. Don_Madappuli_Dissertation_REV5.pdf
2. Batterytemp.m (bus bar thermal simulation script)
3. Hotwire WorkBench files – Ansys simulation profiles/Geometries